Advances towards the development of compact relativistic electron and bright x-ray sources

Key scientific and technological demonstrations

Sergio Carbajo

Fachbereich Physik

Universität Hamburg

This dissertation is submitted to the University of Hamburg for the degree of

Doctor rerum naturalium

Fakultät für Mathematik,
Informatik und
Naturwissenschaften

March 2015

Date of oral defense: 13 March, 2015

The following evaluators recommend the admission of the dissertation:
Prof. Dr. Daniela Pfannkuche

Prof. Dr. Franz X. Kärtner

Prof. Dr. Henry N. Chapman

Prof. Dr. Wilfried Wurth

Prof. Dr. Peter Schmelcher

Maite ditut
maite
geure bazterrak
lanbroak
izkutatzen dizkidanean
zer izkutatzen duen
ez didanean ikusten uzten
orduan hasten bainaiz
izkutukoa
nere barruan bizten diren
bazter miresgarriak
ikusten.

- Mikel Laboa

Declaration

I hereby declare that except where specific reference is made to the work of others, the contents of this dissertation are original and have not been submitted in whole or in part for consideration for any other degree or qualification in this, or any other university. This dissertation is my own work and contains nothing which is the outcome of work done in collaboration with others, except as specified in the text and acknowledgements.

Sergio Carbajo
March 2015

Acknowledgements

First and foremost, I want to express my deepest gratitude to my doctoral advisor, Prof. Franz X. Kärtner. His evergrowing enthusiasm has the unique engaging ability to break through boundaries contrived from skepticism and wear, and his imaginative mind is an inexhaustible driving force for that which does not violate any fundamental physical principle to happen. Through his support, I have been given the opportunity to explore and feed my intellectual curiosity with a great deal of autonomy, and to consolidate my scientific career in completely unanticipated pathways. For that, I am honored and grateful.

I would like to extend my gratitude to all my colleagues both a MIT and CFEL. I have had the pleasure to work closely with a large and diverse group of people, mastered their skills and digested their knowledge as my own. It is only in such distinct environment that I have put my mind and hands in work that reaches well beyond the one presented in this thesis. I would also like to thank my doctoral committee members for their helpful feedback.

In particular, I am happy to make mention of direct contributors to the work presented here. In terms of high-power laser sources, Luis Zapata has made major conceptual contributions to the design of the cryogenic Yb:YLF amplifier system. Hongyu Yan developed entirely the fiber oscillator for the Yb:YLF laser. Yue Zhou worked for many hours hand in hand together with me in its initial experimental implementation stages. Hua Lin finished up some of the latter work before the system was shipped from MIT to CFEL. As for terahertz source development, I would like to acknowledge experimental contributions from Xiaojun Wu and Frederike Ahr in optical rectification systems developed together at CFEL; theoretical support from Koustuban Ravi, which guided us through optimization processes to push the limits; and pump-source development by Anne-Laure Calendron and Huseyin Cankaya. Finally, in enabling the first demonstration of direct laser acceleration of electrons in vacuum, I would like to give credit to the contributions made by Eduardo Granados, Kyung-Han Hong, and Jeffrey Moses in few-cycle source development; the very essential theoretical and modeling efforts of Liang Jie Wong; and Emilio Nanni's dedication to two intense but productive weeks of unstoppable search for accelerated electrons.

As in any progress in life worth pursuing, my family, friends, and Avana deserve my most evermore increasing appreciation. This recognition holds special meaning in that during this period of time they bore the entire load of the unannounced, the anguish, for me. I am proud to culminate this work with a full dedication to my most beloved ones.

Abstract

Compact brilliant attosecond electron and x-ray sources promise to bring wide-spread access to groundbreaking scientific, technological, and medical tools. In the pursuit of such visionary technology, this thesis describes in detail three key scientific and technological feasibility advances towards the development of novel electron and x-ray sources based entirely on optical lasers. The main areas covered are (i) high average- and peak-power optical laser development, (ii) efficiency scaling and limitations of terahertz radiation generation, and (iii) direct longitudinal laser acceleration of electrons in vacuum. In (i) we will point at Yb:YLF technology as a candidate for optical energy scaling at high repetition rates and sub-ps pulse durations, and will present a thorough front-end design and preliminary experimental results. In (ii) we will describe in detail theoretical and experimental aspects of the primary mechanisms that contribute to increasing and ultimately saturating the optical-to-terahertz energy conversion efficiency in lithium niobate through optical rectification, and show the highest efficiency demonstrated to date. In (iii) we will expound on the first-time demonstration of longitudinal acceleration of electrons using relativistic radially-polarized few-cycle pulses in an entirely free-space environment. Throughout the thesis and specially in the introduction, we will discuss how each independent topic relates to one another and ultimately integrates into the concept of compact relativistic electron and bright x-ray sources.

Kompakte, brillante Attosekunden-Elektronen- und Röntgenquellen treten mit dem Versprechen an, einen weitverbreiteten Zugang zu neuen bahnbrechenden wissenschaftlichen, technologischen und medizinischen Werkzeugen zu ermöglichen. In Verfolgung dieser visionären Technologie beschreibt diese Arbeit detailliert drei wesentliche Fortschritte bezüglich der wissenschaftlichen und technologischen Machbarkeit auf dem Weg zur Entwicklung neuartiger Elektronen- und Röntgenquellen, die ganz auf optischen Lasern basieren. Die wichtigsten in dieser Arbeit behandelten Themen sind (i) die Entwicklung optischer Lasersysteme mit hoher mittlerer und Spitzenleistung, (ii) Skalierung des Wirkungsgrades und die Grenzen bei der Erzeugung von Terahertz-Strahlung, und (iii) direkte Laser-Vorwärtsbeschleunigung von Elektronen im Vakuum. Im ersten Teil wird zunächst die Yb:YLF Technologie als Kandidat vorgestellt, um die optische Energie bei hohen Repetitionsraten und Impulsdauern unter einer Pikosekunden zu erhöhen. Wir präsentieren das ausgearbeitete Frontend-Design und erste experimentelle Ergebnisse. Der zweite Teil der Arbeit (ii) beschreibt genau die theoretischen und experimentellen Details der wichtigsten Mechanismen, die zur Steigerung und letztendlich Sättigung der Energiekonversionseffizienz vom optischen zum Terahertz-Bereich im nichtlinearen Medium Lithiumniobat durch optische Gleichrichtung beitragen. Hierbei wird die bisher höchste Konversionseffizienz gezeigt. In (iii) wird die erstmalige Demonstration der Vorwärtsbeschleunigung von Elektronen mit relativistischen, wenige Lichtzyklen langen, radial polarisierten Laserimpulsen im Vakuum diskutiert. Überall in der Doktorarbeit, und insbesondere in der Einleitung, wird aufgezeigt, wie jedes dieser unabhängigen Themen mit den anderen in Beziehung steht, und wie sich schließlich alles in das Konzept der kompakten relativistischen Elektronen- und brillanten Röntgenquellen integriert.

List of refereed journal publications derived from this thesis

1. **S Carbajo** et al., *Laser-induced Damage Threshold in Lithium Niobate*, *in preparation for* Opt. Mat. Exp.
2. **S Carbajo** et al., *Towards Relativistic Sub-Terahertz Transients*, *in preparation.*
3. **S Carbajo**, E Nanni, LJ Wong, RJD Miller, FX Kärtner, *On-axis laser acceleration of electrons in free-space*, submitted to Nature Photonics.
4. K Ravi, WR Huang, **S Carbajo**, E Nanni, D Schimpf, EP Ippen, FX Kärtner, *Theory of THz generation by Optical Rectification using Tilted-Pulse-Fronts*, arXiv preprint arXiv:1410.8120.
5. WS Graves, J Bessuille, P Brown, **S Carbajo**, V Dolgashev, K-H Hong, E Ihloff, B Khaykovich, H Lin, K Murari, EA Nanni, G Resta, S Tantawi, LE Zapata, FX Kärtner, DE Moncton, *Compact x-ray source based on burst-mode inverse Compton scattering at 100 kHz*, Phys. Rev. ST Accel. Beams 17, 120701 (2014).
6. K Ravi, WR Huang, **S Carbajo**, X Wu, F Kärtner, *Limitations to THz generation by optical rectification using tilted pulse fronts*, arXiv:1406.1439 (2014).
7. X Wu, **S Carbajo**, K Ravi, F Ahr, G Cirmi, Y Zhou, OD Mücke, FX Kärtner, *Terahertz generation in lithium niobate driven by Ti:Sapphire laser pulses and its limitations*, Optics Letters 39 (18), 5403-5406 (2014).
8. **S. Carbajo**, E Granados, D Schimpf, A Sell, KH Hong, J Moses, FX Kärtner, *Efficient generation of ultra-intense few-cycle radially polarized laser pulses*, Optics Letters 39 (8), 2487-2490 (2014).

List of conference proceedings derived from this thesis

1. **S Carbajo** et al., *Relativistic Few-cycle Cylindrical Vector Beams for Table-top Particle Accelerators*, CLEO 2015 (**invited**).
2. **S. Carbajo**, L.J. Wong, E. Nanni, R.J. Miller, F. X. Kärtner, *First Observation of Direct Laser On-axis Acceleration of Electrons in Vacuum*, OSA Proceedings Frontiers in Optics, FTh2A. 2 (2014) (*post-deadline*).
3. **S. Carbajo**, X. Wu, F. Ahr, F. X. Kärtner, *Terahertz Conversion Efficiency Scaling by Optical Rectification in the 800 nm Pump-Wavelength Range*, CLEO Proceedings Science and Innovations, SW1F. 6 (2014).

4. S. Fang, H. Ye, G. Cirmi, S.-H. Chia, **S. Carbajo**, O. D. Mücke, F. X. Kärtner, *High-Energy Carrier-Envelope Phase-Stable Optical Waveforms Compressible to 1 fs Using Induced-Phase Modulation in Argon-Filled Hollow-Core Fiber*, in Research in Optical Sciences. (Optical Society of America), 2014, pp. HW1C.2.
5. **S. Carbajo**, L. J. Wong, E. Nanni, D. N. Schimpf, F. X. Kärtner, *Ultra-intense Few-cycle Radial Polarization Source for Vacuum Laser Acceleration*, in Research in Optical Sciences. (Optical Society of America), 2014, pp. HTu2C.6 (**invited**).
6. W. S. Graves, K. K. Berggren, **S. Carbajo**, R. Hobbs, K. H. Hong, W. R. Huang, F. Kärtner, P. D. Keathley, D. E. Moncton, E. Nanni, K. Ravi, K. Swanwick, L. F. Velasquez-Garcia, L. J. Wong, Y. Yang, L. E. Zapata, Y. Zhou, J. Bessuille, P. Brown, E. Ihloff, S. Carbajo, J. Derksen, A. Fallahi, F. Kaertner, F. Scheiba, X. Wu, D. Mihalcea, P. Piot, Compact XFEL Light Source, in International Free-electron laser conference, Manhattan (USA), 2013).

List of refereed journal publications and conference proceedings prior to this thesis

1. C. S. Menoni, **S. Carbajo**, I. D. Howlett, W. Chao, E. H. Anderson, A. V. Vinogradov, I. A. Artyukov, K. Buchanan, M. C. Marconi, J. J. Rocca, in X-Ray Lasers 2012, S. Sebban, J. Gautier, D. Ros, P. Zeitoun, Eds. (Springer International Publishing, 2014), vol. 147, chap. 30, pp. 185-192.
2. **S. Carbajo**, *Single-shot flash imaging using a compact soft X-ray microscope*, M. Sc. thesis, Colorado State University, 2012.
3. **S. Carbajo**, I. D. Howlett, F. Brizuela, K. S. Buchanan, M. C. Marconi, W. Chao, E. H. Anderson, I. Artioukov, A. Vinogradov, J. J. Rocca, C. S. Menoni, *Sequential single-shot imaging of nanoscale dynamic interactions with a table-top soft x-ray laser*. Opt. Lett. 37, 2994-2996 (2012).
4. F. Brizuela, I. D. Howlett, **S. Carbajo**, D. Peterson, A. Sakdinawat, L. Yanwei, D. T. Attwood, M. C. Marconi, J. J. Rocca, C. S. Menoni, *Imaging at the Nanoscale With Practical Table-Top EUV Laser-Based Full-Field Microscopes*. Selected Topics in Quantum Electronics, IEEE Journal of 18, 434-442 (2012).
5. C. S. Menoni, F. Brizuela, **S. Carbajo**, Y. Wang, D. Alessi, D. H. Martz, B. Luther, M. C. Marconi, J. J. Rocca, A. Sakdinawat, W. Chao, Y. W. Liu, E. H. Anderson, K. A. Goldberg, D. T. Attwood, A. V. Vinogradov, I. A. Artioukov, B. LaFontaine,

in X-Ray Lasers 2010, J. Lee, C. Nam, K. Janulewicz, Eds. (Springer Netherlands, 2011), vol. 136, chap. 41, pp. 359-370.

6. I. D. Howlett, F. Brizuela, **S. Carbajo**, D. Peterson, A. Sakdinawat, Y. Liu, D. T. Attwood, M. C. Marconi, J. J. Rocca, C. S. Menoni, *Assesment of illumination characteristics of soft x-ray laser-based full-field microscopes*,in SPIE Proceedings (2011), vol. 8140, pp. 81405.

7. **S. Carbajo**, I. D. Howlett, M. C. Marconi, J. J. Rocca, C. S. Menoni, *Laser based aerial microscope for at-wavelength characterization of extreme ultraviolet lithography masks*, in IEEE Photonics, pp. 698-699 (2011).

8. **S. Carbajo**, I. Howlett, A. Sakdinawat, Y. Liu, W. Chao, E. H. Anderson, A. Vinogradov, I. Artioukov, D. T. Attwood, M. C. Marconi, J. J. Rocca, C. S. Menoni, *Movies of nanoscale dynamics using soft x-ray laser illumination*, in Frontiers in Optics 2011. (Optical Society of America, San Jose, California, 2011), pp. FTuL3, (*post-deadline*).

9. **S. Carbajo**, F. Brizuela, A. Sakdinawat, Y. Liu, W. Chao, W. Chao, E. H. Anderson, A. Vinogradov, I. Artioukov, D. T. Attwood, M. C. Marconi, J. Rocca, K. Buchanan, C. Menoni, *Single-Shot Imaging of Nanoscale Dynamics by Extreme Ultraviolet Microscopy*, in CLEO 2011, pp. JWA121.

10. **S. Carbajo**, F. Brizuela, A. Sakdinawat, Y. Liu, W. Chao, E. H. Anderson, A. V. Vinogradov, I. A. Artioukov, D. T. Attwood, M. C. Marconi, J. J. Rocca, C. S. Menoni, *Movies at the nanoscale using extreme ultraviolet laser light*, in Frontiers in Optics 2010. (Optical Society of America, Rochester, New York, 2010), pp. PDPB2.

11. **S. Carbajo**, F. Brizuela, D. H. Martz, D. Alessi, Y. Wang, M. C. Marconi, J. J. Rocca, C. S. Menoni, A. Sakdinawat, E. Anderson, K. A. Goldberg, D. T. Attwood, B. La Fontaine, *Laser based aerial microscope for at-wavelength characterization of extreme ultraviolet lithography masks*, in IEEE Photonics, pp. 584-585 (2010).

12. F. Brizuela, **S. Carbajo**, A. Sakdinawat, Y. Wang, D. Alessi, D. Martz, B. Luther, K. A. Goldberg, D. T. Attwood, B. La Fontaine, J. Rocca, C. Menoni, *Table-top Extreme Ultraviolet Laser Aerial Imaging of Lithorgraphic Masks*, in CLEO 2010. (Optical Society of America, San Jose, California, 2010), pp. AFA5.

13. F. Brizuela, **S. Carbajo**, A. Sakdinawat, D. Alessi, D. H. Martz, Y. Wang, B. Luther, K. A. Goldberg, I. Mochi, D. T. Attwood, B. La Fontaine, J. J. Rocca, C. S. Menoni,

Extreme ultraviolet laser-based table-top aerial image metrology of lithographic masks. Opt. Express 18, 14467-14473 (2010).

Table of contents

Table of contents **xv**

List of figures **xvii**

List of tables **xxiii**

Nomenclature **xxiii**

1 Compact Relativistic Electron and Bright X-ray Sources **1**

2 Cryogenically-Cooled Yb:LiYF$_4$ Chirped-Pulse Regenerative Amplifier **5**
- 2.1 Introduction 5
- 2.2 Motivation 5
- 2.3 Design of a Cryo-Yb:YLF Regenerative Amplifier at 1018 nm 7
  - 2.3.1 The Gain Medium 8
  - 2.3.2 ANDi Fiber Laser Seed 11
  - 2.3.3 The Grating-pair Stretcher 12
  - 2.3.4 The Fiber-Coupled Laser Diode Pump 14
  - 2.3.5 The Ring-cavity 19
  - 2.3.6 The Grating-pair Compressor 25
  - 2.3.7 Intracavity Pulse-energy Buildup Control Electronics 26
- 2.4 Preliminary Lasing Results 29
  - 2.4.1 Emission Fluorescence Spectrum 29
  - 2.4.2 Quasi-CW Operation 30
- 2.5 Future Development and Prospective Use 32

3 Power-scaling of Sub-cycle Terahertz Pulses **35**
- 3.1 Introduction 35
- 3.2 Motivation 35

3.3 Non-collinear Intrapulse Difference-Frequency Generation 37
3.4 Optical Rectification in the 800-nm Pump Region 38
 3.4.1 Influence of Pump Pulse Duration 41
 3.4.2 The Combined Effect of Angular Dispersion and Cascading 42
 3.4.3 Influence of Central Pump Wavelength 45
 3.4.4 Summary of Limiting Factors 46
3.5 Enhanced Conversion Efficiency in the 1μm Pump Wavelength Region . . 47
 3.5.1 Experimental Setup 47
 3.5.2 Conversion Efficiency at Room Temperature 48
 3.5.3 Influence of Chirp in Conversion Efficiency 50
 3.5.4 Influence of Crystal Temperature 55
 3.5.5 Intrinsic Conversion Efficiency 58
3.6 Conclusions and Remarks 59

4 Free-space Longitudinal Acceleration of Electrons 61
4.1 Introduction 61
4.2 Motivation 61
4.3 The Relativistic Few-cycle Radially-polarized Laser 62
 4.3.1 The Hollow-core Fiber Pulse Compressor 63
 4.3.2 Linear to Radial Polarization Conversion 67
 4.3.3 Source Summary 72
4.4 Longitudinal Acceleration of Electrons in Vacuum 72
 4.4.1 Experimental Design and Setup 73
 4.4.2 Experimental Results 77
 4.4.3 Model and Analysis 78
4.5 Conclusions and Remarks 81

References 83

Appendix A Solid-state Laser Materials Chart 95

Appendix B Pockels Cell Supplementary Information 97

Appendix C Laser-driven Particle Acceleration 101

List of figures

1.1 Conceptual block diagram of compact relativistic electron and bright x-ray source. 2

2.1 Full schematic of Yb:YLF regenerative CPA system. 7

2.2 Composite gain material: one piece of 25%-doped Yb:YLF (dark blue) and two undoped Yb:YLF caps (light blue). Dimensions are in mm. 8

2.3 Absorption spectrum of Yb:YLF at 80 K for polarizations parallel to c and a axis from Zapata et al. [1]. 10

2.4 Stimulated emission cross section of Yb:YLF at 80 K for polarizations parallel to c and a axis from Zapata et al. [1]. 10

2.5 Configuration of laser seed centered at 1018 nm wavelength. ISO: isolator; BPF: band-pass filter; RM: reflecting mirror; PD: photodiode; Yb SM: ytterbium-doped single-mode fiber; Yb DC: ytterbium-doped double-clad fiber. Image courtesy of Hongyu Yang [2]. 11

2.6 ANDi laser seed spectrum in linear (black) and logarithmic (blue) scales with 6 nm bandwidth. 12

2.7 Autocorrelation trace of the direct output pulse (inset) and compressed pulse. 13

2.8 Scaled schematic of folded two-grating stretcher. 13

2.9 Far-field beam exiting the stretcher, where *r* is the 1/e^2 beam waist in mm and *x* is the propagation length originating at the output grating plane in mm. 14

2.10 a) Scaled schematic of the 960 nm pump configuration and b) the corresponding beam caustic. 15

2.11 a) LDM output power, b) central wavelength, and c) bandwidth as a function of drive current and temperature. 17

2.12 Relative absorption cross-section of Yb:YLF at cryogenic-temperature for a- and c-axis, in blue and red, respectively. 18

2.13 Long-term settings of a) temperature in C, b) output central wavelength in nm, c) bandwidth in nm, and d) output power in W. The x-axis shows time in minutes. 18

2.14 Pump beam profile at focus (crystal plane) under operating conditions in Table 2.2. The above-90% top-hat beam diameter is 1.482 mm and 1.486 mm in x and y, respectively, or 1.283 mm and 1.287 mm 1/e^2 alternatively. 19

2.15 a) Structure of the model representing the composite Yb:YLF gain crystal In-bonded to a cryogenically-cooled copper sink and b) side- and c) top-view of the corresponding temperature distribution under pumping conditions described above. 20

2.16 Schematic of the ring-cavity for the seeded Yb:YLF regenerative amplifier, including pump-beam optics. 21

2.17 Schematic and relevant parameters of ring cavity. 22

2.18 a) Caustic of a stable single-mode 1018 nm wavelength pulse inside the ring-cavity and b) corresponding stability map as a function of thermal lensing strength. 23

2.19 a) Intracavity energy and fluence buildup as a function of number of passes in the cavity for the parameters in Table 2.3 and b) zoom of a) in the expected operational region. 24

2.20 Schematic of double-pass grating pair high-energy pulse compressor. . . . 25

2.21 Influence of 2.5% pump-power variation in amplified energy build-up. . . . 26

2.22 Conceptual schematic of 100 Hz trigger signal electronics and an integrated real-time intracavity energy buildup monitoring and control system. 28

2.23 Concept of seeding and Pockels cell triggering timing with most relevant time-scales. 28

2.24 Pocket cell HV trigger R-C network. 29

2.25 Measurement setup for polarization-dependent emission fluorescence from both sides of the gain medium under different pumping modes. 30

2.26 Absolute measured fluorescence power spectrum of our custom-cut Yb:YLF crystal at cryogenic temperatures, pumped by our LD module at 960 nm wavelength. The OSA resolution is 0.1 nm over a 40 nm span. 31

2.27 Extended span of measured fluorescence power spectrum pumped under same conditions as in Fig. 2.26. The 995 line is strongly suppressed. The OSA resolution is 0.2 nm over a 60 nm span. 31

2.28 Peak output power of QCW multimode ring cavity as a function of output coupler transmittance (T=0.05;0.1;0.18;0.2) and corresponding Findlay-Clay fit. 32
2.29 Slope efficiency of QCW operated ring-cavity with an output coupling T=0.18. 32
2.30 Far-field image of the beam outputting the ring cavity in single-mode QCW operation (bar is 1 mm). 33

3.1 a) Conceptual k-vector distribution in non-collinear DFG process and b) conceptual schematic of PFT OR. 36
3.2 Concept of optical cascaded frequency down-conversion. 38
3.3 Experimental layout of the THz generation by optical rectification in the 800-nm pump-wavelength region. 39
3.4 Pump spectrum from Ti:Sapphire amplifier corresponding to a measured transform-limited pulse duration of 160 fs. 39
3.5 a) Generated THz energy as a function of input optical energy at 300 K. b) Temporal waveform measured by EO sampling in 0.5 mm ZnTe. c) Retrieved broadband THz spectrum with maximum spectral content at 0.35 THz. 40
3.6 a) THz energy as a function of input optical energy for a variety of transform-limited pulse durations and b) corresponding efficiency curves. 41
3.7 Conversion efficiency as a function of peak intensity for fixed pump fluence and central wavelength. 41
3.8 One-dimensional model of saturation mechanisms for two different pulse durations, including material and angular dispersion (D), linear absorption (A), self-phase modulation (SPM) and cascading (C). The parameters used in this simulation are a fluence of 15 mJ/cm^2, a temperature of 100 K, a nonlinear refractive index n$_2$ = $2 \cdot 10^{-15}$ cm^2/W and second order susceptibility $\chi^2 = 366$ pV/m from [3]. 42
3.9 Measured THz conversion efficiency curves as a function of input optical energy, fluence, and peak-intensity, acquired by starting off the optimum conversion at lowest input energy upward (blue); and starting off at highest input energy downward (red). 43
3.10 Input and output optical power spectrum of the pump pulse for s- and p-polarization. The number of cascaded cycles of the broadened optical spectrum (red) is estimated to be about 14. 44

3.11 Generated THz energy as a function of pump central wavelength for fixed peak intensity, fluence, and bandwidth. 45
3.12 Conceptual schematic of PFT OR with 1030 nm wavelength pump. 48
3.13 Example design of caustic for a Keplerian (4f) telescope within a PFT setup valid for use in OR: L1 = 150 mm; f1 = 100 mm; f2 = 50 mm;. 49
3.14 Beam caustic for two cylindrical lenses within the PFT setup parameters listed in Table 3.1. 49
3.15 Input infrared spectrum and corresponding broadened output spectrum due to efficient THz generation. 50
3.16 a) Output THz energy as a function of input IR energy, fluence, and peak-intensity at 1030 nm pump wavelength and b) corresponding extracted conversion efficiency curve in cLN at room temperature. 51
3.17 a) Conceptual PFT OR setup of a Fourier-limited input pulse through a M = -0.5 imaging system and b) corresponding PFT change with a negatively chirped input pulse in the same setup. 52
3.18 a) Output THz efficiency as a function of input pump energy for the cases of 1.75 ps (red), 1.45 ps (black), and 1.12 ps (blue) optimal stretched pulse durations and b) corresponding conversion efficiency curves at room temperature. 53
3.19 Normalized efficiency and FWHM Gaussian-pulse duration as a function of GDD relative to Fourier-limited pulse in the cases of 1.75 ps (in red) and 1.45 ps (in blue) optimal pulse duration setups. 54
3.20 Generated THz beam profile and relative intensity with the same color scale for four different points of pump pulse GDD as in Fig. 3.19. 55
3.21 Extracted conversion efficiency as a function of cLN crystal temperature. . 56
3.22 a) Extracted conversion efficiency and b) THz energy as a function of input energy, fluence, and peak-intensity for a 1.12 ps pump pulse duration at 110 K cLN temperature. 57
3.23 Measured output pump power spectra in logarithmic scale and their corresponding extracted conversion efficiencies at 300 K. 58
3.24 Nearly diffraction-limited Gaussian THz focused beam with tangential and sagittal diameters of 0.73 mm and 0.83 mm FWHM, respectively. 60

4.1 Cylindrical vector beams are those that exhibit a transverse cylindrical symmetry of their fields, radial and azimuthal polarization being the most commonly known, and the generalized form, which is a combination of the two. 62

4.2 Detailed schematic of high-energy high-power few-cycle radially polarized laser based on an Ti:Sapphire ultrafast laser system, a hollow-core fiber compressor and broadband polarization-mode converter. 63

4.3 a) Representative input ultrashort pulse and intensity carrier envelope. b) Instantaneous self-induced frequency shift and c) spectral broadening due to self-phase modulation. 65

4.4 Schematic of pressure gradient HCF compressor that assists in avoiding self-focusing and ionization losses. 66

4.5 a) Normalized input spectrum (gray), normalized output spectrum (solid cyan), and waveplate transmission curve (dashed cyan); (b) measured interferometric autocorrelator (IAC) signal (dashed cyan) and fitted IAC signal with a 8.06 ± 0.15 fs FWHM pulse duration, waveguide output far-field beam profile (inset); bar is 5 mm. 68

4.6 Computed coupling efficiency as a function of electric field beam waist of linearly polarized Gaussian EH_{11} (solid) and EH_{12} (dashed) beams and linearly polarized Gaussian beam externally converted to TM_{01} (dotted) mode. 69

4.7 Segmented waveplate (SWP): polarization mode converter. 70

4.8 The polarization purity is calculated directly from the visibility of the recorded images after mode conversion. 71

4.9 Normalized transverse far-field intensity profile of 8 fs radially-polarized beam for (a) full beam, (b) 0-degree angle, (c) 45-degree angle, (d) 90-degree angle, and (e) 135-degree angle components. 71

4.10 Concept of vacuum laser acceleration in a co-linear scheme using relativistic radially polarized laser pulses. 73

4.11 Colormap of spatial field distribution of a $\lambda_0 = 800nm$, $w_0 = 1.2\mu m$; 3-cycle FWHM; and 600 μJ radially polarized laser beam focused by a NA=1 perfect lens centered at a) waist (maximum intensity and interaction point) and b) 40 fs after a). 74

4.12 Concept of vacuum laser acceleration in a co-linear scheme using relativistic radially polarized laser pulses. 75

4.13 Technical drawing of 40 keV DC electron gun and interaction chamber. . . 76

4.14 Electron-laser beam coincidence timing and normalized charge of detected accelerated electrons as a function of laser-electron timing delay (τ). . . . 77

4.15 Accelerated electron counts contained in the deflector plane at $\tau = 0$ 78

4.16 Snapshots of the normalized distribution in real- and momentum-space of accelerated electrons at four different temporal overlaps (linked to Fig. 4.14: (i) there are no accelerated electrons when the initial electron bunch arrives at the IP 8.5 ps before the laser; (ii) distribution at the peak of total accelerated charge (τ = 0) them beam is delayed by (iii) 4.25 ps and (iv) 8.5 ps with respect to the laser field. 79
4.17 a) Modeled final electron kinetic energy as a function of azimuthal angle in the region of study with half-angle deflection of less than 25 mrad and b) corresponding histogram as a function of divergence in the kinetic energy region ranging from 42 keV to 53 keV. 80
4.18 a) Modeled final electron kinetic energy as a function of azimuthal angle in the region of study with half-angle deflection of less than 25 mrad and b) corresponding histogram as a function of divergence in the kinetic energy region ranging from 42 keV to 53 keV. 80

A.1 Relevant SSL material properties for Yb:YLF, Yb:YAG, Yb:CaF$_2$, Yb:SrF$_2$, and Tm:YAG. Chart completed by Chris Barty at LLNL and Luis Zapata at MIT LL. 95

B.1 $\lambda/2$-retardation driving voltage of the KD*P Pockels Cell (1042 series). . . 97
B.2 Technical drawing of the assembled PC-retarder. 98
B.3 Main parameters of 1040 series KD*P Pockels Cells. 98
B.4 PC materials standard parameters chart. 99
B.5 Measured and calculated nonlinear indices of refraction of optical crystals [4, 5]. 99

C.1 Particle net kinetic energy gain histogram. 101
C.2 Final kinetic energy electron distribution (colormap) 10 ps after laser collision in real-space as a function of transverse dimension (x) and longitudinal dimension (z). 102
C.3 Final kinetic energy electron distribution 10 ps after laser collision as a function of azimuthal angle. 102

List of tables

2.1 Grating-pair stretcher parameters 14
2.2 Nominal values of diode pump operation parameters 16
2.3 Design parameters for Frantz-Nodvik calculations 24
2.4 Grating compressor parameters 25
2.5 Maximum nominal fluence on cavity optical elements 27

3.1 Design parameters of PFT OR setup at 1030 nm 48
3.2 Cascaded broadening at 300 K and estimated intrinsic conversion efficiency 59

4.1 Quick facts: pros and cons of polarization mode conversion before or after spectral broadening in hollow-waveguide 70
4.2 Few-cycle radially-polarized source summary 72

Chapter 1

Compact Relativistic Electron and Bright X-ray Sources

Since their discovery in 1895 [6], x-rays have become the most utilized probe to determine the structure of matter employing increasingly powerful techniques such as microscopy [7–9], diffraction [10–12], and spectroscopy [13–15]. Current benchmarking x-ray radiation sources —based on relativisitic electron bunches from synchrotrons or linear accelerators—have sufficient brilliance in the hard x-ray photon energy range to unveil structural dynamics of matter at relevant atomic spatial and temporal scales [16–18].

In these machines, electron beams are generally produced by thermionic- or photocathodes, then accelerated by radio-frequency (RF) cavities operating in the range of a few GHz, and finally oscillated by wiggler or undulating magnets to produce x-rays [19–21]. State-of-the-art facilities such as LCLS and the future European XFEL are linear accelerators (LINAC) capable of producing highly relativistic electron bunches, of the order of several GeV. The main limitation imposed in their accelerating gradients arises from field-emission from the cavity walls [22], typically in the range of tens of MeV/m at their operating frequencies. As a consequence, their length must be extended to the kilometric range in order to reach highly relativistic electron velocities, which brings the ratio of produced knowledge to construction and maintenance cost dramatically low. However, the uniqueness of these machines enables scientists to generate knowledge —otherwise unattainable—that underpins the understanding of our physical world, from sub-atomic scales to the observable universe. On these grounds, the development of any generalized form of compact relativistic electron and x-ray source is of unarguable relevance and general public interest since it could bring widespread access, practicality, and orders of magnitude cost reduction to the same scientific and technological questions.

The path towards such a global goal is not paved yet, and there are several different opportunities to tackle the challenge [23–29]. In this context, this thesis reports on fundamental experimental advances in key technologies contributing to the development of a compact relativistic electron source and high-brilliance attosecond x-ray source based entirely on optical and terahertz technology. The baseline strategy explores the development of a terahertz-based electron gun and accelerator combined with coherent inverse Compton scattering from an optical laser for highly efficient x-ray emission, as depicted in Fig. 1.1. The promise behind this general idea is that coherent x-ray generation is possible directly from longitudinally modulated electron beams. The content of this thesis presents significant progress in this direction within three major thrusts: (i) high-power laser source development, (ii) efficient terahertz radiation, and (iii) acceleration of electrons with optical fields in vacuum; each of which is summarized in independent chapters.

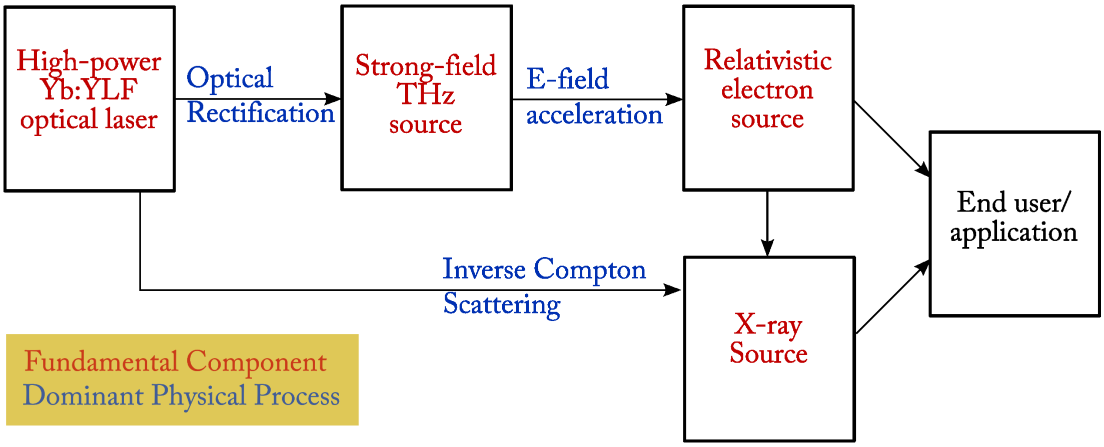

Fig. 1.1 Conceptual block diagram of compact relativistic electron and bright x-ray source.

Chapter 2 covers content from a full-design to preliminary experimental results of an ultrafast mJ-level cryogenic-Yb:YLF regenerative amplification laser system. Cryogenic-Yb:YLF is a relatively unexplored laser technology that holds promise for high-energy high-power optical technology at kilohertz repetition rates and sub-picosecond pulse durations for its relatively high and broadband emission cross-section and saturation fluence at around 1018 nm wavelength. The presented design represents the first step towards building a cryogenic-Yb:YLF chirped-pulse amplification laser system operating above 100 mJ energy level and 700 fs pulse duration at above 1 kHz repetition rate. The implications of such a laser system within the scope of the proposed approach are twofold. First, the relatively large bandwidth of the laser line is ideal for driving nonlinear optical rectification processes to generate terahertz radiation efficiently. In addition, cryogenic-Yb:YLF technology can also be used as an inverse Compton scattering source, that is, an optical undulator with a period on the order of its wavelength (1 μm). Employing four orders of magnitude shorter undulating periods than that of typical magnetic undulators (1) shrinks down the undulating structure to the cm-scale and (2) decreases the required electron beam energy to achieve Angstrom-wavelength x-ray radiation, from the few-GeV to the several-MeV level.

Chapter 3 is dedicated to a thorough theoretical and experimental study of efficient terahertz generation and its scaling limitations. The main rationale behind studying efficient methods to generate terahertz radiation is that employing accelerating frequencies two orders of magnitude higher, i.e. in the terahertz range, than those of conventional RF accelerators brings a few fundamental advantages. First, the field emission threshold for surface electric field increases to the multi-GV/m range. High operating frequencies and fields also make bunch compression to the attosecond regime possible. To set an example, THz pulsed beams could first accelerate electrons freed at the field maximum in each cycle in any generalized emitter structure, namely a terahertz gun, and then boost their kinetic energy to relativistic regime in an accelerating structure, for instance, in a dielectric waveguides or directly in free-space. Their sub-mm wavelength allows for pC-level charges and makes it possible to achieve relativistic laser-electron interactions with multi-mJ energy levels. THz-driven relativistic electron sources can therefore impact future linear particle accelerators or compact high-flux x-ray sources. In this chapter, we explore a THz generation method based on a broadband frequency down-conversion process from optical laser pulses in a nonlinear crystal with record energy conversion efficiencies in the few-percent level from mJ-level ultrafast lasers.

Finally, Chapter 4 reports on a first demonstration of electron acceleration in a purely free-space environment using a relativistic radially-polarized optical laser. Over the last few decades, some of the compact laser-based acceleration methods have shown outstanding performances in certain cases exceeding those of conventional RF accelerators. These methods still face several challenges that hamper their practical use. In all cases, their limitations arise primarily from the use of a medium to assist in the laser-to-particle energy transfer. In this chapter, we experimentally demonstrate for the first time a novel acceleration method that requires no medium in assisting laser-particle interactions and is thereby unrestrained from limitations found in any other methods. The chapter describes in detail the development of a few-cycle radially polarized source and the demonstration of laser-based longitudinal electron acceleration, producing highly-directional longitudinal accelerating gradients in the GeV/m range. This method is capable of accelerating charged-particles from rest to relativistic velocities within the ultrashort interaction with a few-cycle laser pulse, and thus avoid inhomogeneities arising from Coulomb interactions. Moreover, this type of accelerator can generate well-collimated tunable attosecond electron bunches and x-ray pulses. The results from this chapter are directly transferable to any laser frequency, including the THz range.

This abstract is meant to provide an overall motivation for combining various independent research topics. In context, these research areas are tightly intertwined. In order to restrain our attention to each of the different topics in more detail and provide further insight than that depicted in this introductory chapter, the following chapters are self-contained. The global ambition for a compact relativistic electron and high-brilliance attosecond x-ray source will nonetheless be evoked in further detail throughout the dissertation. All things considered, the set of demonstrations presented in all three following chapters represent no other than a leap in the feasibility of novel future compact x-ray sources with the mission of bringing widespread access to groundbreaking x-ray based scientific, technological, and medical tools.

Chapter 2

Cryogenically-Cooled Yb:LiYF$_4$ Chirped-Pulse Regenerative Amplifier

2.1 Introduction

This chapter aims to provide a detailed summary of the design of a high-power high-energy source based on cryogenic Yb^{3+}-doped LiYF$_4$ (Yb:YLF) laser technology. We will address the properties that make this technology a powerful driving source for the various applications of high-harmonic generation (HHG), optical parametric chirped-pulse amplification (OPCPA) technology, x-ray sources based on inverse Compton scattering (ICS) and both broadband and narrowband terahertz (THz) generation, among others. The chapter will conclude with a set of preliminary experimental results and remarks for future direction.

2.2 Motivation

Solid-state lasers with high-energy at kHz repetion rates are continuously pushed towards even shorter and more energetic pulses in order to increase the operating regime span of existing state-of-the-art systems. Cryogenic Yb^{3+}-doped lasers are particularly interesting en route to new lasing regime frontiers because of their low quantum defect and improved thermo-optic properties at cryogenic temperatures [30, 31]. In general, operating solid-state lasers with their gain media cooled to cryogenic temperatures has two fundamental advantages compared to room-temperature operation: (i) host crystals exhibit much better thermo-optic properties and (ii) the thermal population of the lower excitation level is significantly reduced.

These properties have led excellent performances of cryogenically-cooled Yb:YAG lasers

[32], for example, with stable high average power operation in the kW range and several J energies [33, 34]. However, in terms of scalability towards shorter pulse durations, amplification based on Yb:YAG suffers from its narrow emission bandwidth at cryogenic temperatures, which results in final bandwidths narrower than 0.5 nm and thereby limits the pulse width to a few ps [35]. Yb:YLF has been demonstrated to be a promising alternative because of its much broader emission cross section bandwidth supporting 200 fs pulse durations and favorable thermo-optic properties in cryogenic operation [36, 37]. Also, YLF is an attractive host material because it is uniaxial and thus stress-induced birefringence is negligible compared to its natural birefringence.

Yb:YLF is nonetheless a relatively unexplored material still today. Kawanaka *et al.* from CREST, Japan, have made significant progress in characterizing the spectroscopic properties of Yb:YLF and developing laser system in CW, Q-switching, and chirp-pulse amplification, achieving above 100 mJ-energy chirped-pulse amplification (CPA) at low repetition rates and below 700 fs compressed pulse durations, although not simultaneously [36–39]. Fan *et al.* at MITLL, USA, have also strongly contributed to the development of Yb:YLF systems, with comparable results to those reported by the Japanese group [1, 40, 41].

The following are the most remarkable material parameters of Yb:YLF at cryogenic temperatures (for a more complete gain medium comparison see Fig. A.1 in Appendix A):

- Cryogenically-cooled Yb:YLF exhibits an emission cross section 15 times higher than that at room temperature.

- Its saturation fluence also reduces dramatically from 114 J/cm^2 to 13 J/cm^2, which is suitable for high-energy and high-average power amplification.

- The thermal conductivity in undoped YLF is 24 W/mK at 100 K (vs. 5.3 W/mK at 300 K) along the a-axis. For the c-axis, it is 34 W/mK at 100 K (vs. 7.2 W/mK at 300 K).

- At 100 K, dn_e/dT is -0.5 ppm/K and dn_o/dT is -1.8 ppm/K (vs. -4.6 and -6.6 ppm/K, respectively, at 300 K).

- The thermal expansion coefficient is 2.4 ppm/K along the a-axis and 3.2 ppm/K along the c-axis at 100 K (vs. 14 and 10 ppm/K, respectively, at 300 K).

Yb:YLF has two high stimulated emission gain cross section lines:

1. **At 995 nm**, with the polarization parallel to the crystallographic c-axis. This gain line is particularly well suited for high average-power OPCPAs and ICS drivers due to its

small quantum defect, high gain, and relatively narrow bandwidth capable of producing high-energy and high repetition-rate few-ps pulses. This region also supports high gain of two simultaneous narrowband lines at 993 nm and 996 nm (see Fig. 2.4) for difference-frequency-generation (DFG) in the THz range.

2. **At 1018 nm**, with the polarization set parallel to the crystallographic a-axis. The emission cross-section exhibits a broad pedestal with a bandwidth capable of supporting 200 fs pulses. Amplified bandwidths of this line are ideal for THz generation through optical rectification. Kawanaka *et al.* demonstrated a cryogenic chirped-pulse Yb:YLF regenerative amplifier that delivered a pulse energy of 36 mJ and pulse durations of 795 fs [36]. A repetition rate as high as 10 kHz was reported as well from a Yb:YLF regenerative amplifier, with a pulse energy of 1 mJ and an amplified full-width-at-half-maxiumum (FWHM) spectral bandwidth of 2.22 nm [40]. Amplified bandwidths of this line are ideal for THz generation through optical rectification. This technology, combined with external pulse compression techniques, is also able to provide multi-kHz multi-mJ ultrashort pulse durations as a driver for OPCPA technology and attosecond science studies.

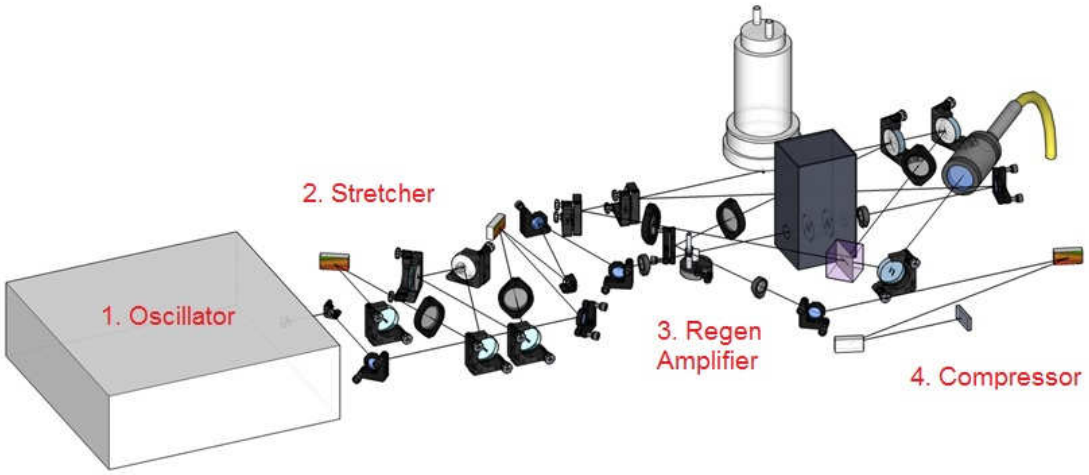

Fig. 2.1 Full schematic of Yb:YLF regenerative CPA system.

2.3 Design of a Cryo-Yb:YLF Regenerative Amplifier at 1018 nm

In this section we review the main design parameters of the chirped-pulse Yb:YLF regenerative amplifier at 1018 nm operating at cryogenic temperatures, as well as the preliminary performance of some of the integrated components. Fig. 2.1 shows the general to-scale schematic of the Yb:YLF CPA system and its main block-components: the oscillator seed laser, the temporal pulse stretcher, the regenerative amplification cavity, and the temporal pulse compressor.

2.3.1 The Gain Medium

The starting materials are high-purity, laser-grade, single-crystals with no imperfections (no bubbles, inclusions, striations, birefringence). The crystallographic orientation is such that the gain profile is predominant in the a-axis, that is, the c-axis is rotated 10 degrees from the direction of propagation, so that (i) the 995 nm emission line is suppressed and (ii) its natural birefringence dominates over the thermal-stress-induced birefringence. Thermally-induced birefringence can be characterized by depolarization coefficient and thermal lens (phase distortions). The latter may be highly anisotropic.

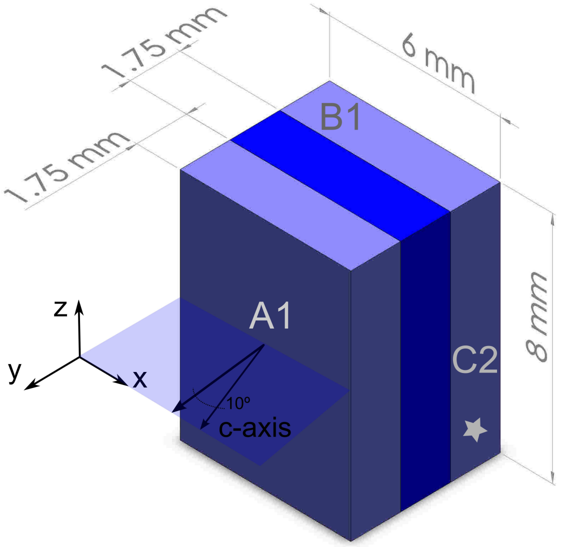

Fig. 2.2 Composite gain material: one piece of 25%-doped Yb:YLF (dark blue) and two undoped Yb:YLF caps (light blue). Dimensions are in mm.

The starting materials are coupons of undoped YLF and 25% Yb:YLF. These coupons have been cut such that the c-axis lies oriented off the large face normal by 10 degrees with respect to y-axis in Fig 2.2. A black dot on top of the short side of the coupons denotes the y-axis orientation as depicted in the figure.

The composite crystal consists of two undoped 8-mm × 6-mm × 1.75-mm ± 0.25-mm YLiF$_4$ (YLF) crystals Adhesive-Free-Bonded to a 8-mm × 6-mm × 1.75-mm ± 0.25-mm thick 25%-doped Yb:YLF gain-crystal. The crystal is then cut and polished to the final dimensions, 8-mm × 6-mm × 5.25-mm ± 0.75-mm.

The 25%-doped Yb:YLF crystal is sandwiched between the two undoped YLF ends to create a composite crystal. The interfaces are defect free over the entire bonded surfaces. Surfaces A1 and A2 (Fig. 2.2) are polished to 90 ±0.05 degrees relative to surface C1 and has a minimum wedge angle in the range of 6 to 12 arcmins relative to the x-axis. There is no parallelism specification between surfaces B1 and B2 nor between surfaces C1 and C2.

The following are the surface finish specifications:

1. A1, A2: High damage-threshold, laser grade polish.
    - Flatness: $\lambda/10$ or better at λ =632 nm over central 80%.
    - Scratch dig 10/5 or better over central 80% of surface.
2. B1, B2: Fine grind (diffuse finish) using 600 silicon carbide or equivalent.
3. C1, C2: Fine grind (diffuse finish) using 600 silicon carbide or equivalent.

While the optical coating specifications are (angles measured relative to crystal face normal):

1. A1, A2: High damage-threshold AR coating (>10 J/cm2 @ 10 ns)
    - λ=1020 nm R<0.2% at 0 degrees for both polarizations.
    - λ=960 nm R<1% over ±5 degrees for both polarizations.
    - Full aperture coverage to within 0.5 mm of the edges
2. B1, B2: No coating.
3. C1, C2: No coating.

For a 1 μm randomly polarized laser beam propagating through the crystal perpendicular to A1, entering and exiting through faces A1 and A2, the reflectivity at the interface between the 25%-doped Yb:YLF and the undoped YLF is <0.1 % while the single-pass depolarization loss is <1%.

The absorption and emission cross sections of Yb:YLF at 80 K are shown in Fig. 2.4. It is worth noting that the crystal can be very efficiently pumped at 960 nm and that there is a 7 nm emission band centered at around 1018 nm band with a cross section above $0.8{\cdot}10^{-20}$

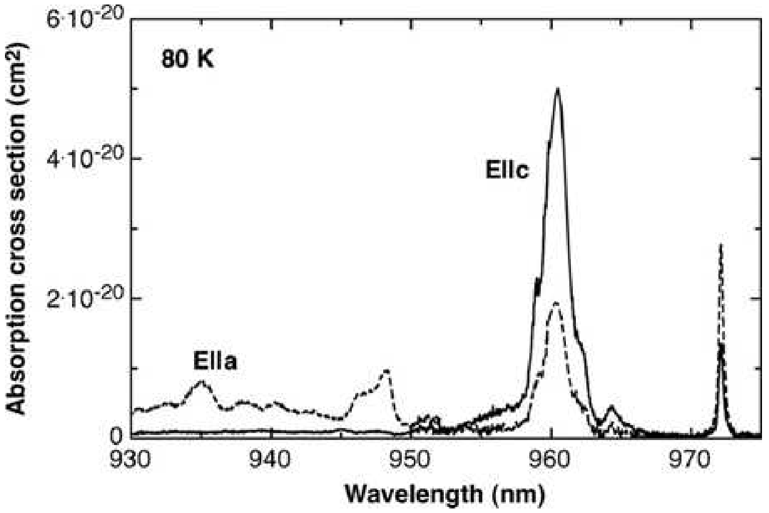

Fig. 2.3 Absorption spectrum of Yb:YLF at 80 K for polarizations parallel to c and a axis from Zapata et al. [1].

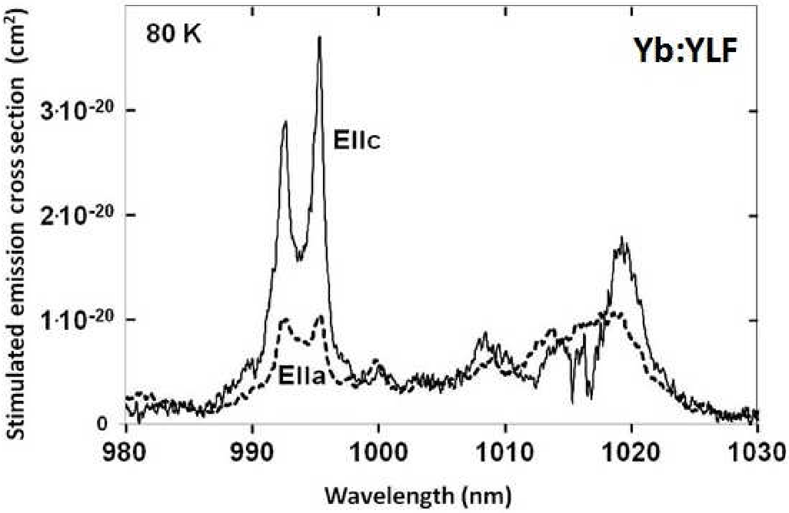

Fig. 2.4 Stimulated emission cross section of Yb:YLF at 80 K for polarizations parallel to c and a axis from Zapata et al. [1].

cm^2. Let us remind ourselves that our custom crystal cut aims to suppress significantly the c-axis emission line as seen in Fig. 2.4 in order to avoid parasitic lasing at around 995 nm. We will confirm experimentally such performance in latter sections of this chapter.

2.3.2 ANDi Fiber Laser Seed

A conceptual schematic of the seed laser is shown in Fig. 2.5. It consists of an oscillator, a fiber stretcher, a bandpass filter, and a fiber amplifier. The oscillator is an all-normal dispersion (ANDi) fiber laser [42], using nonlinear-polarization rotation (NPR) and a spectral filter as the mode-lock mechanisms.

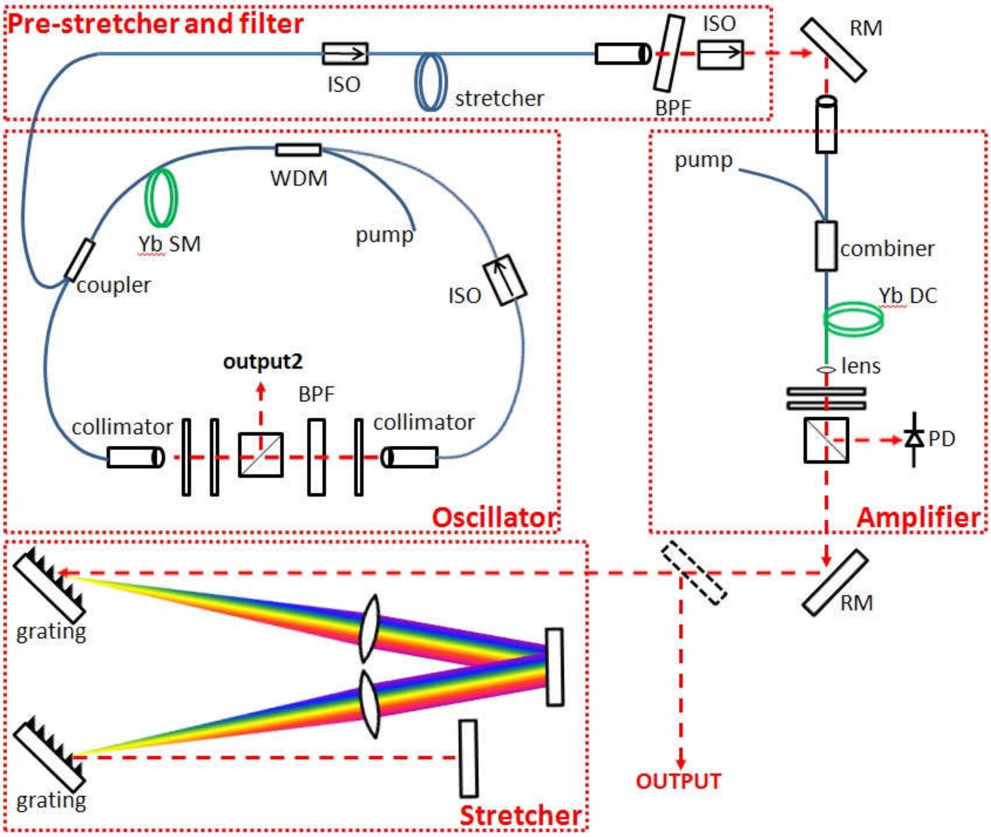
Pre-stretcher and filter
ISO
stretcher
ISO
BPF
RM
WDM
Yb SM
pump
coupler
ISO
output2
BPF
collimator
collimator
Oscillator
pump
combiner
Yb DC
lens
PD
Amplifier
grating
grating
RM
OUTPUT
Stretcher

Fig. 2.5 Configuration of laser seed centered at 1018 nm wavelength. ISO: isolator; BPF: band-pass filter; RM: reflecting mirror; PD: photodiode; Yb SM: ytterbium-doped single-mode fiber; Yb DC: ytterbium-doped double-clad fiber. Image courtesy of Hongyu Yang [2].

The first segment of wavelength-division multiplexing (WDM) isolator fiber is about 1400 cm. The Yb-fiber is 25 cm Yb1200-4/125 highly doped fiber. The third part of the coupler-collimator fiber is about 50 cm. A bandpass filter (BPF) with 3.5 nm bandwidth and flat-top shape was employed to facilitate mode-locking and tune the central wavelength of the spectrum in order to cover 1018 nm. Since the Yb-4/1200 fiber does not have a high gain at 1018 nm, careful adjustment is needed to mode-lock the laser using this 3.5 nm narrow bandpass filter. We use a 40:60 coupler and the 60% portion is coupled out into a fiber-based isolator and then launched into a segment of 20 m long HI-1060 fiber stretcher.

Another BPF is employed and tuned between the stretcher and the double-clad amplifier to select the signal wavelength for amplifying and cut unwanted signal spectrum. Removing the BFP shifts the output spectrum from the amplifier to wavelengths higher than 1030 nm. The amplifier consists of a (2+1) beam combiner and 50 cm of absorption-flattened Yb-doped double-clad fiber (FP fiber). This kind of FP fiber has a higher gain at 1018 nm than 1030 nm or higher wavelength, enabling efficient amplification.

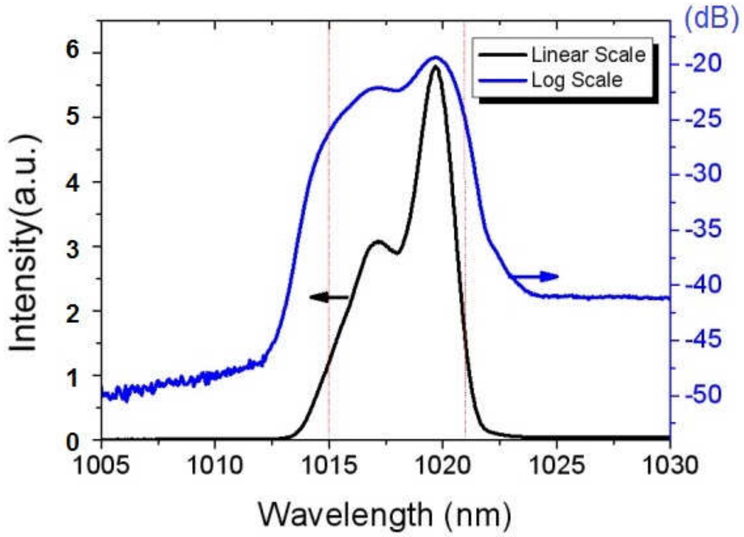

Fig. 2.6 ANDi laser seed spectrum in linear (black) and logarithmic (blue) scales with 6 nm bandwidth.

The seed oscillator works at repetition rate of 12.86 MHz using a 976 nm pump with 300 mW optical power. The output spectrum is shown in Fig. 2.6. The output pulse from the coupler in the oscillator has a pulse duration around 3 ps. After the fiber stretcher and band-pass filter, the direct output pulse width is 4.3 ps (Fig. 2.7 inset). With 1 W multimode 976 nm optical pumping, 450 mW at 1018 nm narrow band output is achieved, corresponding to 35 nJ pulse energy. A pair of diffraction gratings with 600 lines/mm and distance of 30 cm compressed the amplified pulses and the autocorrelation trace of the compressed pulse is 781 fs, (transform-limited pulse width is 513 fs). The pedestals in the compressed pulse arise from uncompensated high order dispersion introduced by the grating pair, which can be compensated for by prism pairs at the expense of a small loss.

2.3.3 The Grating-pair Stretcher

Figure 2.8 shows the schematic design of the grating-pair stretcher. The stretcher is folded for compactness, where the telescope lenses are a distance $2f$ apart from each other and

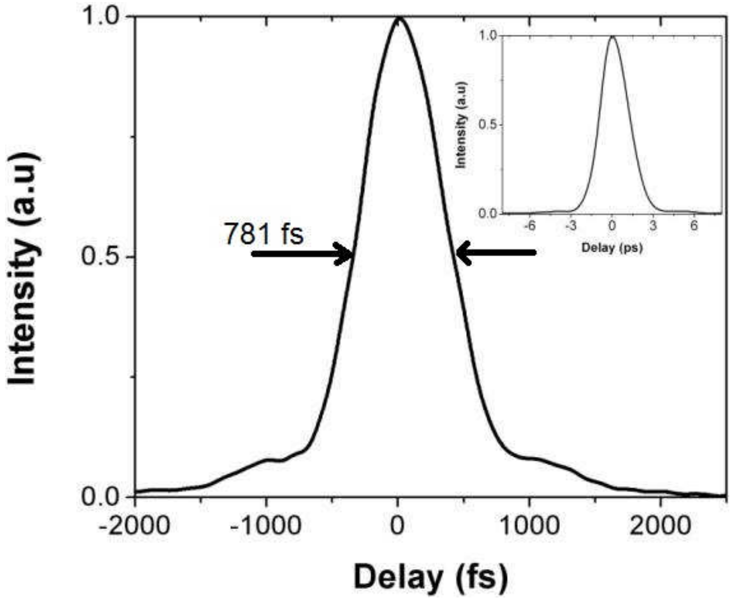

Fig. 2.7 Autocorrelation trace of the direct output pulse (inset) and compressed pulse.

each grating is at a distance *L* from the nearest telescope lens.

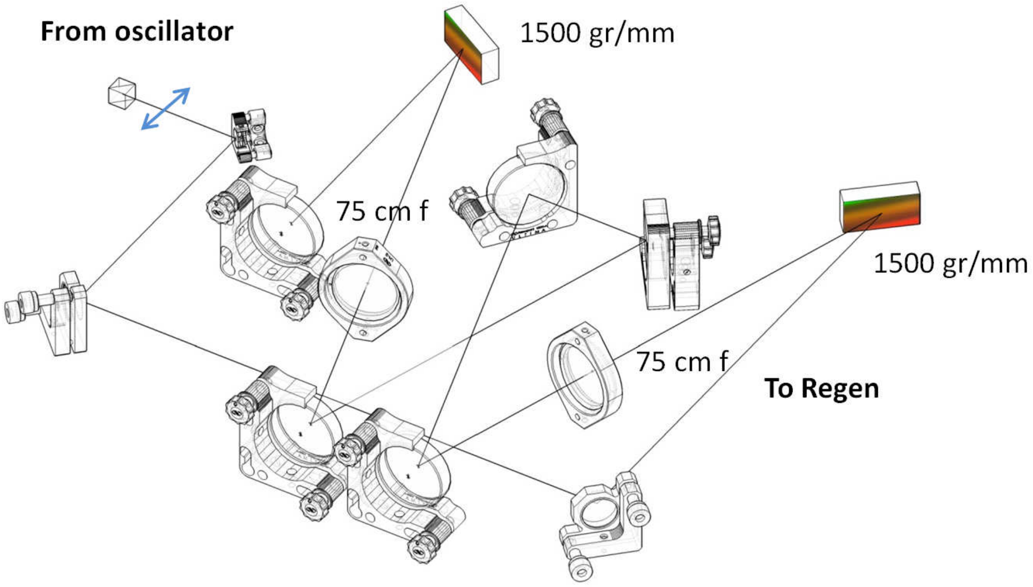

Fig. 2.8 Scaled schematic of folded two-grating stretcher.

The efficiency of each of the gratings is 94% at 1030 nm while total efficiency of the stretcher is 67.5% (71 % is the theoretical maximum) and it has a footprint of about 1 square foot. The seeded pulse from the ANDi fiber laser at the output of this grating-pair is stretched to a measured pulse duration of 260 ps FWHM (Gaussian fit), which resembles

Table 2.1 Grating-pair stretcher parameters

Grating line density	1500 lines/mm
Incidence angle	42 degrees (8-deg from Littrow)
Diffraction angle	59.4 degrees
Focal length (f)	750 mm
Lens-grating distance (L)	500 mm
GDD (2nd order dispersion)	$3.1 \cdot 10^7$ fs^2
TOD (3rd order dispersion)	$-3 \cdot 10^8$ fs^3
FOD (4th order dispersion)	$4.7 \cdot 10^9$ fs^4
Pulse duration	275 ps (assuming a 5 nm BW)

the seed spectrum lineshape. The beam from the stretcher exhibits a divergence of 1.7 mrad, and is p-polarized. The far-field beam propagation factors are shown in Fig. 2.9.

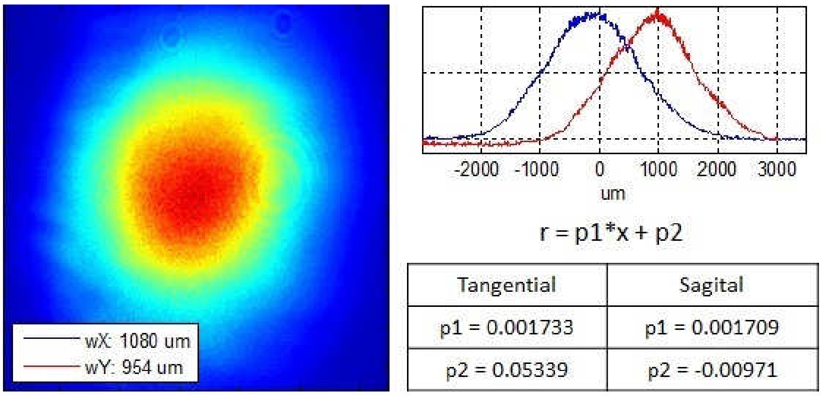

r = p1*x + p2

Tangential	Sagital
p1 = 0.001733	p1 = 0.001709
p2 = 0.05339	p2 = -0.00971

Fig. 2.9 Far-field beam exiting the stretcher, where r is the 1/e^2 beam waist in mm and x is the propagation length originating at the output grating plane in mm.

2.3.4 The Fiber-Coupled Laser Diode Pump

We utilize a commercially available fiber-coupled laser diode module (LDM) from Laserline, GmbH. The LDM offers flexible settings to adjust wavelength and bandwidth at a given operation current and duty cycle. The LDM operates quasi-CW (QCW) at a variable repetition rate and duty cycle, typically from 100 Hz to 1 kHZ at 20% duty cycle, since the upper level lifetime of Yb:YLF is about 2 msec. The typical LDM rise time is about 75 μsec.

We choose to pump the Yb:YLF crystal simultaneously from both sides for uniformity, as shown in Fig. 2.10. The pump beam coming out of the LDM laser head is collimated at 1 inch in diameter, unpolarized, with a variable central wavelength at around 960 nm, 2 nm bandwidth, and 250 W nominal power. That beam is split into two symmetric arms by a polarizing beam splitter (PBS) and is focused onto the crystal using a single f = 500 mm lens with a waist of 0.75 mm. The LDM provides a nominal power level of 250 W (125 W per arm) with 20% duty factor (100 Hz, 2 ms gated pump). The penetration depth is 150 cm^{-1}. The heating is kept relatively low due to a quantum-defect of 6.5%.

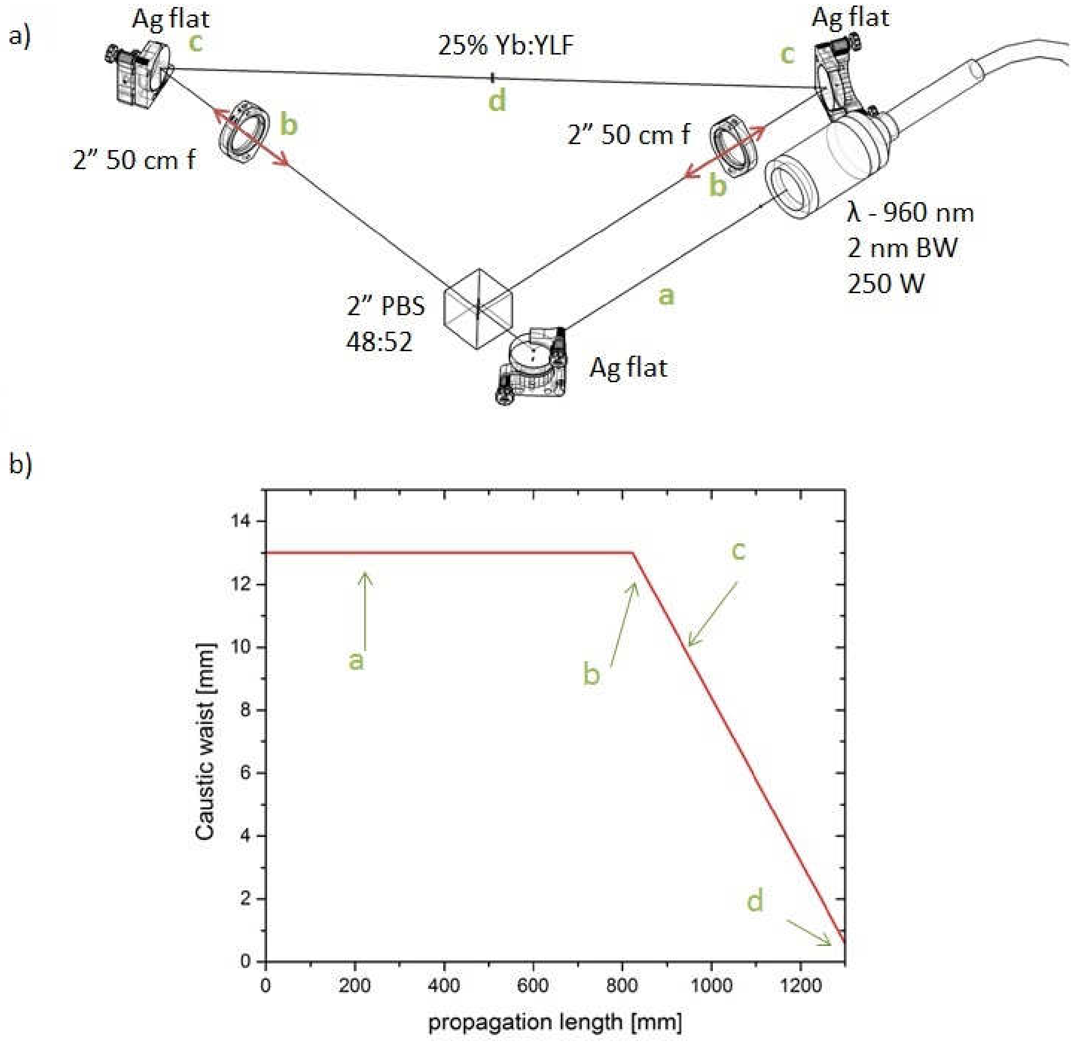
a)
Ag flat
c
25% Yb:YLF
Ag flat
c
d
b
2" 50 cm f
2" 50 cm f
b
λ - 960 nm
2 nm BW
250 W
a
2" PBS
48:52
Ag flat
b)
Caustic waist [mm]
propagation length [mm]
0
2
4
6
8
10
12
14
0
200
400
600
800
1000
1200
a
b
c
d

Fig. 2.10 a) Scaled schematic of the 960 nm pump configuration and b) the corresponding beam caustic.

In order to determine the optimal operation conditions of the LDM, we characterize its output power, central wavelength, spectrum, and bandwidth, as a function of operating current and temperature in CW operation. These results are summarized in Fig. 2.11. From the figures, we observe that, as expected, the output power grows linearly with drive current, and so does the central emission wavelength. We observe that spectral broadening of the

Table 2.2 Nominal values of diode pump operation parameters

Frequency	100 Hz
Pulse duration	2 msec
Duty cycle	0.2
Drive Voltage	10 V
Temperature setting	31 C
Temperature reading	30 C
Central Wavelength	959.85 nm
Bandwidth	2.913 nm
Average Power	53.6 W
Peak Power	268 W

emission spectrum rules at higher operating temperatures. Within this operating regime, the bandwidth remains well within the absorption cross-section (see Fig. 2.12 for a zoomed view around 1018 nm) for optimum conversion. We also characterize the long-term stability and operation of the pump, which is summarized in Fig. 2.13. From these results, we set the optimal operation parameters for our preliminary experiments, as summarized in Table 2.2. We will assume these settings hereafter unless otherwise specified.

We have mentioned earlier that YLF exhibits a few favorable factors at cryogenic temperatures for power scaling: the thermal conductivity increases, the thermal expansion coefficient decreases, and the dn/dT also decreases. In this context there are three different effects that are important to consider:

1. The refractive index of the host material (YLF) will change with temperature. The index of refraction across the crystal will exhibit a non-uniform transverse profile and thus introduce a lensing power proportional to it. YLF has a negative thermo-optic coefficient which leads to negative thermal lensing.

2. The crystal structure expands and compresses with temperature, which results in bulging of the end faces. This is of special relevance in rod type crystals. As a consequence, the bulging effect defines a weakly positive lens along the resonator axis.

3. The non-uniform expansion of the sandwiched crystal structure leads to stress in the crystal, which also changes the refractive index, leading to stress-induced birefringence.

In order to compensate for the thermal lensing effect, we estimate its strength using a finite element environment for partial differential equation to account for the amount of

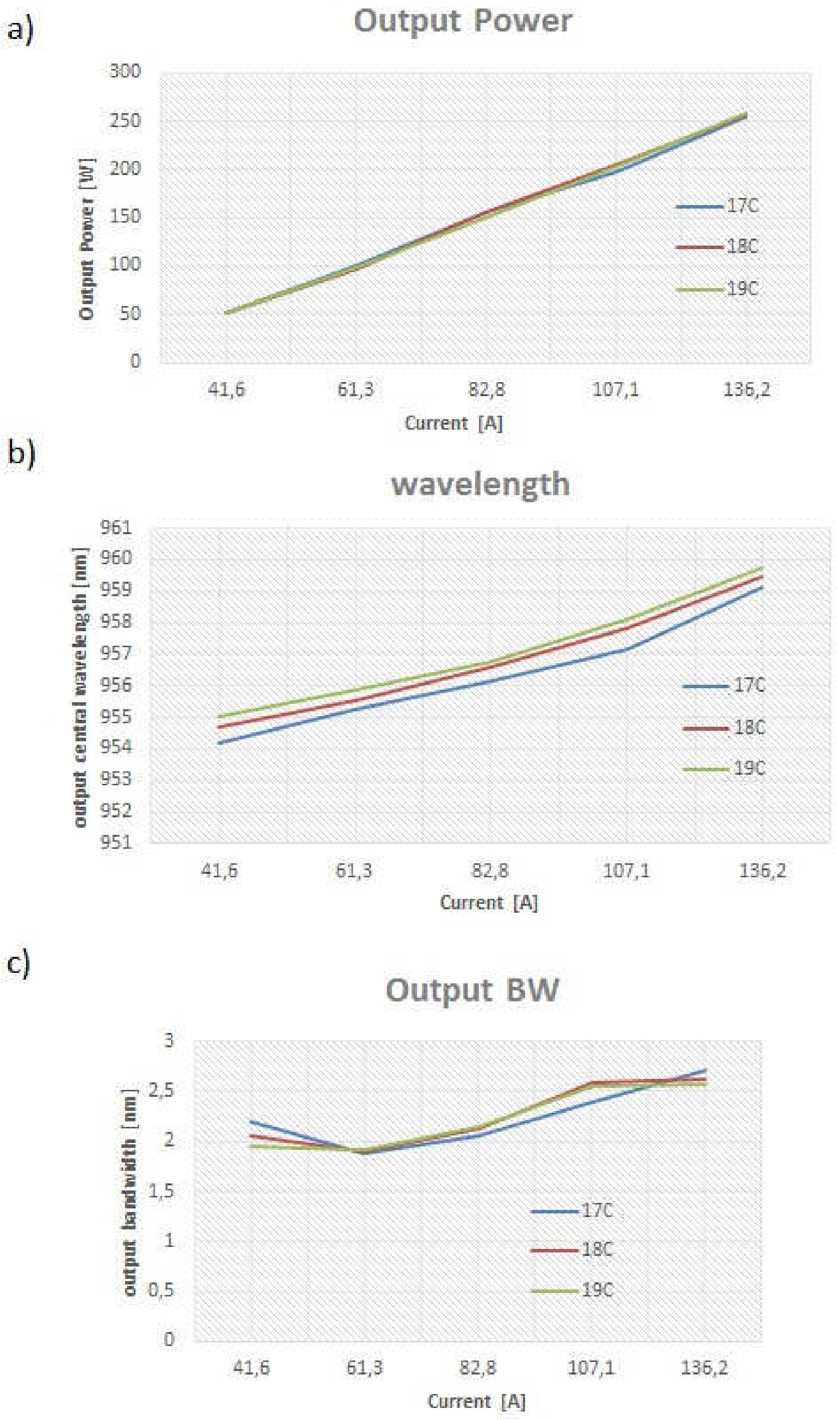

Fig. 2.11 a) LDM output power, b) central wavelength, and c) bandwidth as a function of drive current and temperature.

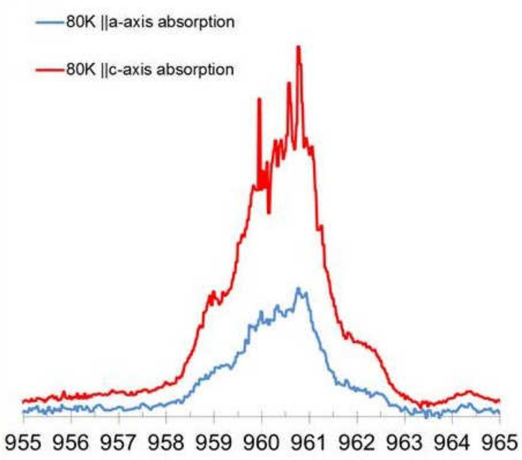

Fig. 2.12 Relative absorption cross-section of Yb:YLF at cryogenic-temperature for a- and c-axis, in blue and red, respectively.

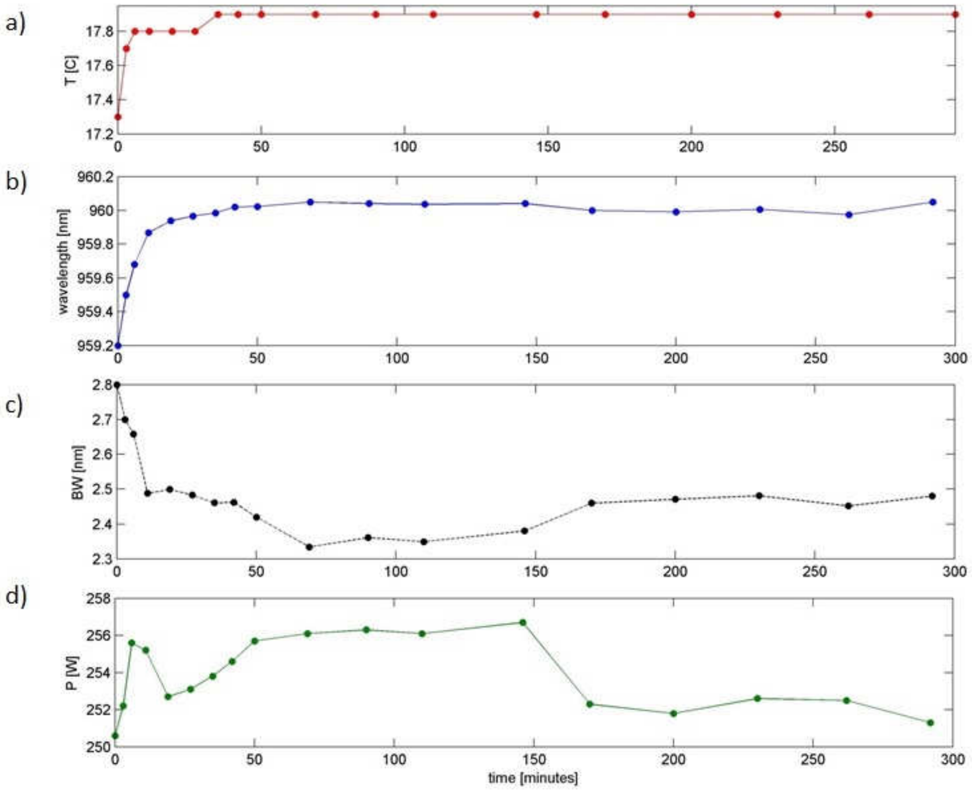

Fig. 2.13 Long-term settings of a) temperature in C, b) output central wavelength in nm, c) bandwidth in nm, and d) output power in W. The x-axis shows time in minutes.

pump absorption-induced thermal distribution of our crystal structure under the aforementioned pumping conditions [43]. The thermally induced transverse and longitudinal profiles

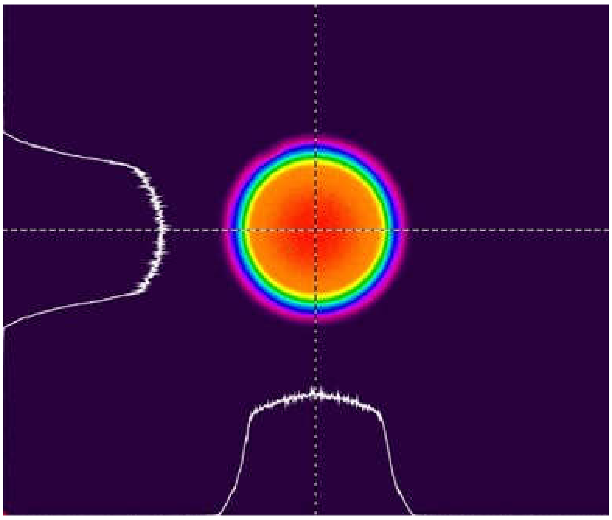

Fig. 2.14 Pump beam profile at focus (crystal plane) under operating conditions in Table 2.2. The above-90% top-hat beam diameter is 1.482 mm and 1.486 mm in x and y, respectively, or 1.283 mm and 1.287 mm 1/e^2 alternatively.

are shown in Fig. 2.15. From this analysis we expect a thermal lens with an effective focal length of $f_{th} = -3.4$ m.

2.3.5 The Ring-cavity

Ring cavities are generally more complicated to align compared to linear ones but they have several inherent advantages over linear designs for applications in CPA lasers [44]. These are the most important aspects to consider when choosing a design:

1. **Cavity length:** for a stable resonator larger mode size leads to larger cavity length. Using a ring design for a long resonator is advantageous, as a ring cavity (with the same mode size as a linear one) can have a smaller length.

2. **ASE Contrast:** leakage through a switchout polarizer (e.g. Pockels cell) prior to the switchout pulse and amplified spontaneous emission (ASE) limit the intensity contrast of a regenerative amplifier. In the case of nearly gain-saturated operation, the intensity of the ASE is proportional to $1/L$, where L is the cavity length [45]. In two comparable linear and ring resonators with same curvature mirrors and beam mode sizes, L will generally be shorter in a linear cavity (note L is the cavity length and not the roundrip length), and thus, ASE will be proportionally larger. Moreover, only ASE going in one direction matters in a ring cavity, while in a linear cavity it is coupled from both directions, which adds another factor of 2.

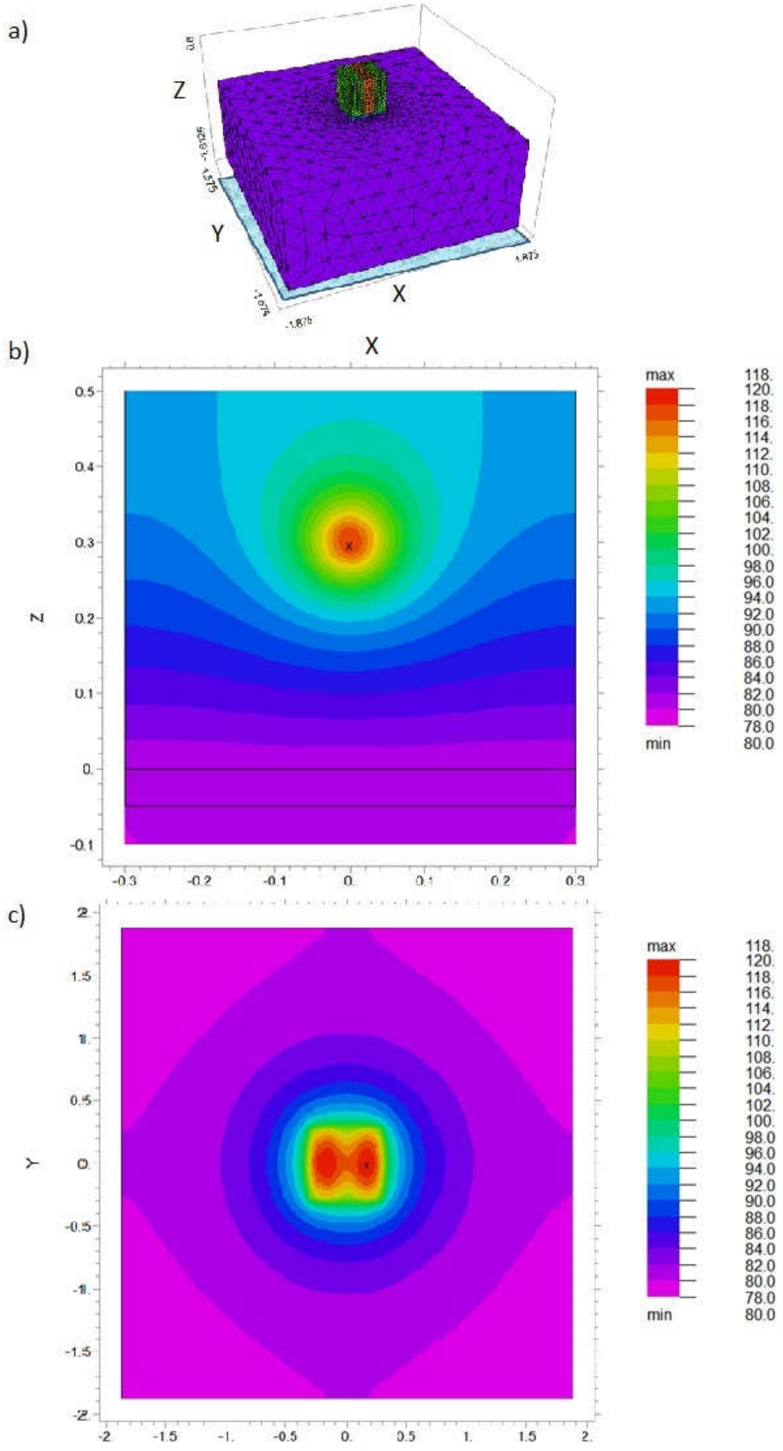

Fig. 2.15 a) Structure of the model representing the composite Yb:YLF gain crystal In-bonded to a cryogenically-cooled copper sink and b) side- and c) top-view of the corresponding temperature distribution under pumping conditions described above.

3. **Isolation from oscillator:** Typically, no more than pJ levels of the backrefleted energy can be tolerated. A ring and a linear cavity differ dramatically in the amount of energy they send back to the oscillator. In a linear cavity one or two stages of isolation are generally required (Faraday isolator or Pockels cell) to supress backreflections. In a ring cavity, only ASE is backreflected towards the oscillator due to its geometry, and thus either no stage or only one single stage suffice the isolation requirements.

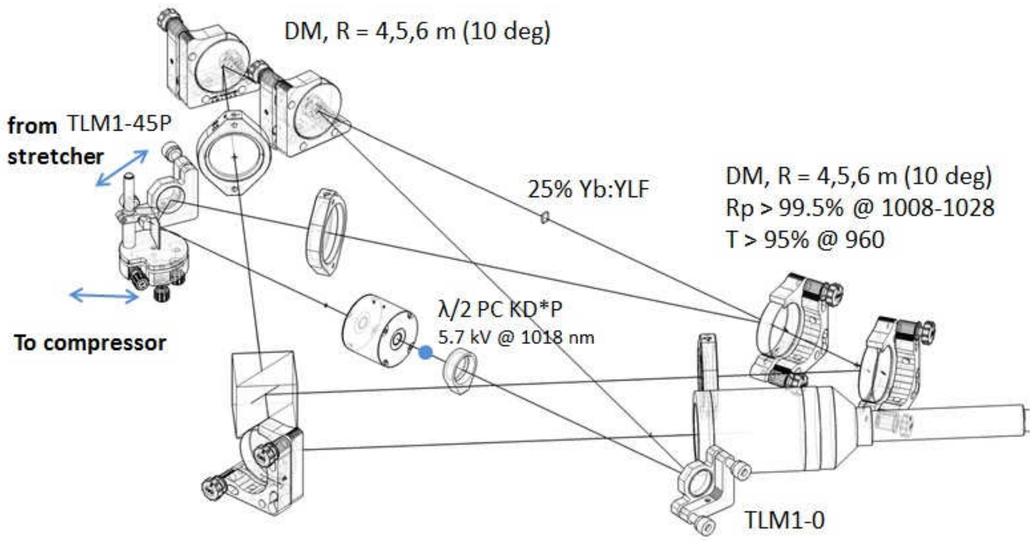

Fig. 2.16 Schematic of the ring-cavity for the seeded Yb:YLF regenerative amplifier, including pump-beam optics.

Our design is depicted in Fig. 2.16, which includes the pump-beam optics for completeness. The roundtrip length of the cavity is 2315 mm (7.716 ns). The stretched seed enters the cavity from a thin-film polarizer (middle-left) with horizontal polarization. A $\lambda/2$ electro-optic switch (Pockels cell) rotates the polarization of seed to vertical in order to trap the beam in the cavity for amplification. A local waist of about 0.75 mm is created by two curved dichroic mirrors on each side of the gain medium at 10 degree incidence angles. The amplified pulse exits the cavity after several passes by switching the Pockels cell again. All cavity mirrors are dielectric for higher damage thresholds. The Pockels cell is built out of two KD*P crystals (Fastpulse Technology model 1042), with a transmission exceeding 95% and a half-way retardation voltage in the order of a few kV. It has a clear aperture of 10 mm and a relatively fast rise time of about 450 ps. More details of the Pockels cell can be found in Appendix B.

Cavity Caustic and Stability

The cavity is designed to have an odd number of bounces so that after each pass the beam becomes its mirror image, that is, it is flipped with respect to the vertical axis. Such mechanism helps reduce spatial beam-distortions arising from one-directional index of refraction gradients present in the cryogenically-cooled crystal (recall Fig. 2.15.b).

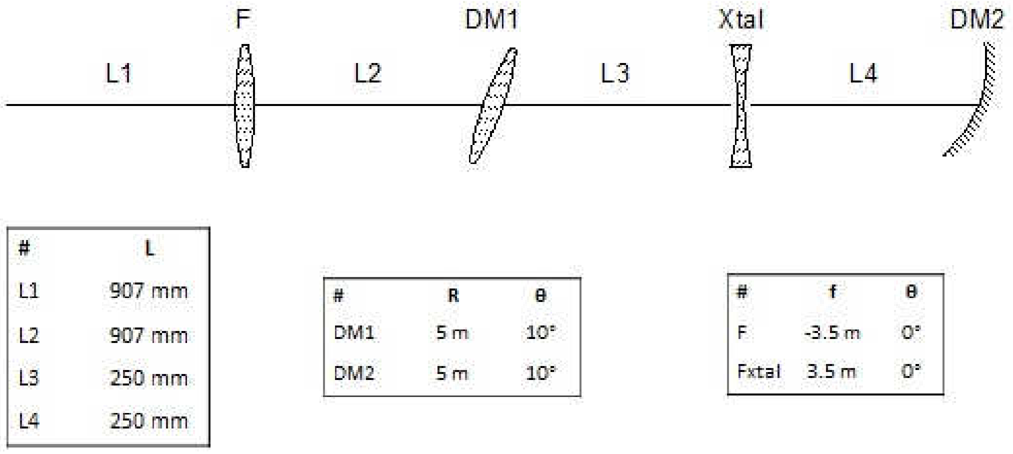

#	L
L1	907 mm
L2	907 mm
L3	250 mm
L4	250 mm

#	R	θ
DM1	5 m	10°
DM2	5 m	10°

#	f	θ
F	-3.5 m	0°
Fxtal	3.5 m	0°

Fig. 2.17 Schematic and relevant parameters of ring cavity.

A simplified version of the ring cavity with the corresponding relevant beam-propagation parameters is shown in Fig. 2.17. The dichroic mirrors (DM1 and DM2) have a radius of 5 m and an incidence angle of 10 degrees. An intermediate lens (F) compensates for the thermal lensing induced by the pumped gain element (F_{xtal}). The relative distances are embedded in the image.

Fig. 2.18.a shows the variation of the caustic along the roundtrip path, where the waist is kept within 0.72 to 0.76 mm size. We also calculate (Fig. 2.18.b) that for weak thermal lensing effects from the gain medium, in the order of a few hundreds of mm and beyond, the cavity is stable and that it can always be set to highly-stable with proper cavity lens (F) adjustments.

Seeded Amplification

The expected energy gain curve of this configuration is shown in Fig. 2.19. This estimate is calculated using Frantz-Nodvik equations.

The saturation fluence for our cryogenic 25%Yb:YLF is J_{sat} = 27.9 J/cm^2. After N=22 passes, the expected output energy and fluences are of the order of 8 mJ and 0.5 mJ/cm^2.

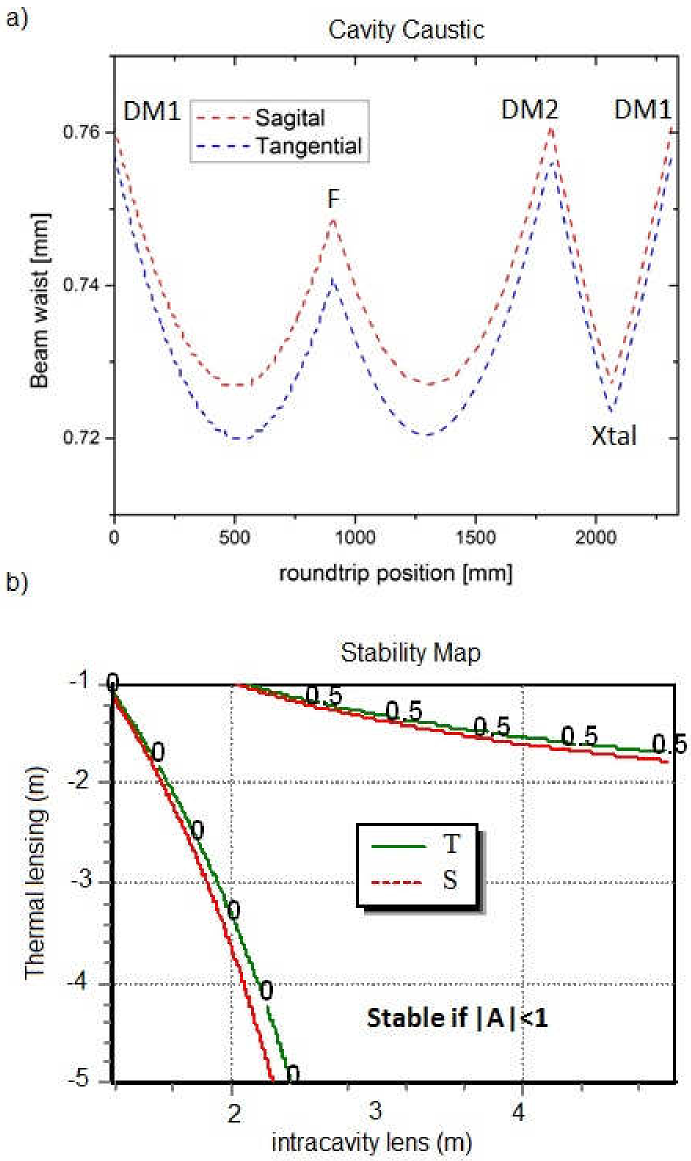

Fig. 2.18 a) Caustic of a stable single-mode 1018 nm wavelength pulse inside the ring-cavity and b) corresponding stability map as a function of thermal lensing strength.

Under the conditions listed on Table 2.3, the achieved population inversion is $\Delta N = 8.9 \cdot 10^{19}$ cm^2 and the unsaturated gain is $G_0 = e^{\Delta N \cdot \sigma} = 1.865$, or equivalently of $g_0 = 3.56$ cm^{-1}, where $\sigma = 0.7 \cdot 10^{-20}$ cm^2. In non-saturation operation, the extraction efficiency is low, of the order of 2 to 3%. This is a design specification and there is in principle no limiting factor other than damage threshold in scaling it. We also estimate the total accumulated B-integral after 22 passes to be 0.118 radians (assuming a nonlinear index $n_2 = 1.3 \cdot 10^{-16}$ cm^2/W, see Fig. B.5), which is still within acceptable values for post-amplification pulse compression.

Table 2.3 Design parameters for Frantz-Nodvik calculations

Seed energy	30 nJ
Seed duration	250 ps
Gain length	1.75 mm
Roundtrip losses	5%
Pump power	250 W
Pump pulse duration	2 ms
Pump waist	0.75 mm

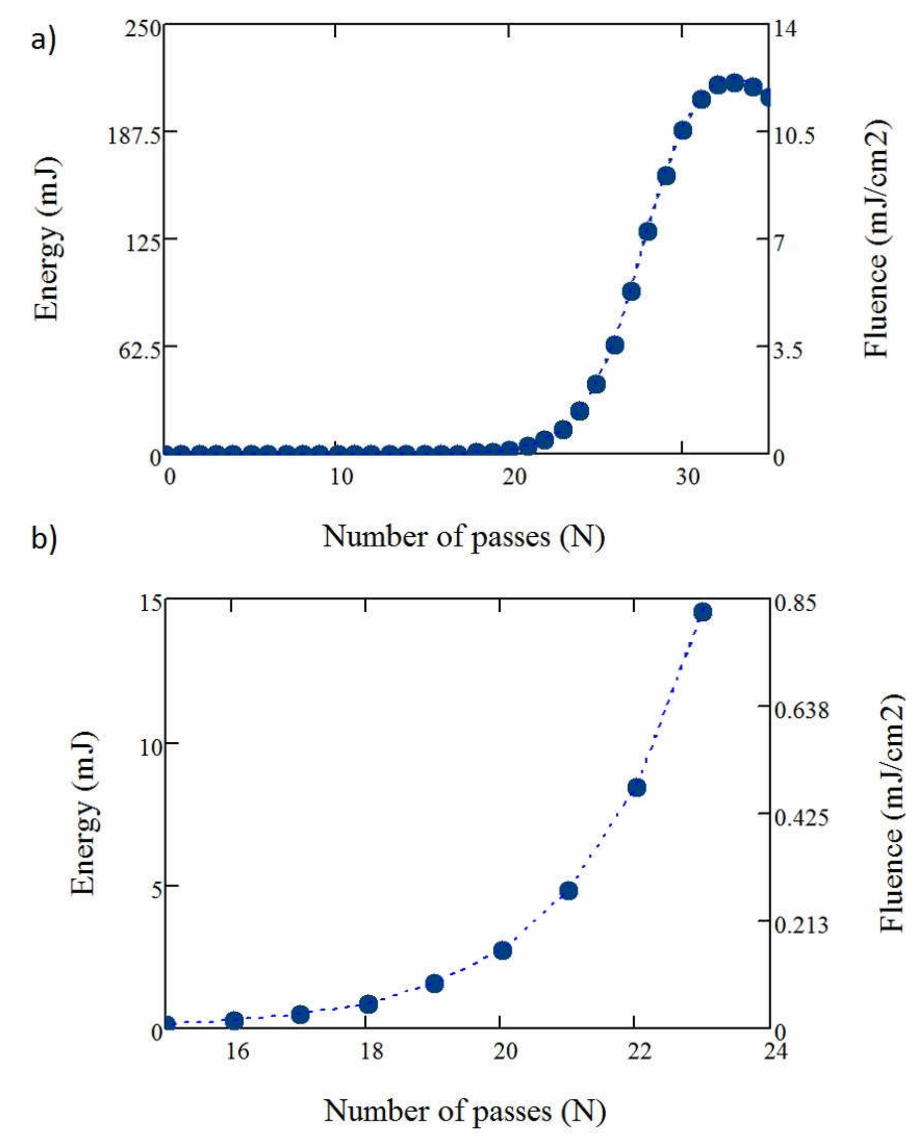

Fig. 2.19 a) Intracavity energy and fluence buildup as a function of number of passes in the cavity for the parameters in Table 2.3 and b) zoom of a) in the expected operational region.

Table 2.4 Grating compressor parameters

Grating line density	1752 lines/mm
Incidence angle	71.3 degrees (8-deg from Littrow)
Diffraction angle	57.1 degrees
Grating-grating distance (Z)	890 mm
GDD (2nd order dispersion)	$-3.1 \cdot 10^7$ fs^2
TOD (3rd order dispersion)	$3 \cdot 10^8$ fs^3
FOD (4th order dispersion)	$-4.8 \cdot 10^9$ fs^4
Compressed duration	600 fs (assuming a 4 nm bandwidth)

From the curves in Fig. 2.19, operation above 10 mJ amplified energy is achieved around pass 23 and beyond, with a very steep exponential increase of the fluence. Let us remind ourselves that the saturation fluence of well above damage threshold. We will address the practical implications of such dramatic energy increase in Subsection 2.3.7

2.3.6 The Grating-pair Compressor

It consists of two dielectric gratings with line density of 1752 mm^{-1}, in a double-pass grating pair configuration, as shown in Fig. 2.20. The fundamental design parameters of this compressor (listed in Table 2.4) were chosen to cancel out second and third order dispersion (GDD and TOD) from the grating stretcher and exhibits small residual FOD. The dielectric gratings are suitable for high-energy pulse compression because they exhibit damage thresholds in excess of 20 J/cm^2 for ns-pulses and 2 J/cm^2 for fs-pulses.

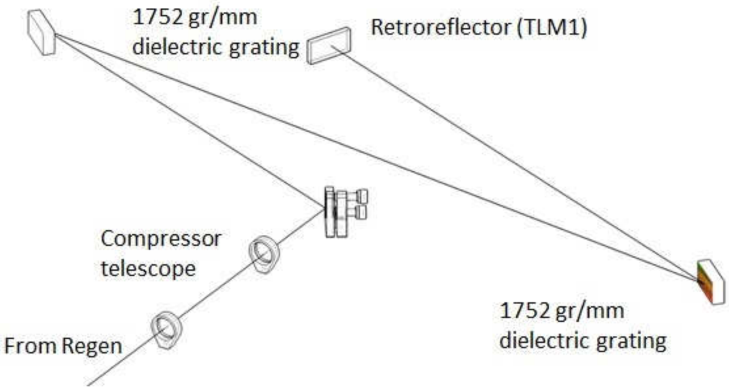

Fig. 2.20 Schematic of double-pass grating pair high-energy pulse compressor.

2.3.7 Intracavity Pulse-energy Buildup Control Electronics

The particularly high saturation fluence of Yb:YLF forces the system to work in a non-saturated mode, that is, the energy in the cavity grows exponentially pass after pass. This mode of operation is prone to high instabilities and fluctuations in extracted beam energy. Moreover, the intracavity pulse energy can easily grow above the damage threshold of various components, including the gain crystal itself or the Pockels cell. As a result, it is crucial that the laser system is actively controled and the maximum allowed amount of intracavity energy is monitored timely before irreversible damage occurs.

The dominant source of extracted energy instability is fluctuations in pump power throughout regenerative amplification, that is, for a few to several ns. Of course variations in the seed energy also affect the amplification curve, but to a much lesser extent. Fig. 2.21 illustrates the change of energy buildup slope in linear scale for a 2.5% increase in the pump power in our designed scheme. For example, the extracted fluence doubles by pass 40.

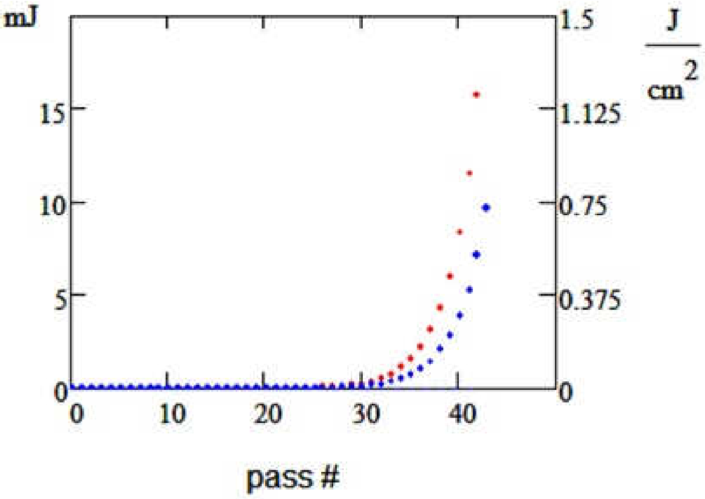

Fig. 2.21 Influence of 2.5% pump-power variation in amplified energy build-up.

The strong effect of pump-power variation lies in that the pulse energy grows proportionally in the exponent, as we show in the following equations. The extrated energy due to a normalized variation (α) in the pump power after one pass (E_1') is related to the input energy (E_0) and the small signal gain (G_0) by

$$E_1'/E_0 = G_0^{1+\alpha} = G_0^1 \cdot G_0^\alpha \tag{2.1}$$

Table 2.5 Maximum nominal fluence on cavity optical elements

Element	**Maximum nominal fluence** [J/cm^2]	**Surface damage threshold fluence** [J/cm^2] @1030nm 250ps
Yb:YLF composite crystal	0.56	>5
Dichroic mirrors	0.5	5
Dielectric flat mirrors	0.5	10
Uncoated fused silica lenses	0.55	25
AR-coated fused silica lenses	0.55	5
KD*P Pockels Cell	0.6	5

and after N passes,

$$E'_N/E_0 = G_0^{(1+\alpha)\cdot N} = G_0^N \cdot G_0^{\alpha\cdot N} \tag{2.2}$$

which results in ratio between the expected extracted energy in pass N under fully stable operation (E_N) and E'_N defined as

$$E'_N/E_N = G_0^{\alpha\cdot N} \tag{2.3}$$

The main implication of Eq. 2.3 is that the output energy of the system will depend on damage threshold of coating and optical materials. Table 2.5 lists the maximum nominal fluences each optical element will experience by design and what the corresponding surface damage threshold fluences are. Note that the cavity is conservatively designed to operate an order of magnitude below these thresholds, although the possibility of experiencing instabilities leading to an approximately twofold increase in intracavity fluence calls for intracavity pulse energy control.

We design a primitive active control loop (Fig. 2.22) that will release an amplified pulse out of the cavity if its energy exceeds the expected level above an arbitrary threshold value. It starts off by multiplying the time signal from the master oscillator and an external signal generator in a single-quadrant analog multiplier in order to set the gating frequency (repetion rate) of the Pockels Cell, in our case set at a 100 Hz. This signal is also used to trigger the laser diode (LD) pump at the same repetition rate and a pulse width set by a pulse generator of the order of 2 ms (upper level lifetime of the Yb^{+3} ions). The same signal is used to synchronously trigger the high-voltage (HV) pulse generator that switches the PC gating on (to a total 0-phase retardation in one cavity roundtrip). The pulse is trapped within the cavity while the gate voltage is set to $\lambda/2$ retardation voltage. Now that the LDM is operating at quasi-CW pumping mode and that the seed is trapped in the cavity, a fast photodiode (FPD) monitors the intracavity pulse energy buildup. The FPD signal enters an

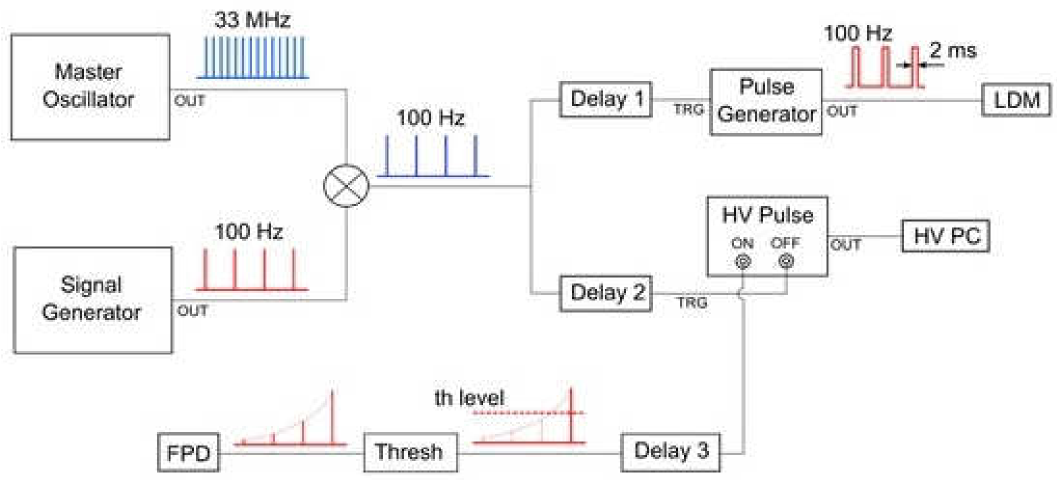
33 MHz
Master Oscillator
OUT
100 Hz
Signal Generator
OUT
100 Hz
Delay 1
TRG
Pulse Generator
OUT
100 Hz
2 ms
LDM
HV Pulse
ON
OFF
OUT
HV PC
Delay 2
TRG
th level
FPD
Thresh
Delay 3

Fig. 2.22 Conceptual schematic of 100 Hz trigger signal electronics and an integrated real-time intracavity energy buildup monitoring and control system.

analogue small signal amplifier and an analogue threshold (based on a fast time-discretizer and single-channel analyzer) that will trigger the gate on (to a total $\lambda/2$-phase retardation in one cavity roundtrip) and allow the amplified pulse to exit the cavity.

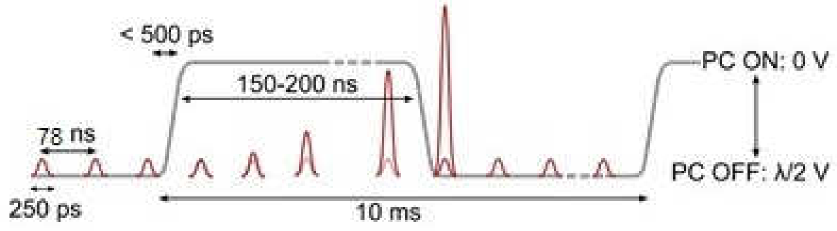
< 500 ps
150-200 ns
PC ON: 0 V
78 ns
PC OFF: λ/2 V
250 ps
10 ms

Fig. 2.23 Concept of seeding and Pockels cell triggering timing with most relevant time-scales.

The most critical aspect in the design of the active control loop is the time that takes the trigger signal from the threshold trigger to reach the HV pulse generator and for the electro-optic gate to switch to full voltage (calibrated values of voltage can be found in Appendix B, Fig. B.1). Fig. 2.23 shows the corresponding timing of the seed pulses, with respect to the gating time in the specific case of 100 Hz repetition rate. The gating time is expected to be in the order of 200 ns, corresponding to approximately 25 passes. The trigger signal must have a rise time of 1-5 ns, a peak amplitude of 2-5 V, a pulse width above 5 ns but no longer than 1 μs. Only the leading edge of the trigger signal is used for the ON/OFF switches (shown in Fig. 2.24) and must be 50 ohm terminated. The gating circuitry in Fig. 2.24 has an intrinsic delay of 50 ns. The analogue amplifier and single-channel analyzer also have an

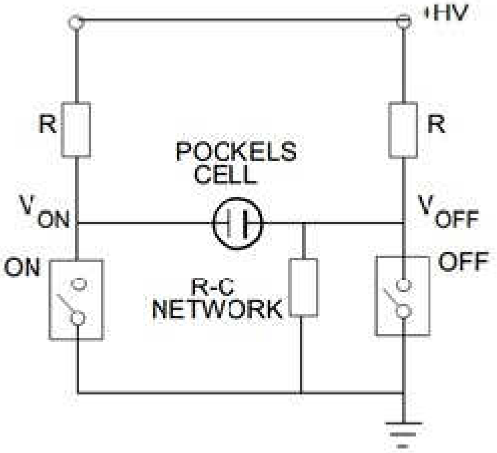

Fig. 2.24 Pocket cell HV trigger R-C network.

intrinsic delay of 20 ns. As a result, the intracavity pulse exceeding the threshold value must be detected at least 10 passes before extraction. In other words, this simple safety trigger mechanism works as long as the threshold value (which depends on the specific operation conditions of the laser) is set to an intracavity energy signal significantly smaller than the one corresponding to the maximum allowed intracavity energy.

Complementary passive control methods to avoid damage inside the cavity include the use of reversible saturable absorbers (RSA) and low-damage threshold inexpensive optical elements. These will be considered in future development.

2.4 Preliminary Lasing Results

We are able to retrieve the fluorescence spectrum of the custom-cut 25%-doped Yb:YLF and confirm strong suppression of the 995 line and operate afterward the cavity in quasi-CW multi- and single-mode. The results are summarized in the upcoming subsections.

2.4.1 Emission Fluorescence Spectrum

We measure the luminescence of our gain medium at cryogenic-temperatures excited by the LD pump at around 960 nm wavelength. The pump photons are very efficiently absorbed in 25%-doped Yb:YLF and thus the Yb-ions are turned into an excited state, from where they decay into lower- through spontaneous emission of photons. Such emission is the fluorescence. The emission fluorescence spectrum differs strongly from the pump spectrum (Stokes shift) since the excited Yb-ions may undergo non-radiative or optical transitions

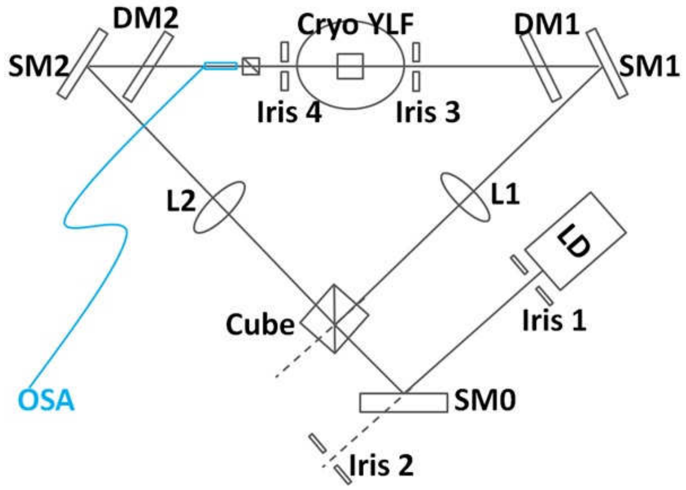

Fig. 2.25 Measurement setup for polarization-dependent emission fluorescence from both sides of the gain medium under different pumping modes.

to another excited level (lower or higher) other than its ground-state or may even cascade towards lower energy levels.

The setup employed for this measurement is depicted in Fig. 2.25. The gain medium is pumped from both sides and with two different polarizations, s- or vertical-polarization and p- or horizontal-polarization. The emission spectrum is also measured for both polarizations in an optical spectrum analyzer (OSA) at each end facet of the crystal. The fluorescence spectra at around 1018 nm wavelength are shown in Fig. 2.26 and confirm a bandwidth around 1018 nm of 7.5 nm. The fluorescence is randomly polarized.

We also confirm that fluorescence in the 995 nm line is strongly suppressed with respect to the 1018 nm line (as shown in Fig. 2.27).

2.4.2 Quasi-CW Operation

In order to optimize the efficiency of the ring cavity in quasi-CW (QCW) lasing operation mode, we take measure a series four of above-lasing-threshold output power values as a function of output coupling (or alternatively, as a function of internal optical losses). We fit our points using the Findlay-Clay analysis [45, 46] and find that an optical coupler with 0.18 transmittance yields maximum output power, as shown in Fig. 2.28.

Lasing of the ring cavity in QCW operation using a T=0.18 output coupler was achieved at 100 Hz repetition rate and a pump duty-cycle of 20%. The slope efficiency for single-mode operation is 45.5% (Fig. 2.29) with an excellent output beam quality (Fig. 2.30). In order to avoid high thermal load into the gain crystal, the cavity was conservatively operated

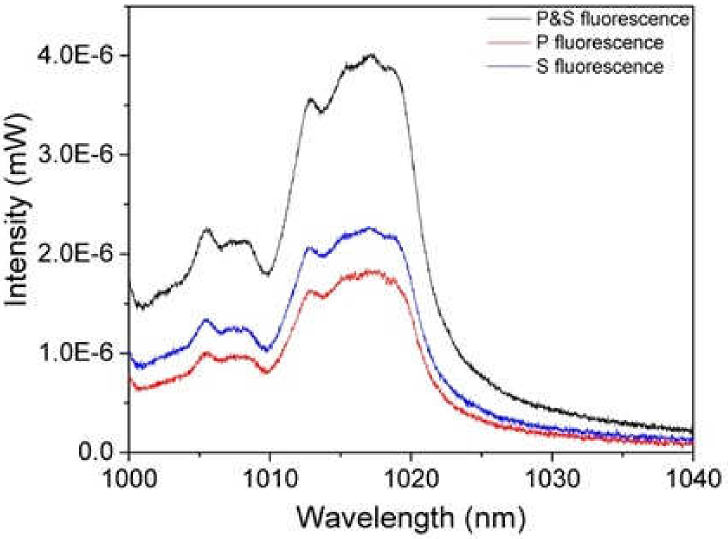

Fig. 2.26 Absolute measured fluorescence power spectrum of our custom-cut Yb:YLF crystal at cryogenic temperatures, pumped by our LD module at 960 nm wavelength. The OSA resolution is 0.1 nm over a 40 nm span.

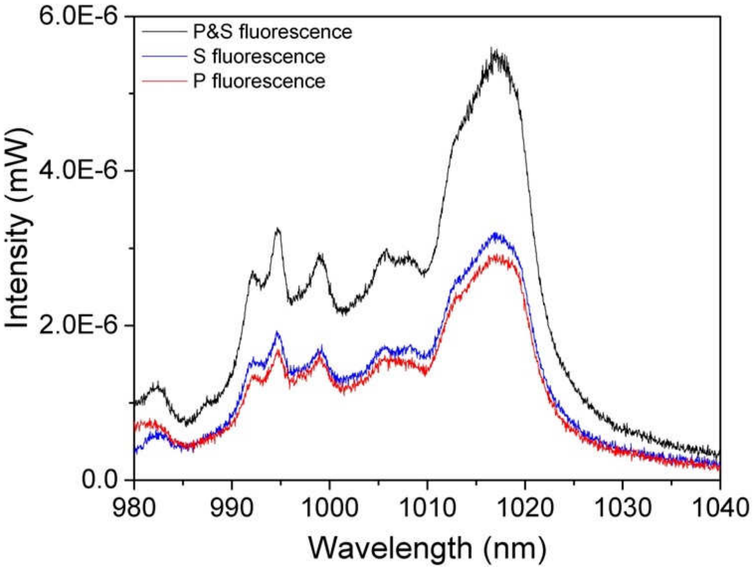

Fig. 2.27 Extended span of measured fluorescence power spectrum pumped under same conditions as in Fig. 2.26. The 995 line is strongly suppressed. The OSA resolution is 0.2 nm over a 60 nm span.

at a maximum average output power of about 19.5 W with 43 W of absorbed power from the LDM.

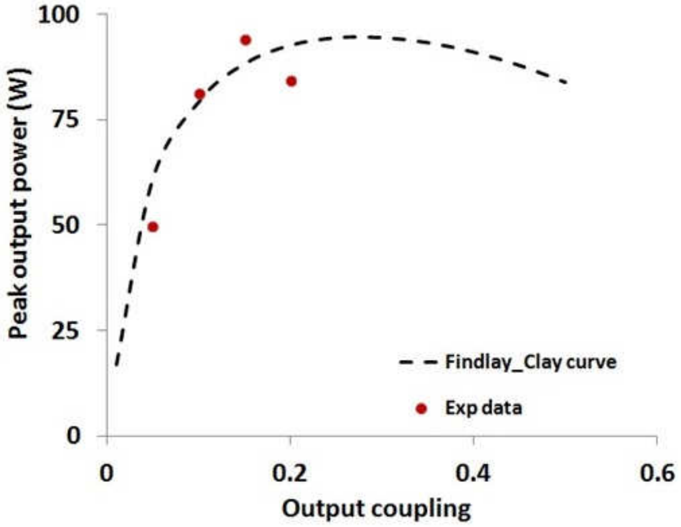

Fig. 2.28 Peak output power of QCW multimode ring cavity as a function of output coupler transmittance (T=0.05;0.1;0.18;0.2) and corresponding Findlay-Clay fit.

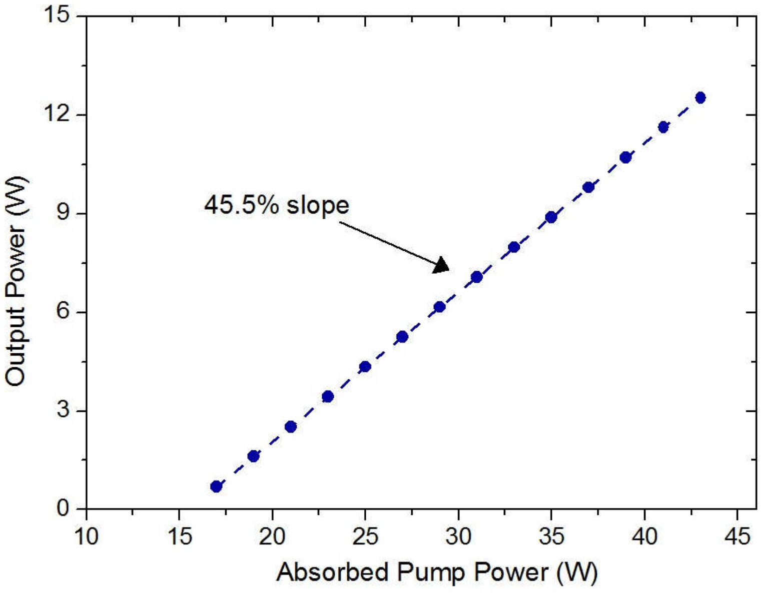

Fig. 2.29 Slope efficiency of QCW operated ring-cavity with an output coupling T=0.18.

2.5 Future Development and Prospective Use

In this chapter, a diode-pumped cryogenically-cooled Yb:YLF amplifier has been demonstrated with 40% slope efficiency, 43 W power, and excellent beam quality at QCW operation. The improved laser gain at low temperatures and low cavity loss will soon allow efficient regenerative amplification and scaling of femtosecond sources. Adapting this tech-

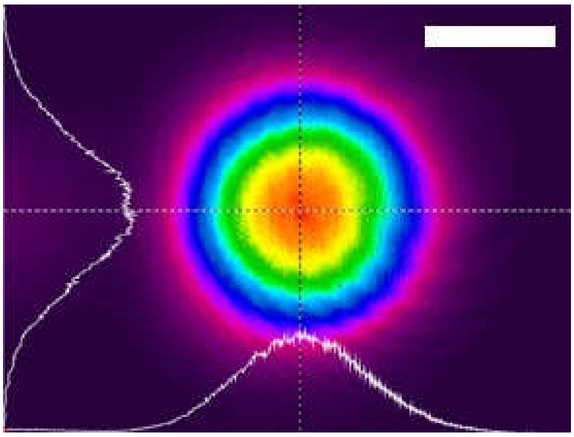

Fig. 2.30 Far-field image of the beam outputting the ring cavity in single-mode QCW operation (bar is 1 mm).

nology to thin-disk laser crystal will also enable to kilohertz operation and scaling to high average power.

In the short and mid-term, the system will be demonstrated to operate in Q-switch mode for high-energy ns-duration pulsed operation first and then be seeded for regenerative amplification. This operating regime will be ideal as a front-end for a multi-pass Yb:YLF amplifier system, which is currently under development, with a gain factor of ten in order to boost the energy and power of the regenerative CPA system while maintaining its bandwidth for sub-ps pulse durations. The performance of this system is expected to be above-100 mJ operation at 1 kHz repetition rate and 700 fs pulse duration. In the next chapter, we describe a frequency down-coversion process to efficiently generate THz radiation and expound on the reasons for high-power Yb:YLF technology to be the ideal driver for THz generation above the mJ-level.

Chapter 3

Power-scaling of Sub-cycle Terahertz Pulses

3.1 Introduction

The goal of this chapter is to present with experimental detail the power scaling mechanisms of terahertz (THz) generation via optical rectification from optical lasers. Step by step, we will point towards the ideal conditions for maximum conversion efficiency —including the pump laser, methods, and materials —, compare them to expected theoretical performances, and ultimately find its limitations.

3.2 Motivation

High-power and high-energy THz radiation is of significant interest to many applications such as non-linear spectroscopy [47], charged particle acceleration [48, 49], high harmonic generation [50], and molecular alignment [51], among others. As a consequence, there is a great need for the development of robust and efficient strong-field THz sources.

The sources capable of accessing the strong-field regime are predominantly accelerator-based facilities delivering up to 100 μJ THz energy [52, 53], or ultrafast laser-based tabletop systems [54–57]. Laboratory scale systems are of particular interest due to accessibility and relatively low cost. In this category, laser-induced air/gas plasmas [58] (delivering up to 5 μJ THz energy), collinear difference-frequency generation (DFG) in organic crystals [59, 60], and optical rectification (OR) (record energy of 400 μJ [55]) of optical pulses in nonlinear crystals have emerged as the most commonly employed methods of all THz generation modalities. The highest optical-to-THz conversion efficiencies in excess of 1%

at room temperature have been achieved by OR employing angularly dispersed femtosecond IR pump pulses in lithium niobate [61]. As a result, these systems are specially relevant to generating millijoule-level THz pulses.

Since most high-power THz generation schemes depend on some type of nonlinear frequency conversion process from an optical laser, scaling of THz energy means scaling of optical lasers. Obviously, as energy conversion efficiency decreases the demand for high-power optical lasers increases, and there are practical limitations to that too. Extracting the maximum possible energy from the frequency conversion system is thus crucial for the purposes stated in this thesis.

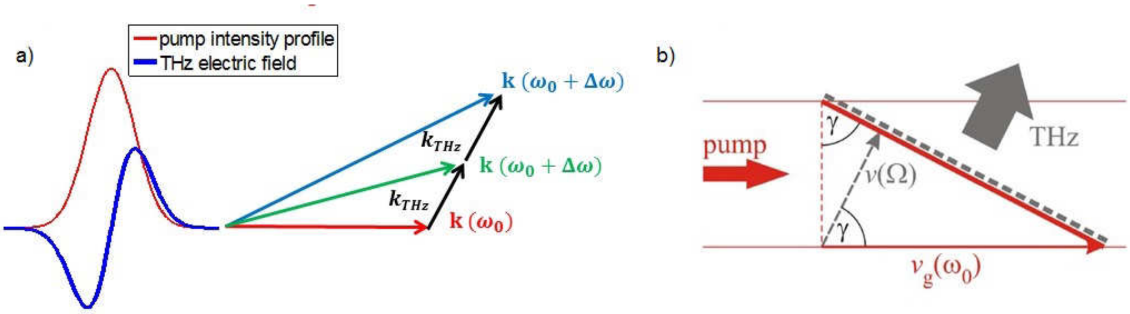

Fig. 3.1 a) Conceptual k-vector distribution in non-collinear DFG process and b) conceptual schematic of PFT OR.

THz generation via OR using pulse-front tilts (PFT) has shown to be one promising technique both for its high efficiency and power scaling capabilities, which we will study in detail in the upcoming section. Intense THz pulses can be generated via OR from ultrashort laser pulses in media with high optical second order nonlinearity, typically lithium niobate. These can only be effectively excited when the group velocity of the pump pulses in the medium matches the phonon-polariton phase velocity. One possible approach to meet this condition is to tilt the pulse intensity front of the pump so that the projection of its velocity in the propagating direction equals the velocity of the THz radiation [62]. However, while theoretical predictions point at a few percent of optical-to-THz conversion efficiency [63], most experimental results do not exceed a fraction of a percent in efficiency. In this chapter, we report on a parametric study of the central wavelength and pulse duration of the pump laser to experimentally explore the optimal operating conditions for maximum conversion efficiency. We also identify the major limiting agents for upscaling optical rectification (OR) processes using PFTs.

3.3 Non-collinear Intrapulse Difference-Frequency Generation

One available technique for THz generation is OR. In lithium niobate, the refractive index at THz and optical frequencies are about 5 and 2.2, respectively, and are thus highly mismatched. Consequently, phase-matching using collinear geometries in bulk lithium niobate is not efficient. In order to circumvent this problem, the intensity pulse front is tilted with an angle γ, which evens out the group velocity of the optical pulse (v_g) and the terahertz phase velocity (v_{THz}) in the nonlinear medium. The angular dispersion is introduced via a diffraction grating. In this intrapulse DFG process, we need to fulfill the phase-matching condition $k(\omega_0) - k(\omega_0 + \Omega) = k(\Omega)$ to generate a THz photon.

$$v_g \cos(\gamma) = v(\Omega) \tag{3.1}$$

The efficiency of this process can expressed under the plane-wave and undepleted pump approximation [64] as follows

$$\eta = \left(\frac{2d_{eff}^2}{\varepsilon_0 n_{opt}^2 n_{THz} c^3} \right) \Omega^2 I \left| L^2 \exp(-\alpha L/2) \frac{\sinh^2(\alpha L/4)}{(\alpha L/4)^2} \right| \tag{3.2}$$

where, d_{eff} is the effective nonlinear coefficient of the medium, ε_0 is the vacuum permittivity, n_{opt} and n_{THz} are the refractive indices of the optical and THz pulses inside the medium, respectively, c is the speed of light in vacuum, and α is the linear absorption coefficient of the THz pulse. To a first order, the efficiency scales quadratically assuming phase-matching with both the THz frequency Ω and the interaction length inside the nonlinear medium L, where only linear absorption is included. Material properties play an important scaling role too.

This approach holds promise in high-power THz generation for its relatively high efficiency and compatibility with strong pumps. However, there is a significant discrepancy between conversion efficiencies predicted by theory in other groups, of more than 10% at cryogenic temperatures with 1 μm wavelength pump [63] and experimental results in the order of a few percent at its record best under similar conditions [61, 65]. This strong disparity motivates re-examining existing models to identify potential shortcomings in theory and steer efforts towards more efficient THz generation schemes.

Before delving into case specific examples, let us note two general and very relevant inherent processes present in OR. On the one hand, the number of cascading cycles (N) —or the number of optical photons that are recycled after undergoing nonlinear frequency down-conversion (and the less probable up-conversion)—increases relative to the pump optical frequency (ω_{opt}) and assists greatly in boosting the photon-to-photon conversion process (Manley-Rowe limit), since as the pump spectrum shifts towards longer wavelengths (λ) it continues to transfer optical energy to THz frequencies (Ω) for as long as the phase mismatch is small [66]. The effect of cascading is conceptually depicted in Fig. 3.2. N is expressed as follows:

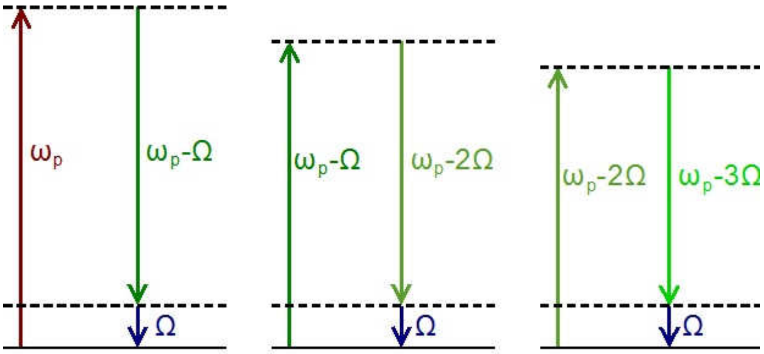

Fig. 3.2 Concept of optical cascaded frequency down-conversion.

$$N = \frac{1}{4\pi c L}\frac{\omega_{opt}^3}{\Omega^2}\left(\frac{d^2 n}{d\lambda^2}\right)^{-1} \tag{3.3}$$

On the other hand, when the pulse front tilt is introduced to achieve achromatic frequency conversion, angular dispersion typically dominates the group-velocity dispersion (GVD) term (typically abs(GVD$_{ang}$) >$1 \cdot 10^5$ fs^2/mm) against material dispersion (abs(GVD$_{mat}$) $\approx$ 250 fs^2/mm) as

$$GVD_{ang} \approx -\frac{n_{opt}}{\omega_0 c}(\tan\gamma)^2 \tag{3.4}$$

by up to two orders of magnitude, which limits the coherence length to several millimeters and thus affects the conversion efficiency, as we will show in the upcoming sections.

3.4 Optical Rectification in the 800-nm Pump Region

Our first wavelength region of interest is centered around 800 nm since Ti:Sapphire-based lasers today continue to be the dominant ultrafast high-energy and -average power laser technology present in most laboratories. We will study the main limitations and efficiency saturation mechanisms and we will see that most conclusions are qualitatively applicable to any optical wavelength, thereby making the PFT OR in the 800-nm pump region an

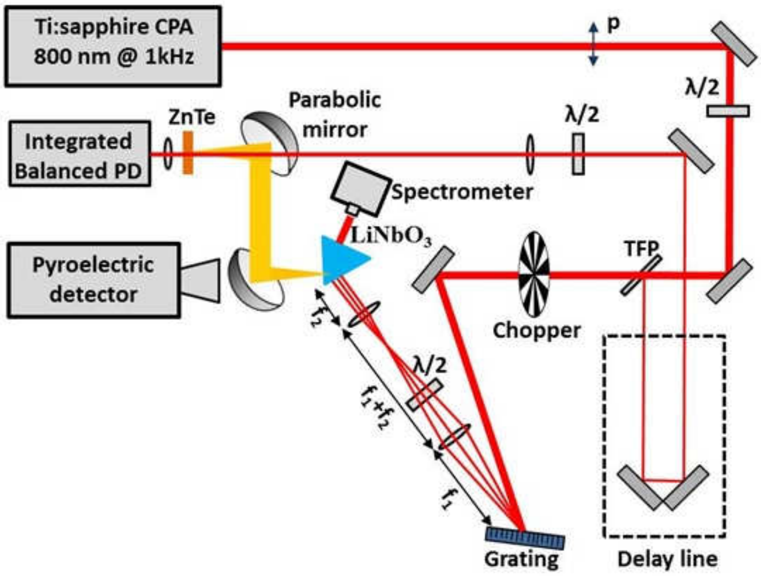
Ti:sapphire CPA
800 nm @ 1kHz
p
λ/2
Integrated Balanced PD
ZnTe
Parabolic mirror
λ/2
Spectrometer
LiNbO$_3$
Pyroelectric detector
TFP
Chopper
f_2
λ/2
f_1+f_2
f_1
Grating
Delay line

Fig. 3.3 Experimental layout of the THz generation by optical rectification in the 800-nm pump-wavelength region.

exemplary case of study.

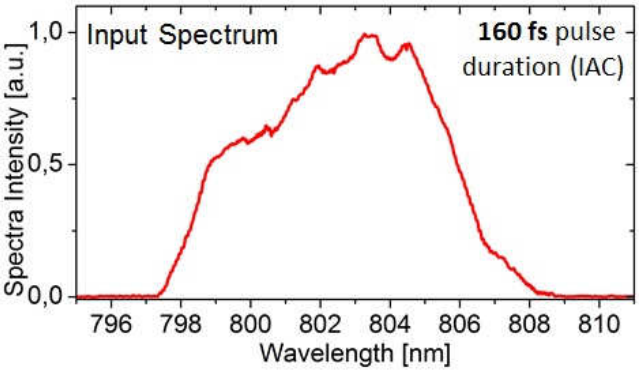

Fig. 3.4 Pump spectrum from Ti:Sapphire amplifier corresponding to a measured transform-limited pulse duration of 160 fs.

For these studies, we start off a multi-mJ Ti:Sapphire amplifier system centered at around 800 nm and with a bandwidth of 11 nm (Fig. 3.4). We have 6 mJ available for this experiment at 1kHz repetition rate. We are able to generate highly-efficient sub-cycle THz pulses via PFT OR in 6.0% MgO-doped congruent LiNbO3 (cLN) in a setup depicted in Fig. 3.3, which is standard for PFT THz generation. The intensity front of the pump pulses is tilted using a 1500 mm^{-1} diffraction grating at 35 degree incidence angle. The pump beam has a collimated FWHM diameter of 52 mm at the grating plane and is focused onto the cLN

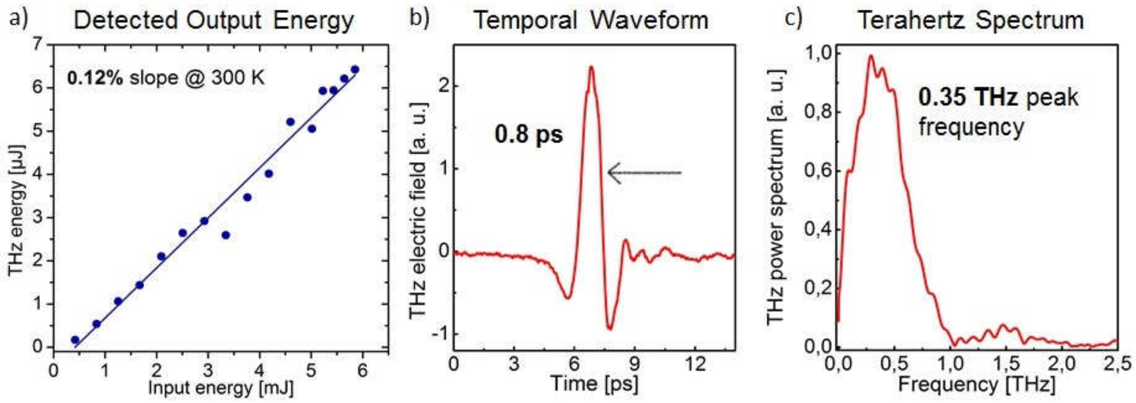

Fig. 3.5 a) Generated THz energy as a function of input optical energy at 300 K. b) Temporal waveform measured by EO sampling in 0.5 mm ZnTe. c) Retrieved broadband THz spectrum with maximum spectral content at 0.35 THz.

crystal (57.9(Y)x57.9x54.4 mm, height 25.4mm(Z), uncoated, apex angle: 63 degree) using a two achromatic spherical lens telescope with a magnification factor of -1/3. The pulse duration is measured with an interferometric autorrelator to ensure the pulse is near transform-limited at the center of the cLN crystal. A calibrated $LiTaO_3$-based pyroelectric detector (Microtech Instruments, Inc.) is used for the measurement of the THz energy. We simultaneously observe the red-shifted optical power spectrum at the output of the prims, which undergoes total-internal-reflection on the first interface cLN-to-air (the THz-outcoupling interface).

We also perform electro-optic (EO) sampling in a 0.5 mm thick ZnTe crystal that provides the temporal profile of the THz electric field and a retrieved energy spectrum.

Employing the full pump bandwidth we routinely obtain 6.5 μJ output energy and same amount of mW of average power, with an energy conversion efficiency slope of 0.12% at room temperature (Fig. 3.5.a). The measured THz field temporal waveform is in Fig. 3.5.b, with sub-cycle duration, and the corresponding THz spectrum amplitude with 0.35 THz peak wavelength (Fig. 3.5.c), both exemplary of standard optical rectification with ultrafast pulses.

Understanding these results as a whole can be complex. With these initial results in mind, we will now assess the role of different factors and address what the main efficiency scaling and saturation mechanisms are.

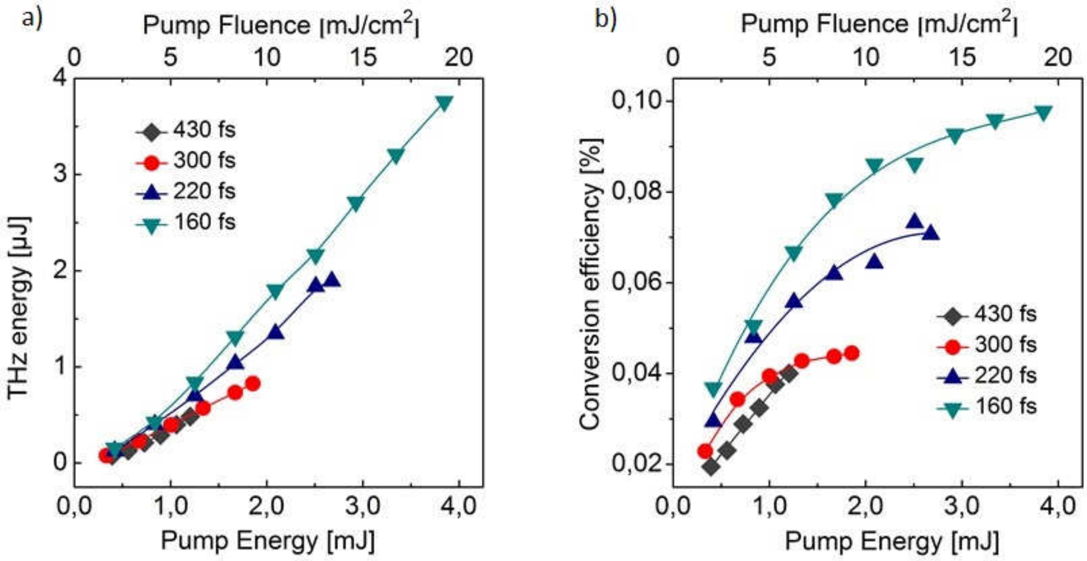

Fig. 3.6 a) THz energy as a function of input optical energy for a variety of transform-limited pulse durations and b) corresponding efficiency curves.

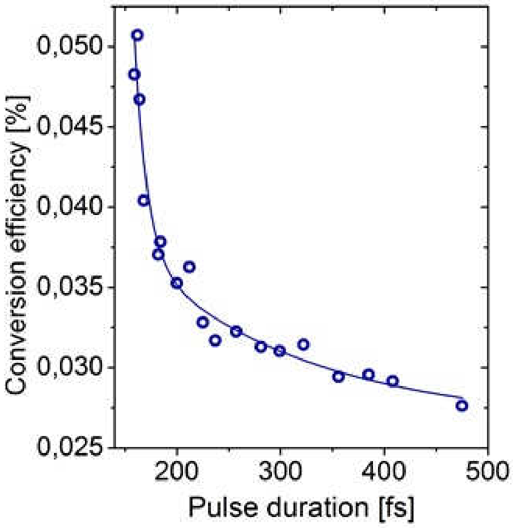

Fig. 3.7 Conversion efficiency as a function of peak intensity for fixed pump fluence and central wavelength.

3.4.1 Influence of Pump Pulse Duration

As we have mentioned in the previous section, the efficiency, to a first order approximation, scales quadratically with both the THz frequency and the interaction length. Now, in this approximation the efficiency also scales linearly with pump intensity. THz absorption in lithium niobate also imposes severe restrictions in energy extraction, which will be ad-

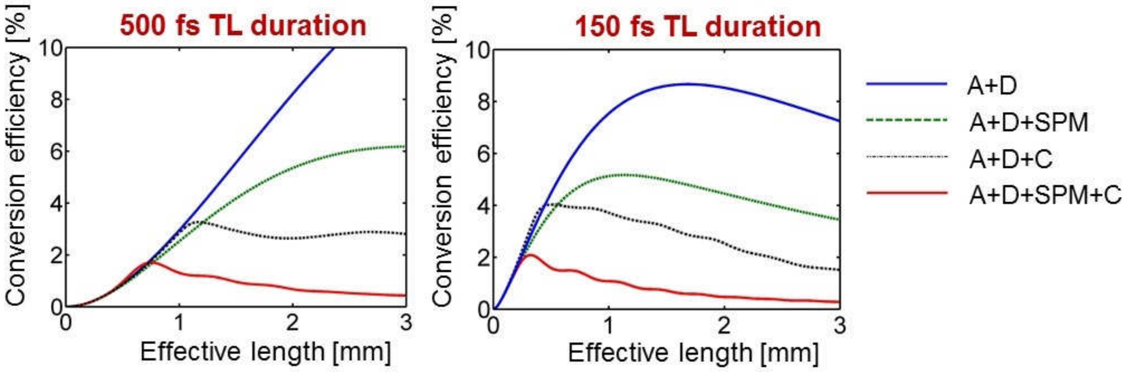

Fig. 3.8 One-dimensional model of saturation mechanisms for two different pulse durations, including material and angular dispersion (D), linear absorption (A), self-phase modulation (SPM) and cascading (C). The parameters used in this simulation are a fluence of 15 mJ/cm^2, a temperature of 100 K, a nonlinear refractive index $n_2 = 2 \cdot 10^{-15}$ cm^2/W and second order susceptibility $\chi^2 = 366$ pV/m from [3].

dressed in upcoming sections. For a start, we measure the influence of the pulse duration, or alternatively peak intensity, with transform-limited pulses all centered at a 803 nm wavelength, and show the THz output energy as a function of input energy and fluence for 430, 300, 220, and 160 fs pulse durations.

Fig. 3.6 shows an increased efficiency trend for shorter pulse durations, which is directly associated to an increase in peak intensity. This effect is more apparent in the conversion efficiency curve (Fig. 3.6.b). The saturation fluence shows up around 15 mJ/cm^2 for the 160 fs pump.

Additionally, we investigate the dependence of THz generation efficiency on pulse duration for various transform-limited pulse durations at a constant pump fluence of 6.5 mJ/cm^2 and central wavelength of 804 nm, as shown in Fig 3.7. The conversion efficiency decreased by 45% when the pump pulse duration was increased from 157 to 475 fs. We achieve a maximum THz energy of 6.4 μJ for the shortest transform-limited pump pulse energy available.

3.4.2 The Combined Effect of Angular Dispersion and Cascading

The efficiency increase with pump intensity shown in Fig. 3.7 is significant. However, the trend is not linear, as one would expect from the simplified analytical equation in Eq. 3.2. Moreover, Fig. 3.6 shows that the shortest pulse duration of 157 fs exhibits the highest saturation threshold of about 15 mJ/cm^2 while saturation is not reached for the 426 fs curve due to the limited pump energy. In earlier studies, both self-phase modulation (SPM) and free-carrier absorption (FCA) due to multi-photon absorption was cited as the principal reason for THz energy saturation in the 800 nm wavelength region, although no direct evidence has been reported.

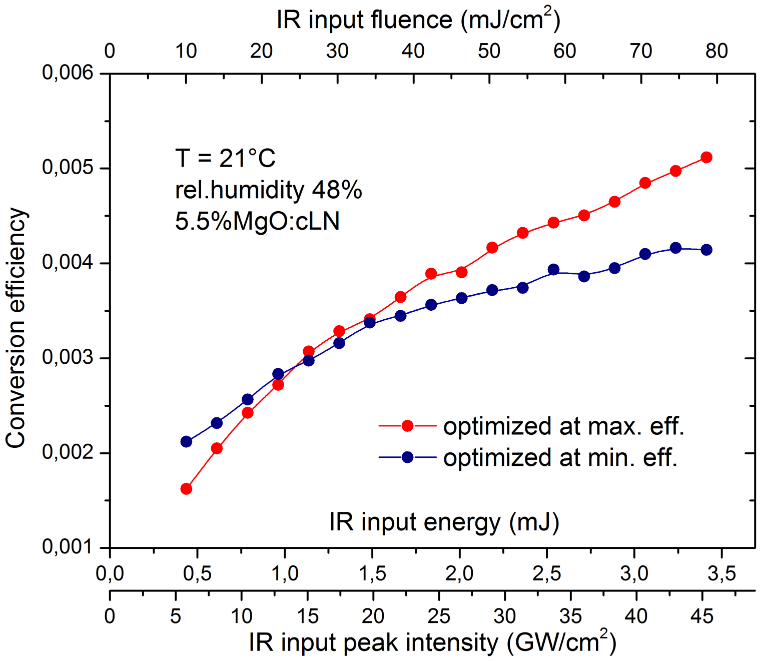

Fig. 3.9 Measured THz conversion efficiency curves as a function of input optical energy, fluence, and peak-intensity, acquired by starting off the optimum conversion at lowest input energy upward (blue); and starting off at highest input energy downward (red).

In order to begin to address in more detail the saturation mechanisms of PFT OR, we employ a more inclusive one-dimensional model that considers both material and angular dispersion (D), linear absorption (A), SPM, and cascading (C) [3]. We are able to compute the expected conversion efficiencies as a function of effective length. As an example, Fig. 3.8 shows the effect of including different major role players in PFT OR and the corresponding expected efficiencies. It is directly obvious that conversion efficiencies of a few percent may be possible only within few millimeters of propagation and that SPM shows to be more detrimental at stronger intensities.

Now, we observe a very pronounced efficiency decline when cascading is included. The effective interaction length, already short due to angular dispersion, decreases even faster because of cascaded broadening of the pump pulse. As a result, the efficiency does get higher for stronger pumping but the effective coherence lengths drastically decline to about one millimeter. Note that this applies only at cryogenic temperatures, at which —only for the purposes of this section of our study—we will neglect THz phonon absorption. Another important implication from Fig. 3.8 is that, each of these fluences exhibit a different optimal effective length. One has to keep this implication in mind when carrying out experimental parametric sweeps as simple as for instance, efficiency versus input energy, since that would determine the trend of the curve. This effect is exemplified in Fig. 3.9, where we acquired efficiency curves of a PFT OR setup with the same pumping conditions for two different starting points: one with the setup optimized at highest pumping intensities; the other with the setup optimized at lowest pumping intensity. The results, as well as the simulations, show that each complete set of conditions in a PFT OR process has an optimal operation point.

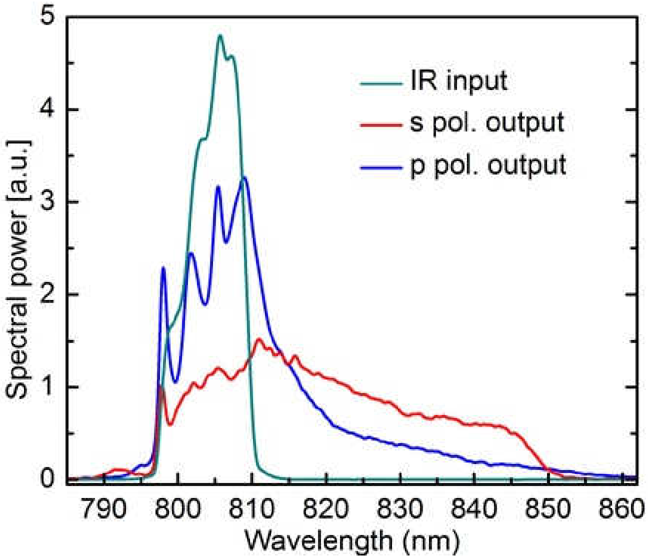

Fig. 3.10 Input and output optical power spectrum of the pump pulse for s- and p-polarization. The number of cascaded cycles of the broadened optical spectrum (red) is estimated to be about 14.

An alternative way of looking at the cascading effects is in the strong correlation between high THz efficiency and the output spectral broadening of the pump. In fact, we know now that the key element to limiting the conversion efficiency in PFT OR is the short coherence length associated with strong angular dispersion in conjunction with cascaded broadening. In order to verify it experimentally, we measure the spectral reshaping effects in the transmitted optical spectrum due to THz generation with and without phase matching by varying the input polarization. Fig. 3.10 shows the measured input spectrum in dark cyan and the broadened output spectrum after the highest THz conversion efficiency in red. The scale is absolute, and thus the entire initial power spectrum is being shifted towards redder wavelengths as they interact with each other during OR until, at some point, the broadening is so strong that phase-matching ceases to fulfill. If we simply rotate the input polarization 90 degrees, and record the output spectrum (in blue), the broadening diminishes dramatically, and so does the THz conversion efficiency, about a fourfold. From the recorded s-polarized broadened output spectrum, we estimate the number of photon cascading cycles (N) to be $N \approx 14$. Therefore, the *intrinsic*[1] THz conversion efficiency is expected to be about 1.3%, in agreement with predicted efficiency values. The detriment in detected efficiency is primarily linked to FCA in the material, Fresnel losses, and finite detection.

We confirm again that cascading plays a crucial role in upscaling the conversion efficiency as much as it does in limiting it, and that therefore, it cannot be omitted when computing the THz generation schemes.

3.4.3 Influence of Central Pump Wavelength

We fix the pump fluence and bandwidth to 5 mJ/cm^2 and 5 nm, respectively, and record the THz energy as a function of central wavelength in order to study its scaling law only in the vicinity of 800 nm. The THz energy monotonically increases with the central wavelength of the pump laser. In fact, we observe a dramatic increase in output energy even at moderate pump intensities, of up to 50% in just about 5 nm shift from 801 to 806 nm wavelength (Fig. 3.11).

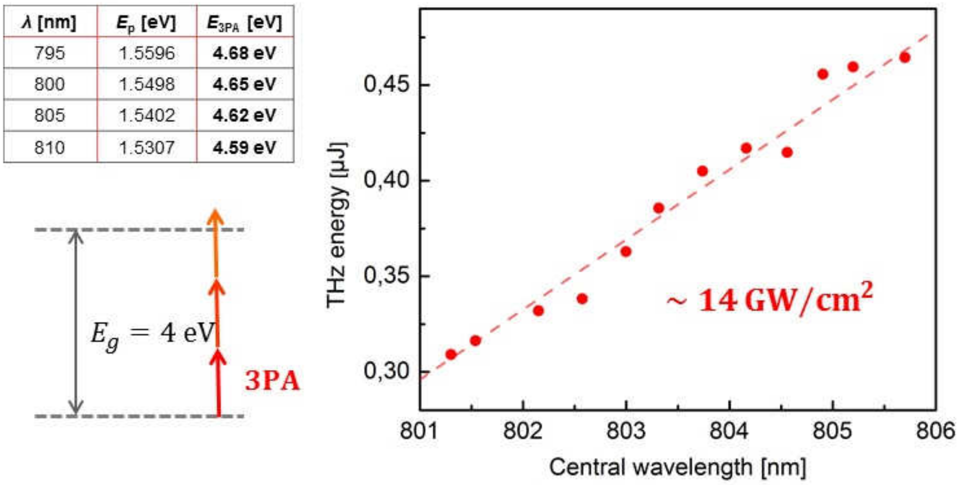

λ [nm]	E_p [eV]	E_{3PA} [eV]
795	1.5596	**4.68 eV**
800	1.5498	**4.65 eV**
805	1.5402	**4.62 eV**
810	1.5307	**4.59 eV**

Fig. 3.11 Generated THz energy as a function of pump central wavelength for fixed peak intensity, fluence, and bandwidth.

This observation indicates that the central wavelength of the pump has a strong influence on the THz generation, at least in this frequency range. We associate this behaviour to three-photon absorption (3PA), limiting the conversion efficiency by creating free carriers, which strongly absorb THz waves. In fact, the direct band gap (E_g) of lithium niobate is in the range of 4 eV at room temperature and a significant nonlinear absorption rate may originate from three-photon interband transitions, where the photon energy ($\hbar\omega$) is about 1.55 eV, even at moderate intensities of up to a few tens of GW/cm^2. For a given radiation intensity, the interband 3PA scales approximately linearly with photon energy in the case $3\hbar\omega > E_g$, which is the case for 3PA in lithium niobate with a radiation wavelength centered around 800 nm. This process limits the conversion efficiency by significantly increasing the free-carrier density, which then strongly absorbs THz radiation. These results still require further investigation but strongly motivate the inclusion of multi-photon and free-carrier absorption into our models, which may seemingly unfold strong wavelength correlation of THz efficiency around the 800 nm region and beyond. Moreover, crystal temperature dependence must also be considered for the purposes of FCA analysis since the band gap of lithium niobate decreases dramatically with increasing temperature [67].

---

[1] We denote *intrinsic* energy conversion efficiency hereafter as the one which occurs as direct DFG process inside the crystal, withouth considering absorption, outcoupling, and collection/transport losses, although it does consider back-conversion in the crystal.

3.4.4 Summary of Limiting Factors

In this section we have experimentally and theoretically investigated the most relevant scaling mechanisms of OR by PFT with unprecedented agreement. Understanding this complex process is an ongoing progress but there are some clear remarks from our observations. The first and most important being that:

1. Conversion efficiencies are overestimated if cascading effects are neglected in a general OR process.

2. Self-phase modulation weights in only at considerably high intensities and never exceeding the combined effect of

3. angular dispersion and cascading, which are the two main scaling limitations in PFT OR.

4. THz conversion efficiency exhibits a strong wavelength sensitivity in the 800 nm range possibly from strong FCA due to 3PA.

3.5 Enhanced Conversion Efficiency in the 1μm Pump Wavelength Region

In general, there are three main implications that need to be considered when employing longer wavelengths in PFT OR:

1. Given an arbitrary pump fluence, the use of longer pump wavelengths for THz generation ensures a latter saturation of the generation process due to multi-photon absorption. As a result, the pump peak intensity can be increased in the system in order to enhance the efficiency before FCA due to 4PA becomes a limiting factor.
2. The number of cascaded cycles decreases significantly given a propagation length by a factor of more than 2 from 800 nm to 1 μm pump, for instance. As a consequence, the optimum interaction length (L) may become longer since the spectral shape of the pump will distort at a slower rate due to cascaded spectral broadening. In other words, a new optimal balance for optimum pump and interaction length conditions may be found.
3. Material dispersion may be significantly smaller or negligible. This process may not be dominant but should not be neglected.

In this section, we present the main achievements and implications of analogous OR setup to that employed in Section 3.4 employing a pump laser at a central wavelength of 1030 nm.

3.5.1 Experimental Setup

The pump source is based on an in-house developed high-energy Yb:KYW dual-crystal regenerative amplifier [68]. The laser system delivers 4.3 mJ pulses at 1 kHz repetition rate compressed to 700 fs pulse duration (FWHM sech2 fit) at a central wavelength of 1030 nm, outputting average- and peak-powers well above 4 W and 6 GW, respectively. We employ the same lithium niobate crystal again and find an optimal setup, shown in Fig. 3.12, that can introduce a pulse front tilt of about $\gamma \approx 63^\circ$ with the main parameters listed in Table 3.1. The incidence and diffraction angles are chosen such that the angular dispersion of the beam is minimized while fulfilling the tilt angle imposed for phase-matching at THz frequencies.

One of the main differences introduced in the geometry of this setup with respect to the previous one is the imaging system after the grating, which, instead of consisting of a traditional Keplerian telescope, is made out of two cylindrical lenses. Employing such

Table 3.1 Design parameters of PFT OR setup at 1030 nm

Grating	1500 lines/mm
Incidence angle α	56.16 degrees
Diffraction angle ϕ	45.59 degrees
Magnification (M)	-0.5
Focusing Lens 1 (f1)	75 mm f (Tangential)
Focusing Lens 2 (f2)	50 mm f (Sagittal)
Distance to f1 (t1)	225 mm
Distance f1-to-f2 (u)	37 mm
Distance to crytal (s2)	75 mm

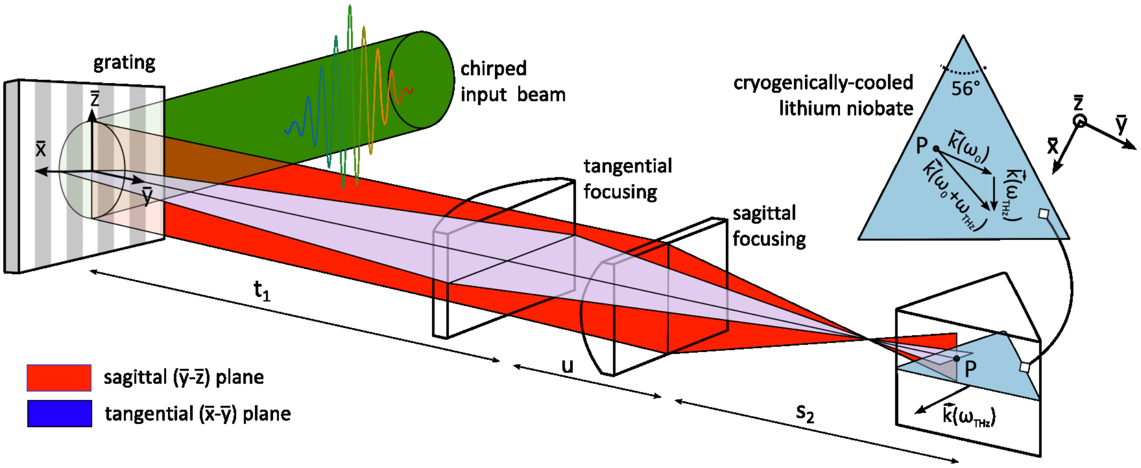
grating
$\bar{z}$
$\bar{x}$
$\bar{y}$
chirped input beam
tangential focusing
sagittal focusing
cryogenically-cooled lithium niobate
56°
P
$\vec{k}(\omega_0)$
$\vec{k}(\omega_0+\omega_{THz})$
$\vec{k}(\omega_{THz})$
$\bar{z}$
$\bar{x}$
$\bar{y}$
t_1
u
s_2
P
$\vec{k}(\omega_{THz})$
🟥 sagittal ($\bar{y}$-$\bar{z}$) plane
🟦 tangential ($\bar{x}$-$\bar{y}$) plane

Fig. 3.12 Conceptual schematic of PFT OR with 1030 nm wavelength pump.

a geometry has two generalized advantages: first, it allows for correction of input beam ellipticity, which is to a certain extent an inherent property of any real laser beam; and second, it allows for decoupling sagittal and tangential focusing. The latter provides an additional degree of freedom in chosing the crystal location for optimal balance between beam sagittal demagnification (i.e. fluence or peak intensity) and tangential demagnification (phase-matched PFT). These points are exemplified in Fig. 3.13 and Fig. 3.14.

3.5.2 Conversion Efficiency at Room Temperature

With the scheme described above, we are able to achieve an extracted[2] of up to 0.62% energy conversion efficiency at room temperature operation employing the maximum available energy at the crystal. The output energy curve in Fig. 3.16.a exhibits a quadratic behaviour

---

[2] Hereafter *extracted* efficiency refers to actual usable efficiency, that is, collected, transported, and measured at a calibrated detector.

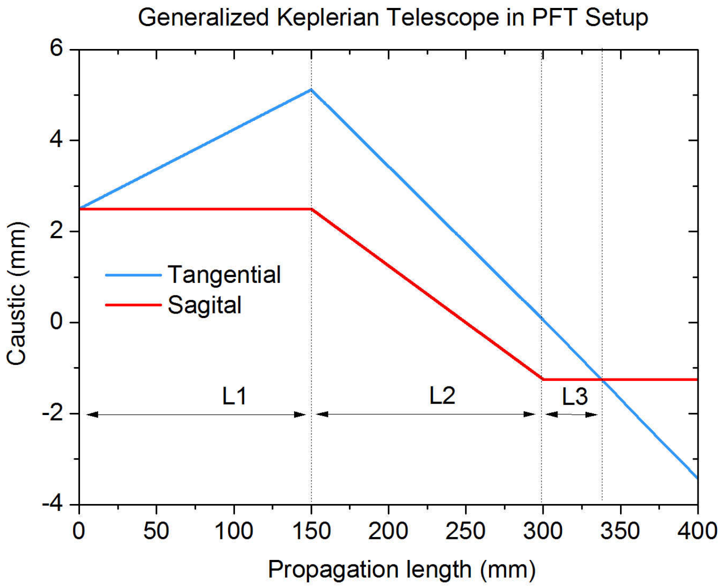

Fig. 3.13 Example design of caustic for a Keplerian (4f) telescope within a PFT setup valid for use in OR: L1 = 150 mm; f1 = 100 mm; f2 = 50 mm;.

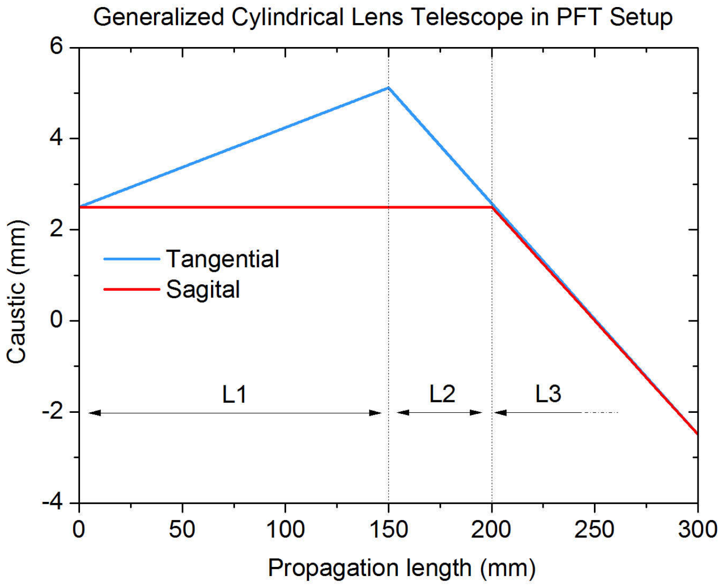

Fig. 3.14 Beam caustic for two cylindrical lenses within the PFT setup parameters listed in Table 3.1.

with respect to input intensity (recall Equation 3.2) and it shows slight saturation only for higher input fluences (Fig.3.16.b). Such high efficiency is supported by the strong cascaded broadening of the input pump spectrum, shown in Fig. 3.15, which suggests that the average number of cascaded cycles is of the order of 20 to 30. Consequently, the intrinsic conversion efficiency is of a few percent level and differs from the measured value due to losses mainly from linear absorption, FCA, Fresnel losses, and limited detection.

The input pulse duration is 1.75 ps FWHM (Gaussian pulseshape) instead of its Fourier-limited value of 0.7 ps. We will address this choice in the next subsection.

We have already seen in the previous section that determining the saturation fluence may be non-trivial experimentally —recall how both curves in Fig. 3.9 seem to slightly saturate at different input fluences—. However, it is clear from the curves that the system can be pushed to perform better until saturation of the conversion efficiency curve becomes apparent.

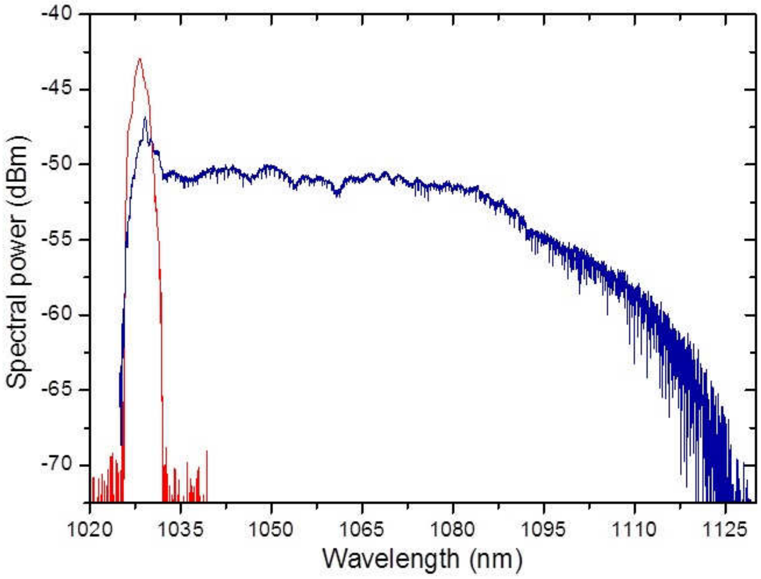

Fig. 3.15 Input infrared spectrum and corresponding broadened output spectrum due to efficient THz generation.

3.5.3 Influence of Chirp in Conversion Efficiency

The consensus on optimal temporal shape of the pump pulse is that Fourier-limited pulses yield higher conversion efficiencies than temporally stretched ones [69]. This rule of thumb arises primarily from the fact that the shortest available pulses for a given bandwidth lead to the highest peak-intensity, and therefore, assist in increasing the efficiency. We already observed this scaling law in our case study at 800 nm wavelength pump (Fig. 3.7). Recent theoretical studies suggest that the peak THz frequency and corresponding efficiency can be tuned by adjusting the Fourier-limited pump pulse duration in the sub-ps range [70].

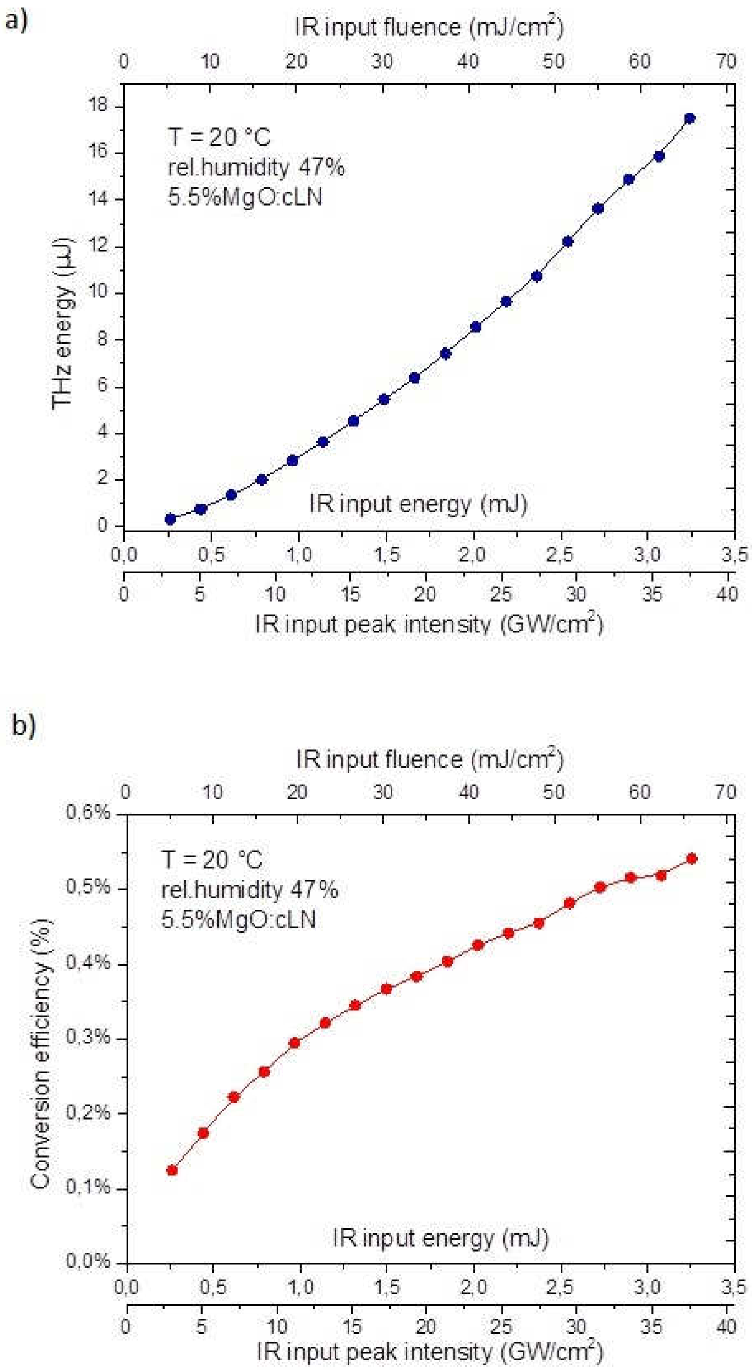

Fig. 3.16 a) Output THz energy as a function of input IR energy, fluence, and peak-intensity at 1030 nm pump wavelength and b) corresponding extracted conversion efficiency curve in cLN at room temperature.

We perform a simple experiment to show that Fourier-limited pulses are not necessary to achieve maximum conversion efficiency, and that in principle only enough bandwidth within the pump pulse is required to allow for spectral components to undergo a frequency down-conversion process. Moreover, we show that introducing group-delay dispersion (GDD) in the pump pulse of less than 10^6 fs^2 can significantly correct for alignment imperfections and optical aberrations, and that it can be chosen to maximize the effective length of the nonlinear interaction for THz generation. As a consequence, tuning of the pulse pre-chirp becomes a very powerful method to achieve optimal phase-matching conditions.

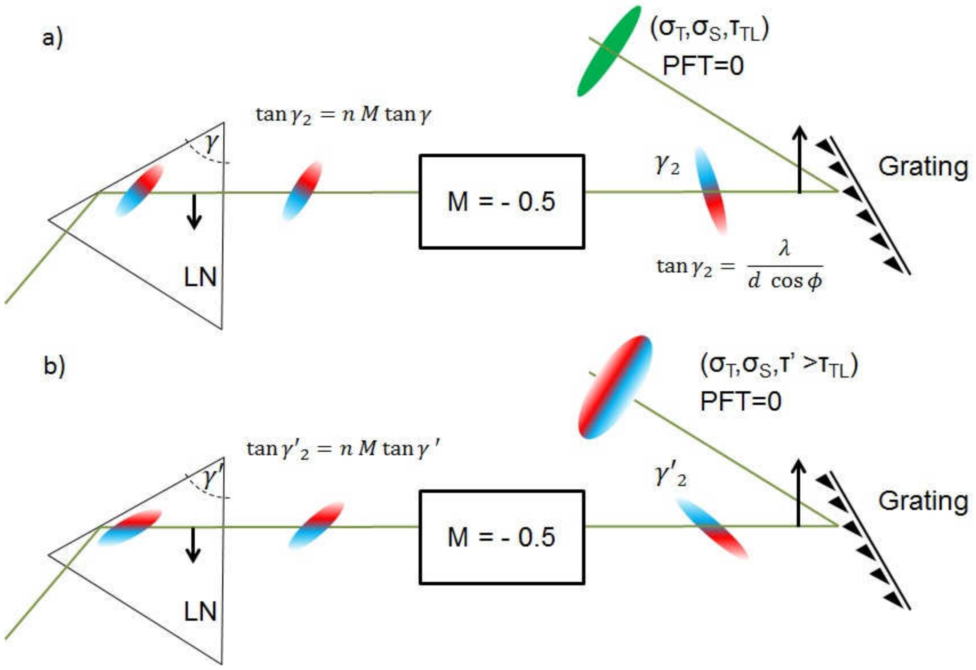
a)
$(\sigma_T, \sigma_S, \tau_{TL})$
PFT=0
$\tan\gamma_2 = n\,M\tan\gamma$
γ
LN
M = - 0.5
γ_2
Grating
$\tan\gamma_2 = \frac{\lambda}{d\,\cos\phi}$
b)
$(\sigma_T, \sigma_S, \tau' > \tau_{TL})$
PFT=0
$\tan\gamma'_2 = n\,M\tan\gamma'$
γ'
LN
M = - 0.5
γ'_2
Grating

Fig. 3.17 a) Conceptual PFT OR setup of a Fourier-limited input pulse through a M = -0.5 imaging system and b) corresponding PFT change with a negatively chirped input pulse in the same setup.

Fig. 3.17 depicts how temporally chirping the input pump pulse acts upon the final tilt of its intensity pulse front. By adding temporal dispersion, some spectral components will arrive earlier at the nonlinear interaction point both temporally and spatially. Therefore, pre-chirping the pump pulse is equivalent to fine-tuning the PFT angle. The collateral effect of temporal chirping is of course an increased pulse duration and it thereby acts upon a decline in peak intensity. However, such decrease does not necessarily imply a decline in conversion efficiency since near-saturation operation can be achieved by modifying the pump fluence at the crystal.

We verify this by acquiring another independent set of measurements similar to those in

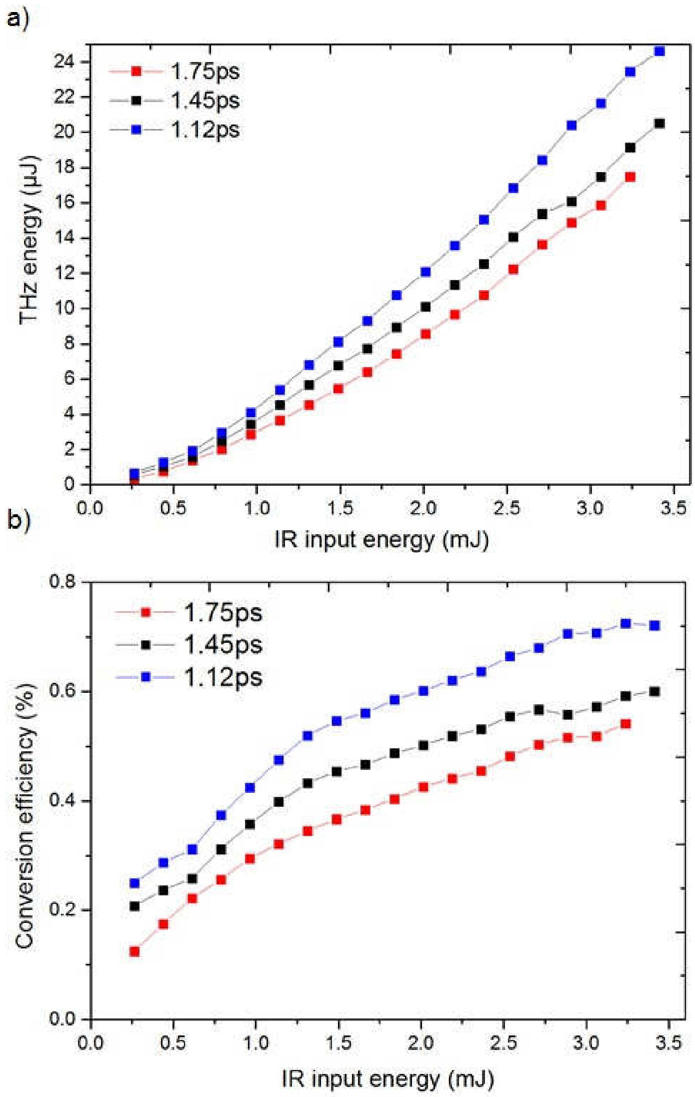

Fig. 3.18 a) Output THz efficiency as a function of input pump energy for the cases of 1.75 ps (red), 1.45 ps (black), and 1.12 ps (blue) optimal stretched pulse durations and b) corresponding conversion efficiency curves at room temperature.

Subsection 3.5.2 with a slightly higher fluences, shown in Fig. 3.18, and measured pump pulse duration of 1.45 ps and 1.12 ps FWHM (Gaussian pulse shape). The maximum peak-intensity here is about 5 GW/cm^2 and 10 GW/cm^2 higher than the one in Fig. 3.16 for the cases of 1.45 ps and 1.12 ps, respectively.

For comparison purposes, Fig. 3.18.a contains only the output THz energy as a function of input energy, since fluence and intensity differ in all three cases by design. We can derive from these measurements that adjusting the setup such that it would operate at its optimum with two shorter pulse durations (1.45 ps and 1.12 ps) yields a steeper rise in generated

THz energy. On the other hand, it is obvious that the curve saturates much quicker in this case too, possibly due to the stronger action of the photorefractive effect and FCA through multi-photon absorption. In any case, the main conclusion from these measurements is that there are multiple solutions to PFT OR in lithium niobate and that one must operate at an input fluence and intensity range close to saturation for maximum efficiency extraction, and that input pulse duration can be a design parameter, contrary to the general belief that only Fourier-limited pulses are optimal.

An alternative way of studying this effect is the dependence of conversion efficiency as a function GDD, in this case introduced from the double-pass two-grating compressor of the Yb:KYW regenerative amplifier. The results of these measurements are shown in Fig. 3.19. We derive from these curves that the strong decline in efficiency with respect to GDD arises primarily from the phase-mismatch introduced by the variation of the PFT and that this effect is dominant compared to an increase or decrease in peak-intensity. The effect of such mismatch also becomes apparent in the spatial distribution of the generated THz beam, shown in Fig. 3.20, where it shows a transverse Gaussian profile at optimal conditions (Fig. 3.20.a); and quickly loses energy and displaces tangentially for non optimal chirps (Fig. 3.20.b-d) as a result of only the higher THz frequencies components being phase-matched.

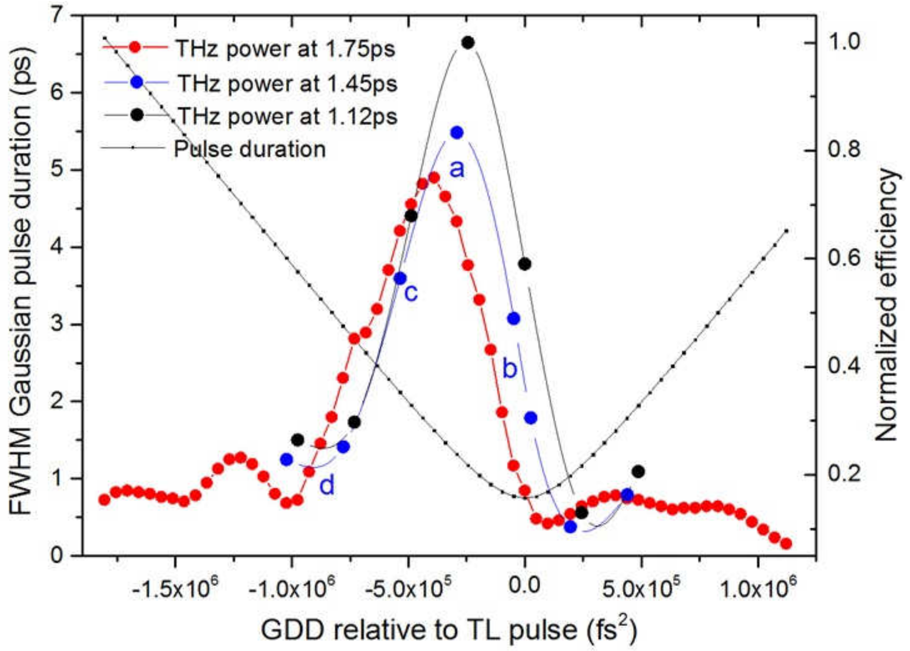

Fig. 3.19 Normalized efficiency and FWHM Gaussian-pulse duration as a function of GDD relative to Fourier-limited pulse in the cases of 1.75 ps (in red) and 1.45 ps (in blue) optimal pulse duration setups.

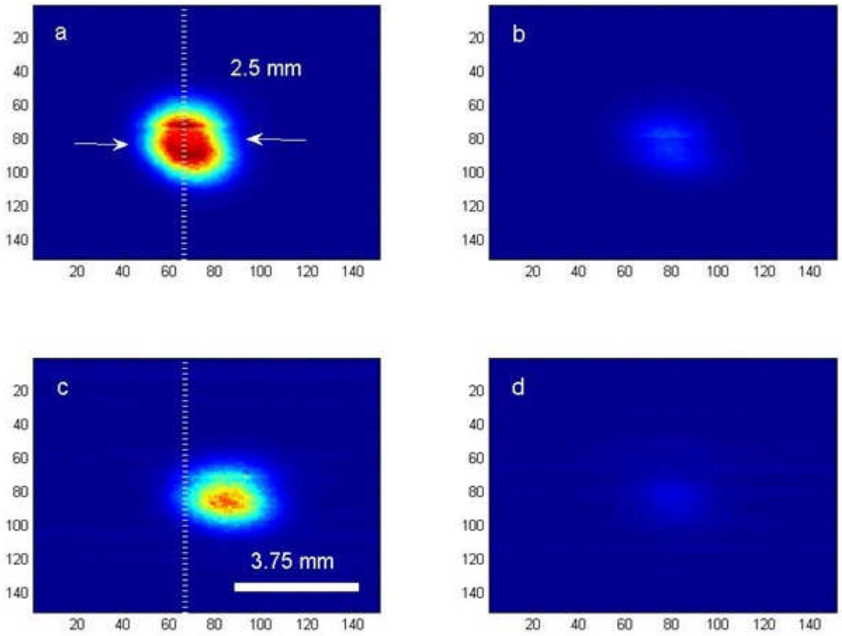

Fig. 3.20 Generated THz beam profile and relative intensity with the same color scale for four different points of pump pulse GDD as in Fig. 3.19.

3.5.4 Influence of Crystal Temperature

We have already shown that LN is a highly suitable material for efficient THz generation. However, the absorption coefficient of THz in LN at room temperature is of the order of 10-20 cm^{-1} [71, 72], which severely limits the conversion efficiency. This absorption arises primarily from acoustic phonon resonant absorption. In the 0.1 to 1 THz range, only the lowest phonon frequency modes are excited in LN and the absorption increases dramatically thereafter [73]. On the other hand, THz absorption in LN has already been shown to be substantially suppressed (about an order of magnitude) at cryogenic temperatures [74]. It is important to note that losses due to scattering from photorefractive effect are still present at low temperatures, although their impact is not fully documented [75].

We are able to characterize the improvement in extracted efficiency by cooling down the our same cLN crystal in the exact same arrangement described earlier for a 1.12 ps FWHM duration pump pulse. The results are summarized in Fig. 3.21. The trend is clear, there is approximately a fivefold increase in extracted conversion efficiency from room temperature to 110 K. The enhancement is more pronounced over the first 100 K cooling from room temperature, although it never ceases to increase as the temperature drops.

There is one important detail worth discussing. Note that the efficiency point at 300 K from Fig. 3.21 is about 0.42%, while the maximum efficiency we achieved using the same

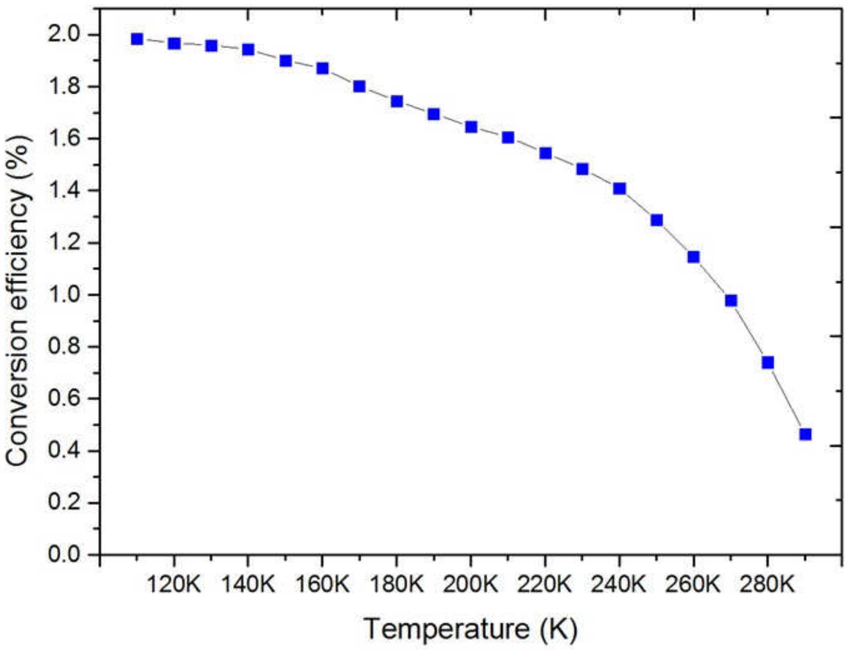

Fig. 3.21 Extracted conversion efficiency as a function of cLN crystal temperature.

pump beam —energy, beam shape, spectrum, and chirp —, as shown in Fig. 3.18 (Subsection 3.5.3), was almost twice higher, about 0.72%. The explanation for this disparity has already been discussed earlier in another context, which was exemplified by the different efficiency curve trends in Fig. 3.9 (Subsection 3.4.2). The rationale is the same: *every parameter change in a PFT setup introduces a new optimum set of conditions for maximum THz energy extraction.* In this case, the parameter change is temperature, i.e. THz absorption. The measurement was acquired by maximizing the efficiency at 110 K and then allowing the crystal to slowly thermalize. Since at cryogenic temperatures the absorption length is much longer than at warmer temperatures, we can allow for the pump beam to travel a longer effective distance (L) inside the crystal before cascaded broadening limits the process. Intuitively, as the temperature increases the new optimal length (L') is expected to be shorter than L, since as THz absorption begins to become non-negligible, a new balance between nonlinear interaction length and absorption length must be found. This is easy to set in numerical models, albeit impractical empirically. In this experiment, the position of the cLN crystal remains unchanged, and so, when it is finally thermalized, the pump beam is traveling a nonlinear interaction distance that does not overcome the strong effect of THz absorption. As a result, the extracted conversion efficiency is lower[3]. In other words, had each of the points in Fig. 3.21 been adjusted to its optimal interaction length, the enhancement from 300 K to 110 K would have been a factor of $\approx$2.7 (instead of 5).

---

[3] Note that the intrinsic THz conversion efficiency is the same for all temperatures

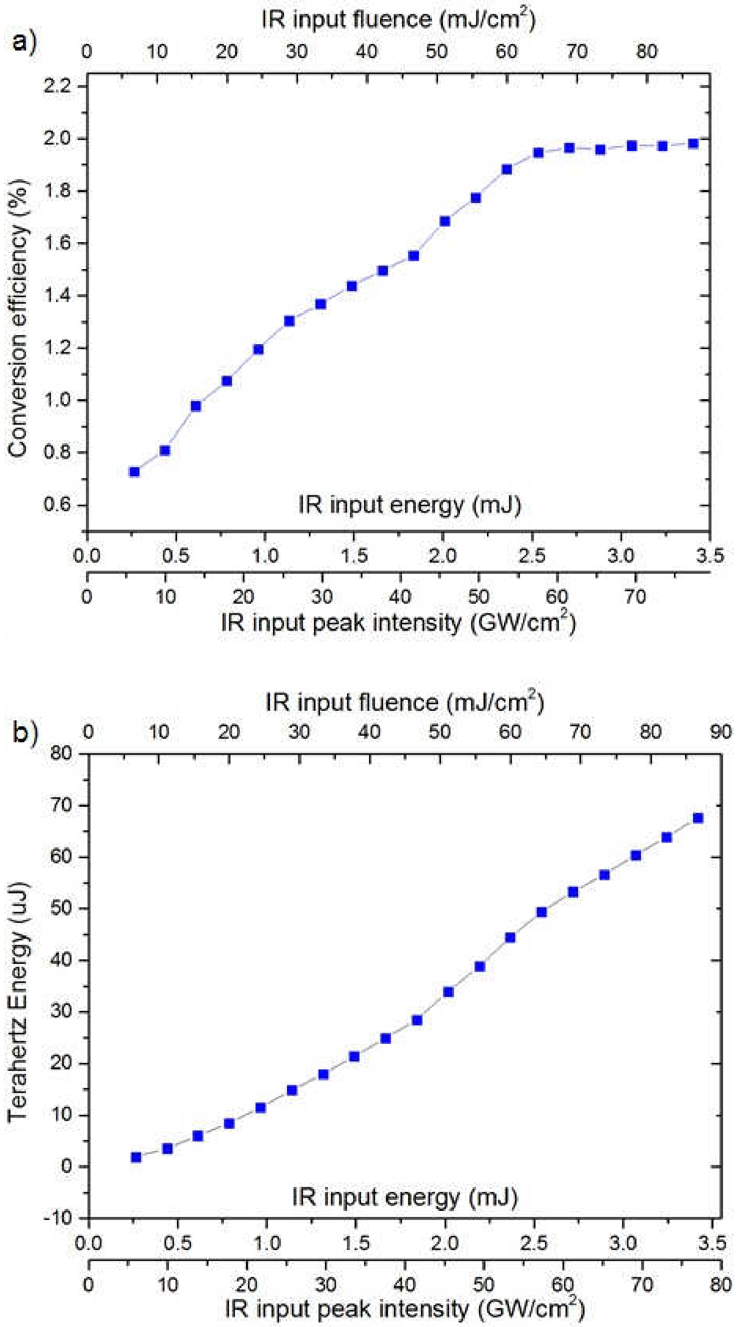

Fig. 3.22 a) Extracted conversion efficiency and b) THz energy as a function of input energy, fluence, and peak-intensity for a 1.12 ps pump pulse duration at 110 K cLN temperature.

Finally, by taking advantage of the low THz absorption at low temperatures, we reproduce similar curves to those in previous sections, that is, extracted energy and efficiency shown in Fig. 3.22, now at a constant crystal temperature of 110 K and obtain 67 μ of extracted energy at a record measured 2% extracted efficiency.

3.5.5 Intrinsic Conversion Efficiency

Intrinsic efficiency refers to an absolute transfer of optical energy to THz energy before it is absorbed, outcoupled, transported, and detected. Instrisic efficiency is not the practical (extracted) efficiency that reaches the experiment down the line, although understanding its scaling may point towards the ultimate physical limit, which can guide us through smarter approaches to either generate or extract THz more efficiently.

In light of estimating intrinsic efficiency, we look at the cascaded spectral broadening of the pump pulse. The shift of the optical power spectrum towards longer wavelengths may give us an accurate estimate of the nominal cascaded number of cycles N an optical photon experiences —recall Eq. 3.3 —and thus, derive how many THz frequency photons are generated during the DFG process.

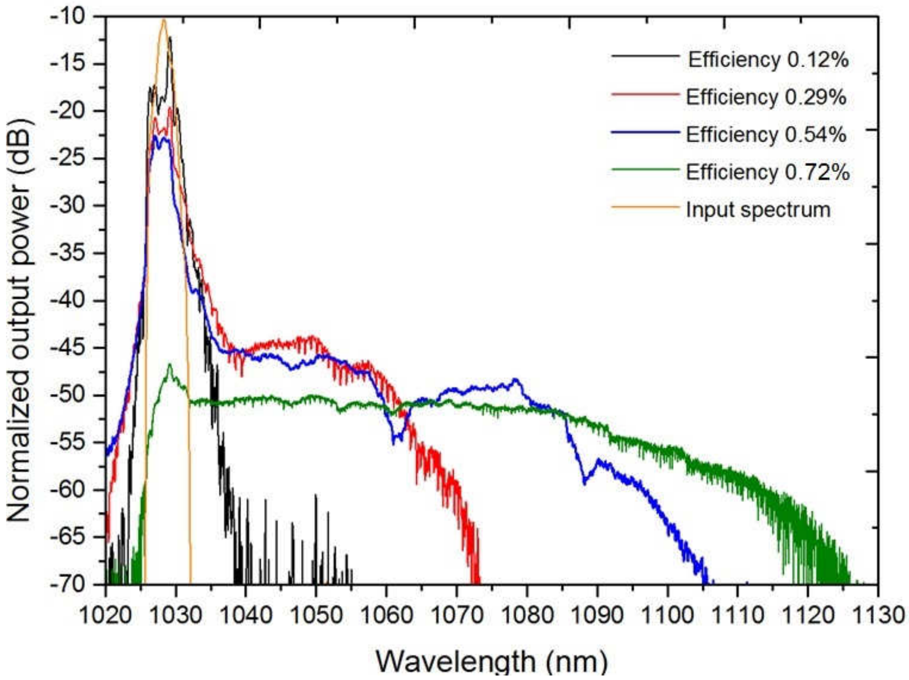

Fig. 3.23 Measured output pump power spectra in logarithmic scale and their corresponding extracted conversion efficiencies at 300 K.

Fig. 3.23 shows the different pump spectra for a variety of extracted efficiencies at room temperature. These spectra correspond to the same dataset as in Fig. 3.18 for a pulse duration of 1.12 ps. The input pulse spectrum is included for completeness. The red-shift becomes apparent as efficiency begins to increase and there is a comparatively much smaller but measurable blue-shift.

Table 3.2 Cascaded broadening at 300 K and estimated intrinsic conversion efficiency

Extracted efficiency (%)	**Spectral bandwidth** (nm)	**Center of mass** (nm)	**Cascaded cycles**	**Intrinsic efficiency** (%)
0 (input)	2.38	1028.4	0	0
0.12	3.36	1028.9	2	0.21
0.29	5.95	1030.2	3	0.31
0.54	9.6	1033	6	0.62
0.72	67.2	1057.7	27	2.77

Table 3.2 lists the calculated bandwidths and centers of mass of the spectra shown in Fig. 3.23. It also contains an estimated nominal number of cascaded cycles and the intrinsic conversion efficiency that would correspond to such number of cycles. Let us focus on the case of maximum broadening and extracted conversion efficiency of 0.72% at 300 K. This point of operation is similar to that for the extracted 2% efficiency at 110 K, and so is the broadening. Besides THz absorption, the only major causes for loss in extracted efficiency left are (i) outcoupling, which back-reflects about 20 to 30 % of the beam energy[4]; and beam transport. Since the effective interaction length of OR with PFTs is limited to a few millimeters at most (recall Fig. 3.8), it seems acceptable to assume that the THz absorption coefficient is rather negligible provided that our maximum extracted efficiency (2%) and intrinsic efficiency (2.77%) differ by about 38%, outcoupling and transport combined. These are only approximations derived from the nominal estimates of cascaded cycles. However, these simple calculations suggest that only efficiencies of the order of a few-percent may be physically possible under the presented scheme, which agrees in order of magnitude with our theoretical investigations [3].

3.6 Conclusions and Remarks

In conclusion, we have developed a system for PFT systems that, by (i) utilizing cylindrical lenses to custom-shape the pump spatial distribution; and (ii) exploiting the spectral-temporal shape of the pump beam, is able to emit THz radiation with well-above percent-level extracted conversion efficiencies and excellent beam quality (Fig. 3.24).

The difference between our intrinsic and extracted efficiencies still suggests that we may be able to find the means to improve THz outcoupling from the crystal and come up with efficient methods to transport the beam from source to application. As for PFT OR, there are other alternatives to explore efficiency scalability. One possible route relies on the improved

---

[4] This includes a single-layer broadband anti-reflection coating for THz. In fact, the reflectance off of the LN-to-air interface is 45%.

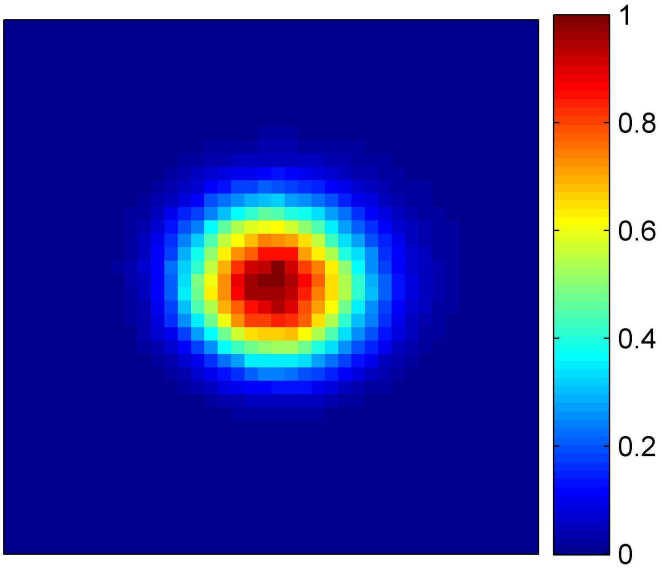

Fig. 3.24 Nearly diffraction-limited Gaussian THz focused beam with tangential and sagittal diameters of 0.73 mm and 0.83 mm FWHM, respectively.

fabrication process of stoichiometric lithium niobate (sLN)[5], which exhibits a higher nonlinear coefficient and decreased photorefractive effects, leading to an improvement of about 20% over the that of cLN.

Currently, the performance of our setup grants electric fields as high as 0.2 GV/m with 70 μJ energy, and beam focusable to nearly diffraction limit, specially suited for strong-field THz applications. These specifications already suffice the requirements for a THz gun capable of accelerating electrons above the 100 keV range from rest or to accelerate non-relativistic electrons to relativistic speeds in accelerating structures, for instance. Moreover, with scaling the pump energy by using cryogenic-Yb:YLF laser technology, THz operating regimes in the mJ-level and fields strengths of several GV/m are readily accessible, opening the possibility of direction acceleration of electrons in free space without the assistance of any additional structure or energy confinement method, and thus overcoming material limitations and inhomogeneities. The next chapter is dedicated towards this novel idea and describes a proof-of-principle experiment of in-vacuum longitudinal acceleration of electrons employing optical wavelengths.

---

[5] The largest pieces of sLN fabricated today do not exceed 2 to 3 cm length without imperfections. sLN is not a currently an option for high-power THz generation above the mJ-level since it cannot accommodate large pump beam dimensions.

Chapter 4

Free-space Longitudinal Acceleration of Electrons

4.1 Introduction

In this chapter we present a first-time observation of in-vacuum longitudinal laser acceleration of non-relativistic electrons that undergo accelerating gradients of up to 3 GeV/m and exhibit 3 mrad divergence from the co-linear interaction with an ultra-relativistic radially polarized laser. Our compact accelerator opens a new frontier for direct laser-driven particle acceleration capable of creating well collimated and relativistic attosecond electron bunches [76] and x-ray pulses [77].

4.2 Motivation

Compact laser-driven accelerators are versatile and powerful tools of unarguable relevance on societal grounds for the diverse purposes of security, health, science, and technology because they bring enormous practicality to state-of-the-art achievements of conventional radio-frequency accelerators. Current benchmarking laser-based technologies [78, 79] rely on a medium to assist the light-matter interaction and thus are generally challenged by conditions imposed by such an intermediary. The advent of few cycle ultra-intense radially polarized lasers [80] has materialized an extensively studied [48, 76, 81, 82] novel particle accelerator scheme that adopts the simplest form of laser acceleration and is unique in requiring no medium to achieve strong longitudinal energy transfer directly from laser to particle.

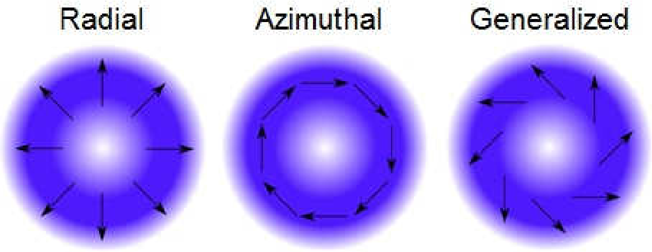

Fig. 4.1 Cylindrical vector beams are those that exhibit a transverse cylindrical symmetry of their fields, radial and azimuthal polarization being the most commonly known, and the generalized form, which is a combination of the two.

4.3 The Relativistic Few-cycle Radially-polarized Laser

There is an increasing interest in unconventional optical fields with spatially variant amplitude, phase, and/or polarization within the beam cross-section. Scalar optical vortices carrying orbital angular momentum and vectorial vortices from cylindrical vector beams, such as radially and azimuthally polarized beams, are among the most intensively studied examples. The added degrees of freedom arising from the amplitude, phase, and polarization diversity within the beam cross-section enables scientists and engineers to break the limits imposed by conventional wisdom in many optical and photonic applications.

In particular, the generation of radially polarized laser pulses with relativistic intensities can unfold new horizons in the nonlinear optical regime where laser-matter interactions are dominated by the relativistic motion of the electrons. High-energy few-cycle radially polarized sources remain relatively unexplored today. Traditionally, the generation of pulses with relativistic intensities has been limited to chirp pulse amplification-based techniques with linearly polarized lasers [83–85].

Radially polarized beams present several advantages compared to those with linear or circular polarization. They can be focused significantly tighter, hence entailing less demanding peak powers to reach any given optical fluence, and exhibit up to two times stronger longitudinal field intensities than transversely at the focal region [86, 87]. These features are relevant to a wide variety of applications requiring not only relativistic intensities but also to those uniquely sensitive to electromagnetic vector symmetry about the propagation axis or to those exhibiting a polarization vortex at the center of the beam, such as atomic and molecular dynamics [88], high-resolution second-harmonic generation [89], enhanced solid-state laser amplification [90], micromachining [91], and particle acceleration [48, 92, 93].

In this section, we focus on experimentally demonstrating a highly efficient linear-to-radial polarization mode conversion induced at the output of a few-cycle mJ-level hollow-

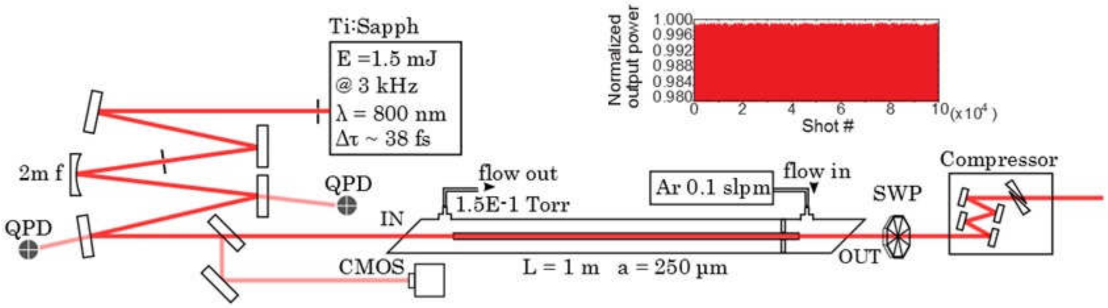

Fig. 4.2 Detailed schematic of high-energy high-power few-cycle radially polarized laser based on an Ti:Sapphire ultrafast laser system, a hollow-core fiber compressor and broadband polarization-mode converter.

waveguide compressor where nearly transform-limited few-cycle pulses with radial polarization are achieved. This scheme results in a radially-polarized 3-cycle laser centered at 800 nm routinely operating at peak and average power levels of 90 GW and 2 W, respectively, comprising the shortest pulse duration and the highest peak- and average-power radially polarized source reported to date [94–96]. Moreover, exploiting the intensity scalability in the few-cycle regime offers the additional benefit of reaching out to physical processes dependent on the carrier phase relative to the pulse envelope.

4.3.1 The Hollow-core Fiber Pulse Compressor

Lasers capable of generating multi-octave spanning and multi-mJ pulses allow for full control and tailoring of high electric field waveforms in the sub-femtosecond regime, which enables new opportunities in ultrafast science, chemistry, and particle physics. Extracavity compression techniques can meet such conditions and generate high-energy few-cycle and sub-cycle optical pulses. Two possible methods to reach such a goal are based on coherent waveform synthesis of either multiple broadband pulses from optical parametric amplifiers in the near- to mid-infrared bands or multi-color hollow-core fiber compressed pulses.

In hollow-core fiber (HCF) compressors, each of the input pulses undergoes spectral broadening and chirp that arise from the combined action of self-phase modulation (SPM) and group-velocity dispersion (GVD) in a gas-filled hollow-fiber [97]. The induced chirp can be independently suppressed by using standard compressors composed of chirped mirrors and prisms which in turn result on compressed pulses shorter than the input pulse due to the increased spectral bandwidth.

We develop a single-color HCF compressor based on a drive laser (Coherent Legend Elite Duo USP) that generates linearly polarized, up to 5-mJ pulses at 3 kHz repetition rate with 35 nm bandwidth centered at 800 nm wavelength. The carrier-envelope phase of the amplifier output can be locked within 200 mrad rms (10 shots integration).

The pulses are coupled into an Ar-filled dielectric hollow-waveguide, where they undergo spectral broadening. At high intensities, a pulse traveling through a nonlinear medium with index of refraction (linear and nonlinear) $n(\omega,I)$ can induce frequency shifts ($\omega(t)$) upon itself due to nonlinear phase shift ϕ_{NL}.

$$n(\omega,I) = n_0(\omega) + n_2 I(t) \tag{4.1}$$

$$\phi_{NL} = \frac{2\pi}{\lambda} n_2 I(t) L \tag{4.2}$$

$$\omega(t) = \frac{\partial \phi}{\partial t} \tag{4.3}$$

The leading edge shifts to lower frequencies and trailing edge to higher frequencies while the very peak of the pulse is not shifted (Fig. 4.3.b). This process creates new frequencies and broadens the initial pulse, which by properly compensating for the dispersion, leads to an output pulse shorter than the input pulse. The spectral broadening is proportional to the input power (P_0), interaction length (L), and Kerr term (n_2) and inversely proportional to the wavelength (λ) and effective nonlinear interaction area (A_{eff}). The maximum self-induced nonlinear frequency shift ϕ_{max} is

$$\phi_{max} = \frac{2\pi n_2}{\lambda A_{eff}} P_0 L \tag{4.4}$$

and the number of peaks (N) the broadened power spectrum will show can be approximated by

$$\phi_{max} \approx (N - 0.5)\pi \tag{4.5}$$

The hollow-waveguide has an inner diameter of 500 μm, an outer diameter of 2 mm and a length of 1 m. The Ar-gas flows along the waveguide in a pressure gradient geometry. As shown in Fig. 4.4, the optical output-end of the waveguide is set with constant laminar flow of Ar while the input is kept at 0.15 Torr, inducing an end-to-end net pressure drop of 10 psi. The combination of a large waveguide core-radius relative to the optical wavelength with a reduced optical-input gas pressure enables high pulse energy before detrimental self-focusing and ionization occurs at the input of the fiber, thereby maximizing spectral broadening and throughput.

For the purposes of this study, we spectrally broaden 2 mJ input pulses from the Ti:Sapphire

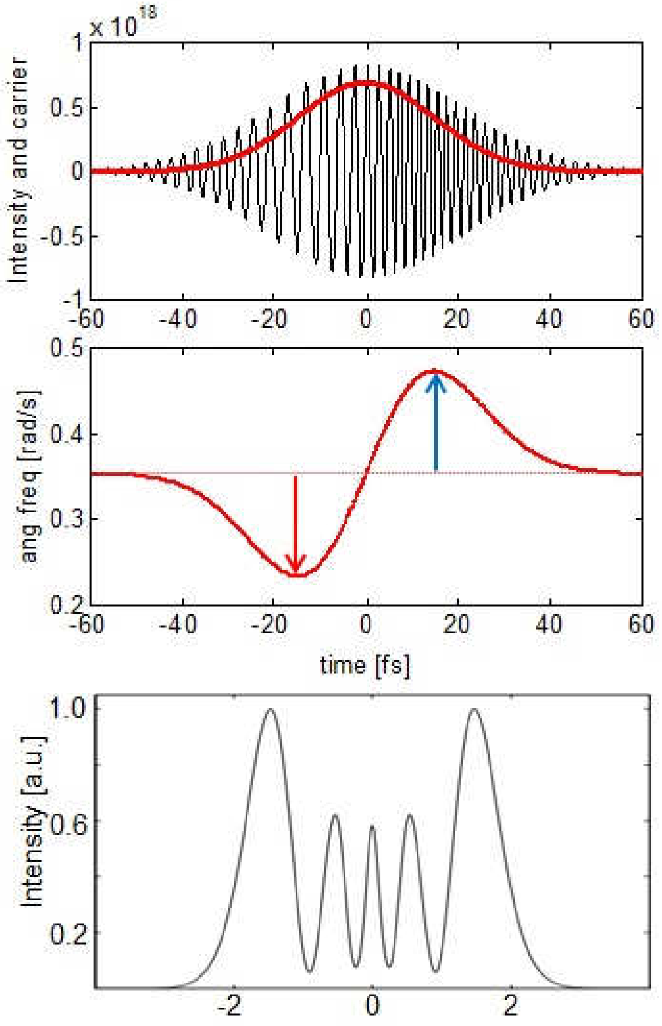

Fig. 4.3 a) Representative input ultrashort pulse and intensity carrier envelope. b) Instantaneous self-induced frequency shift and c) spectral broadening due to self-phase modulation.

amplifier to 130 nm FWHM bandwidth. The efficiency of the spectral broadening process is 60%, measured from input to output of the hollow-waveguide, in proximity to the maximum achievable value of 68% [98]. The major throughput loss contributors are identified as the following:

1. Waveguide attenuation ($\alpha_{EH11} \approx 9 \cdot 10^{-3}$ m^{-1}). Here are the waveguide constants, β, the phase constant, and α, attenuation constant, expressed as

$$\beta_{nm} = \frac{2\pi}{\lambda}\left\{1 - \frac{1}{2}\left(\frac{u_{nm}\lambda}{2\pi a}\right)^2\right\} \tag{4.6}$$

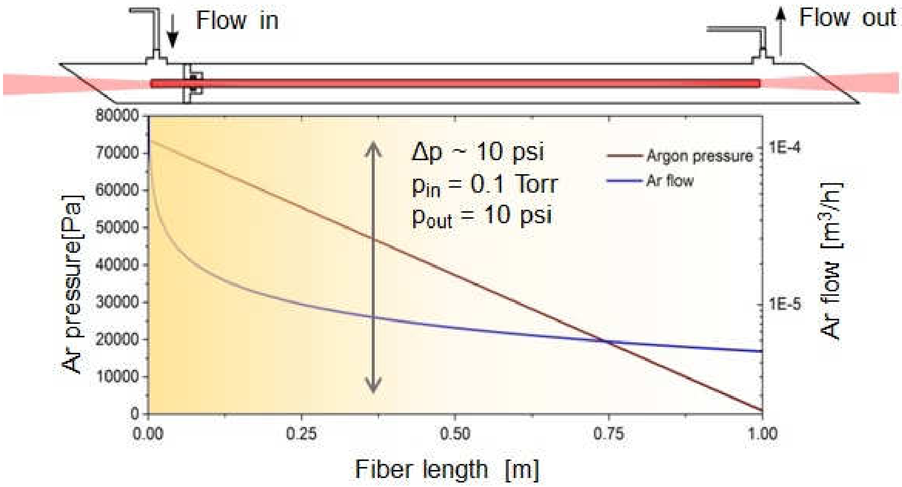

Fig. 4.4 Schematic of pressure gradient HCF compressor that assists in avoiding self-focusing and ionization losses.

$$\alpha_{TE0n} = \left(\frac{u_{0n}}{2\pi}\right)^2 \frac{\lambda^2}{a^3} \frac{1}{\sqrt{\nu^2 - 1}} \tag{4.7}$$

$$\alpha_{TM0n} = \left(\frac{u_{0n}}{2\pi}\right)^2 \frac{\lambda^2}{a^3} \frac{\nu^2}{\sqrt{\nu^2 - 1}} \tag{4.8}$$

$$\alpha_{EHnm} = \left(\frac{u_{mn}}{2\pi}\right)^2 \frac{\lambda^2}{a^3} \frac{0.5(\nu^2 + 1)}{\sqrt{\nu^2 - 1}} \tag{4.9}$$

where u_{mn} is the Bessel function coefficient for any given nm-index mode and a is the waveguide radius. It is interesting to note that the attenuation constants, here α, are proportional to λ^2/a^3, here ν is the normalized index of refraction of the dielectric waveguide. The losses can be made arbitrarily small by choosing the radius of the waveguide sufficiently large relative to the wavelength lambda.

2. Mode-coupling efficiency (η is lower than 98% for fundamental hybrid EH$_{11}$ mode). We will study this in more detail in the upcoming subsection.

3. Q-factor, or the energy in the fundamental hybrid EH$_{11}$ mode relative to the total energy (approximately 70 % in our specific case). The Q-factor is calculated using a quasi-discrete Hankel transform, where the electric-field amplitude can be decomposed as expressed here,

$$E(r,\lambda) = \sum c_m(\lambda) J_0\left(\alpha_m \frac{r}{a}\right) \tag{4.10}$$

where each coefficient is calculated as a function of fiber radius a, its electric field distribution and the corresponding Bessel function J_m as

$$c_m(\lambda) = \frac{1}{a^2 J_1^2(\alpha_{(m)})} \int_0^a E(r,\lambda) J_0\left(\frac{\alpha_m r}{a}\right) r dr \tag{4.11}$$

$$Q = \frac{\int |c_1(\lambda)|^2 d\lambda}{\sum \int |c_m(\lambda)|^2 d\lambda} \tag{4.12}$$

Spectral broadening is a nonlinear process strongly dependent on the input pulse intensity and shape, the laser pointing, and gas pressure. Therefore, a high spectral broadening efficiency in a large core-radius waveguide is indicative of maximized self-phase modulation, increased spatio-temporal output beam quality, intensity and spectral stability, and minimized cross-phase modulation between the fundamental and other co-propagating higher order leaky waveguide modes.

The output of the hollow-waveguide exhibits excellent long and short-term stability for practical applications. The short-term fluctuations of the broadened pulses account for <0.5% rms of the output intensity. With active stabilization of the input laser pointing the system operates stably for several hours. The broadened fundamental-mode is assumed to exit the waveguide near diffraction-limited and exhibits a quasi-Gaussian profile, 5 mrad divergence, and linear polarization. The pulses are temporally compressed employing a suitable set of double-chirp mirrors that compensate cumulative second and third order dispersions of 270 fs^2 and 190 fs^3, respectively. The throughput of the compressor is 86% and the FWHM pulse duration measured at the output is 8 fs, corresponding to a value 1.1 times the transform-limited pulse duration.

4.3.2 Linear to Radial Polarization Conversion

The last key element of our approach is a the polarization conversion. The approach of hollow-waveguide broadening after conversion from linear to radial polarization is disadvantageous for several reasons. Efficient coupling and propagation of the radially polarized (TM_{01}) ultrafast laser pulses in hollow-waveguides has only been demonstrated at low energies of the order of a few μJ [99]. While cylindrically symmetric vector modes TE_{0q} and TM_{0q} exist in circular waveguides for the entire wavelength spectrum, the dominant non-symmetric transverse modes in the infrared region are the hybrid EH_{pq} modes.

For spectral broadening of high energy pulses above few tens of μJ's the required waveguide core-radius becomes significantly larger. This condition imposes an underperformance of the TM_{01} mode relative to the fundamental EH_{11} mode that arises primarily

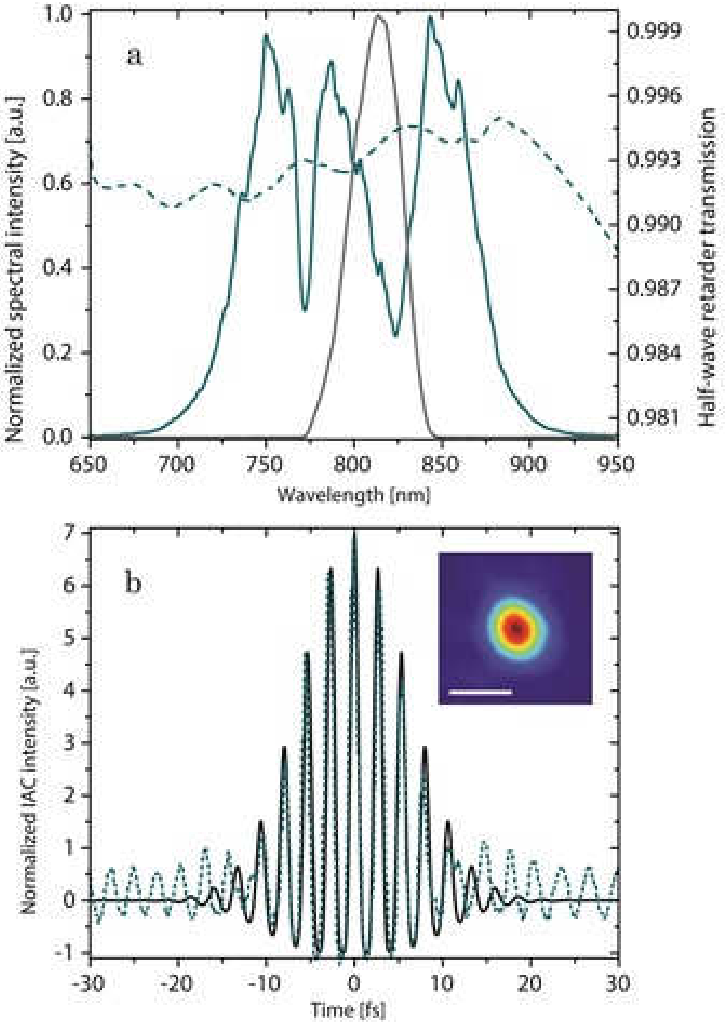

Fig. 4.5 a) Normalized input spectrum (gray), normalized output spectrum (solid cyan), and waveplate transmission curve (dashed cyan); (b) measured interferometric autocorrelator (IAC) signal (dashed cyan) and fitted IAC signal with a 8.06 ± 0.15 fs FWHM pulse duration, waveguide output far-field beam profile (inset); bar is 5 mm.

from a lower coupling efficiency, approximately 14% lower than the EH_{11} mode assuming a Gaussian beam, as shown in Fig. 4.6, and higher propagation losses in a hollow dielectric waveguide. The latter can be set to be arbitrarily small by utilizing a sufficiently large core radius since the attenuation constant is directly proportional to λ^2/a^3, where λ is the wavelength and a is the waveguide radius [100]. However, the ratio of attenuation constants between any given transverse-magnetic mode and hybrid mode is given by $\alpha_{TM0k}/\alpha_{EHnm} = 2\nu^2 \left(u_{0k}/u_{u_{nm}}\right)^2 / \left(\nu^2+1\right)$, where ν is the medium-normalized index of refraction and u_{ij} is the ij-th root of $J_1(u_{ij}) = 0$, where J_1 is the Bessel function of the first

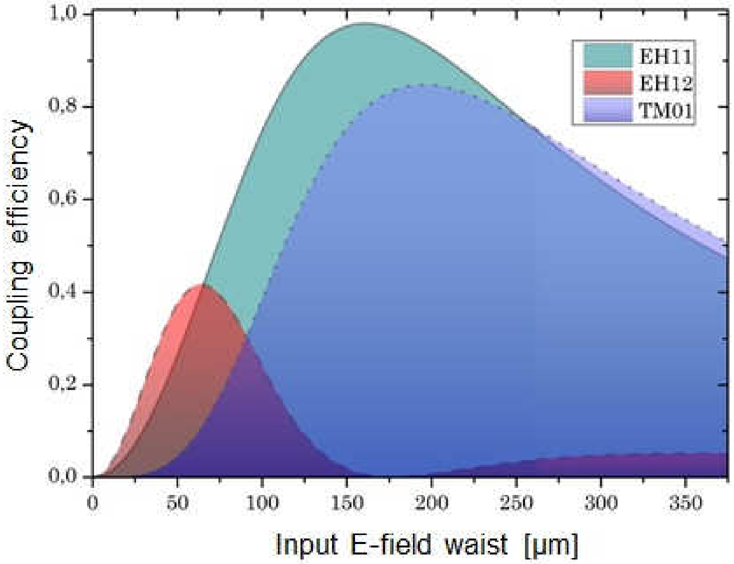

Fig. 4.6 Computed coupling efficiency as a function of electric field beam waist of linearly polarized Gaussian EH_{11} (solid) and EH_{12} (dashed) beams and linearly polarized Gaussian beam externally converted to TM_{01} (dotted) mode.

kind.

The first unfavorable implication of these conditions is that the minimum possible propagation loss of the TM_{01} mode will generally be restricted to be more than 3 times larger than that of the fundamental EH_{11} mode, and thus, the maximum achievable broadening factor and efficiency will be reduced. Another possible consequence is that energy launched into the preferred TM_{01} mode will transfer towards all other modes, especially towards the more dominant ones, generally leading to additional losses and manifesting an increased undesirable cross-talk between comparably strong propagating modes.

Practically, these limitations can be overcome by introducing a broadband polarization state converter at the hollow-waveguide output in order to preserve the high throughput and broadening factor of the gas-filled hollow-waveguide corresponding to the EH_{11} mode operation. We demonstrate this concept by employing a custom segmented achromatic waveplate consisting of eight $\lambda/2$ retarders over a 650-950 nm bandwidth range, each arranged with the slow birefringence axis rotated at ±11.25, ±37.75, ±56.25, and ±78.75 degree angles and same thickness [101].

The mode converter has a clear aperture of 20 mm in diameter and exhibits a measured throughput >96% for the spectrally broadened pulses. The converted radially polarized pulses from the segmented waveplate are compressed again down to 8 fs by slightly modifying the compressor to account for the increased dispersion, which comprises approximately

Table 4.1 Quick facts: pros and cons of polarization mode conversion before or after spectral broadening in hollow-waveguide

Before gas-filled hollow-waveguide
PRO: Good beam quality (spatial filtering)
PRO: Diffraction-limited pulse at output
CON: Lower coupling efficiency than fundamental EH_{11}
CON: Very high attenuation constant
CON: Smaller broadening factor
CON: Prone to inducing undesired cross-phase modulation

After gas-filled hollow-waveguide
PRO: High throughput through EH_{11} mode
PRO: Increased self-phase modulation and spectral broadening
PRO: Higher total efficiency
CON: Lower spatial beam quality

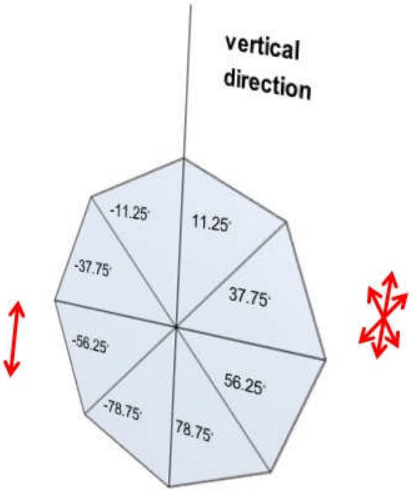

Fig. 4.7 Segmented waveplate (SWP): polarization mode converter.

a total of second and third order dispersion of 320 fs^2 and 210 fs^3, respectively. The retarder-induced phase difference across the bandwidth of these pulses remains small relative to their wavenumber, thus making it possible to compress them to a near transform-limited duration. However, this effect will become prominent when approaching the single-cycle limit.

This concept is directly transferable to the case of azimuthal polarization by introducing a quarter-wave retarder. Because of its cylindrical symmetry, the degree of polarization (P) is evaluated over the transverse 0, ±45, and 90 degree axes, where we find excellent polarization purity. The Stokes parameters S_0, S_1, S_2, and S_3 are calculated directly from

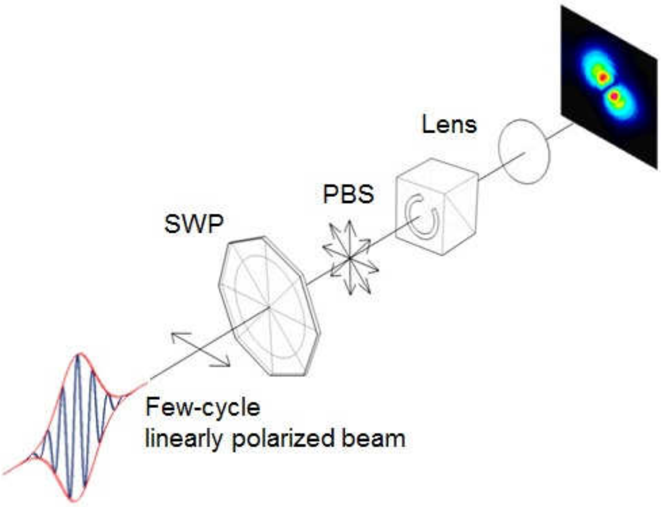

Fig. 4.8 The polarization purity is calculated directly from the visibility of the recorded images after mode conversion.

recorded images at all transverse analyzer orientation as depicted in Fig. 4.8. Using these calculated parameters, the polarization purity is verified quantitatively to exceed 93%, where $P = S_0^{-1}\sqrt{S_1^2+S_2^2+S_3^2}$ [102].

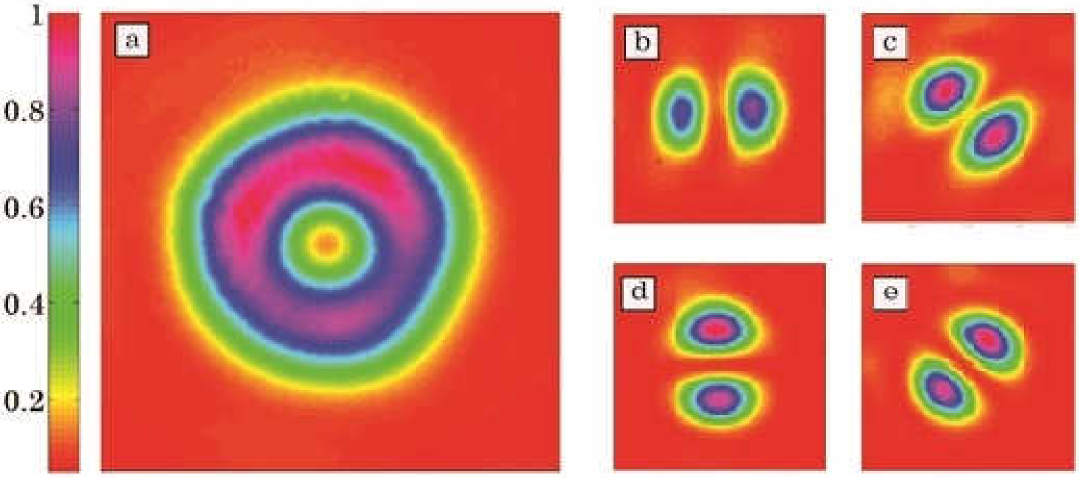

Fig. 4.9 Normalized transverse far-field intensity profile of 8 fs radially-polarized beam for (a) full beam, (b) 0-degree angle, (c) 45-degree angle, (d) 90-degree angle, and (e) 135-degree angle components.

Table 4.2 Few-cycle radially-polarized source summary

Output Energy	1.5 mJ maximum
Routine Peak-Power	90 GW
Routine Average-Power	2.4 W
Repetition Rate	3 kHz
Intensity Fluctuations	0.5% rms
Central Wavelength	810 nm
Bandwidth	135 nm
Pulse Duration	8 fs
Beam Divergence	5 mrad
Polarization	Linear/Radial/Azimuthal

4.3.3 Source Summary

In this section we have described a simple and robust technique to efficiently produce high peak- and average-power few-cycle radially polarized beams by adequately combining well-established optical technologies. We find that a segmented achromatic waveplate employed post-spectral broadening is a feasible method for polarization mode conversion of energetic few-cycle pulses. The excellent spatial quality and high radial-polarization purity of the beam make it now possible for these pulses to reach fluences well into the relativistic intensity regime of the order of 10^{19} W/cm^2. Further progress in the compression efficiency of the laser system will soon extend the outcome of this work to more energetic and shorter radially polarized pulses and scale up reachable intensities by an order of magnitude.

This demonstration has now become an enabling technology for emerging applications such as direct on-axis laser-based vacuum electron acceleration, which is the topic we will cover in the next section.

4.4 Longitudinal Acceleration of Electrons in Vacuum

Let us remind ourselves that high-energy few-cycle laser sources with cylindrical vector beams are especially of interest to relativistic laser-particle interactions because they exhibit cylindrical symmetry of the field-vector distribution and can therefore be focused much more tightly, down to about 0.6 times the cross-sectional area of the diffraction-limited foci of linearly polarized beams [86, 103]. As a consequence, the threshold power required to reach relativistic intensity levels becomes significantly less demanding. Moreover, the longitudinal field component of radially polarized focused beams is uniquely enhanced, with approximately twice the field-strength of beams with any other polarization, thereby making it the ideal driver for direct-field on-axis particle acceleration in vacuum.

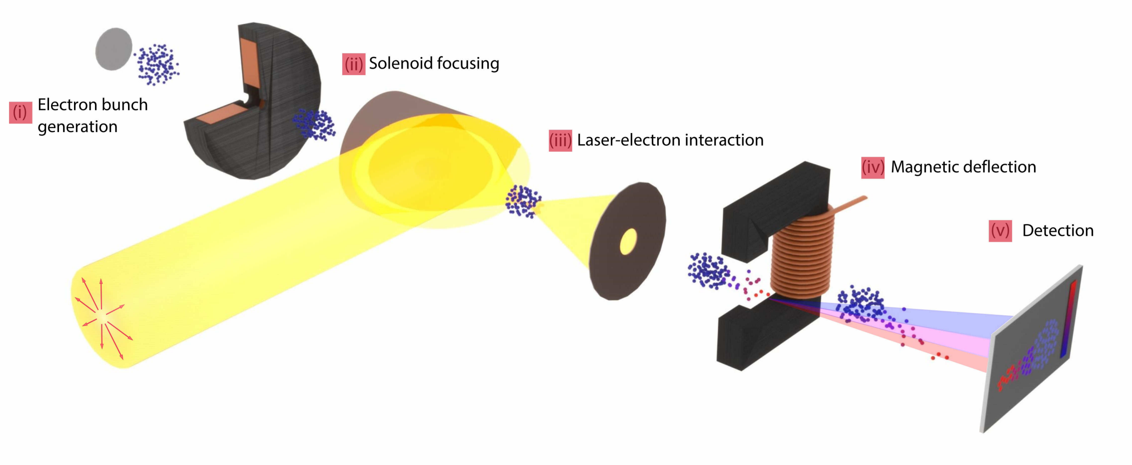
(i) Electron bunch generation
(ii) Solenoid focusing
(iii) Laser-electron interaction
(iv) Magnetic deflection
(v) Detection

Fig. 4.10 Concept of vacuum laser acceleration in a co-linear scheme using relativistic radially polarized laser pulses.

Despite these unique properties and their promising theoretical performance in direct particle acceleration, no experimental evidence of direct on-axis laser acceleration of electrons in vacuum has been reported to date. The fundamental reason behind this shortcoming has up until recently lied upon the inability of several distinct methods [104–106] to scale up and deliver the minimum intensity requirements for few-cycle radially polarized beams to access the relativistic regime of laser-electron interaction, well above 10^{19} W/cm^2 in the case of optical pulses for instance. In fact, this technological void has given way to other laser acceleration schemes [94, 107–112] today capable of yielding multi-GeV/m accelerating gradients and reaching well into the relativistic electron energy regime. However, these schemes entail a medium to intercede for net energy transfer, which may translate into material breakdown or wave-breaking regime limitations for instance in the case of inverse Cherenkov acceleration [94] and plasma wakefield acceleration [113], respectively, or still face several challenges —large emittance, energy spread, and divergence [113, 114] among others—which can severely hamper their use in practical applications. On-axis acceleration employing radially polarized laser pulses is inherently a purely free-space scheme capable of creating well-collimated and relativistic attosecond electron bunches [76, 77] and it is thereby in principle unrestrained from the limitations found in other methods.

4.4.1 Experimental Design and Setup

Here we show an unprecedented experimental demonstration that serves as a proof of principle for in-vacuum on-axis laser acceleration of electrons. On-axis acceleration takes advantage of the strong longitudinal electric field at beam center, where the transverse field components are null, to accelerate electrons directly along the optical axis without additional mediation. Fig. 4.11 shows the expected spatial field distribution. The dashed lines map the threshold where

$$w(z) = \frac{w_0}{\sqrt{2}}\sqrt{1+(z/z_0)^2} \tag{4.13}$$

and we expect electrons inside these dashed lines to be largely affected by linear forces and pushed ponderomotively otherwise.

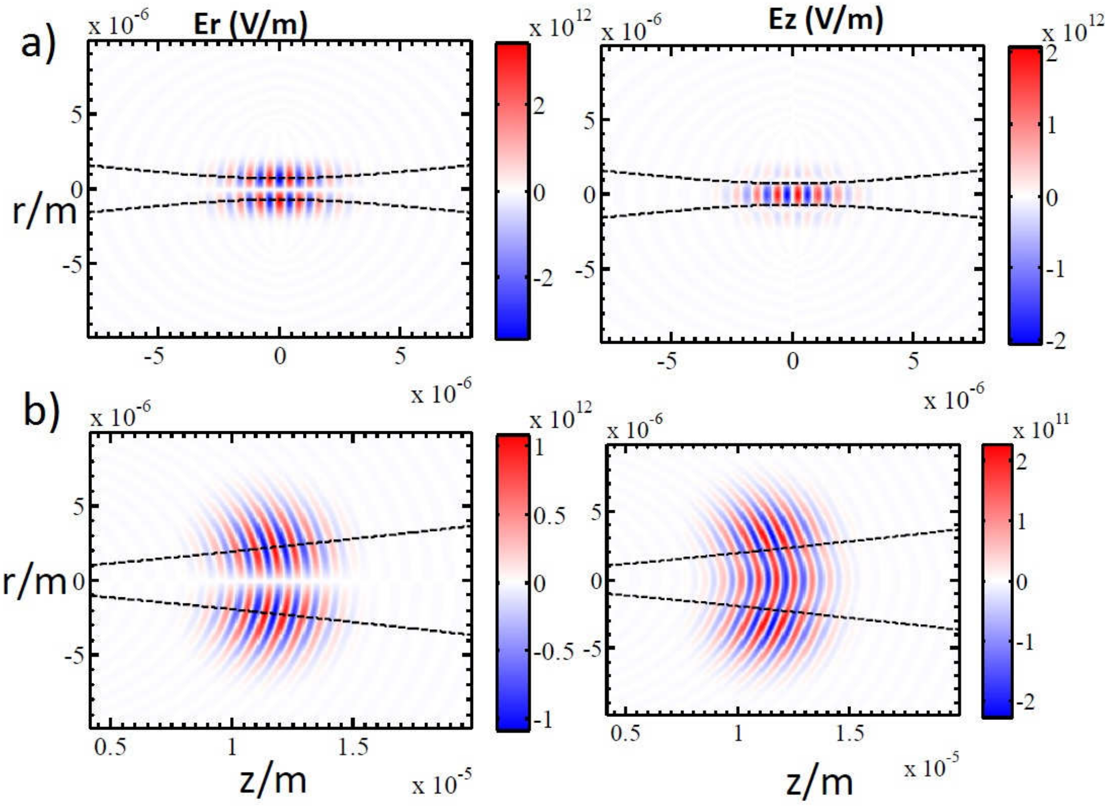

Fig. 4.11 Colormap of spatial field distribution of a $\lambda_0 = 800nm$, $w_0 = 1.2\mu m$; 3-cycle FWHM; and 600 μJ radially polarized laser beam focused by a NA=1 perfect lens centered at a) waist (maximum intensity and interaction point) and b) 40 fs after a).

The key enabling technology is our few-cycle radially polarized laser. The quality of our beams grants propagation factors close to the unity and hence high focusability to access the relativistic intensity regime, defined as the region for which the ratio between the classical electron oscillation and the speed of light in vacuum exceeds unity - the normalized vector potential (a_0) denoted as

$$a_0 = \frac{eE}{m\omega_0 c} = \sqrt{\frac{I_{18}\lambda^2}{1.37}} \tag{4.14}$$

where e is the elementary charge, E is the field amplitude, m is the electron mass, ω_0 is the field central frequency, c is the speed of light in vacuum, I_{18} is the field intensity in W/cm^2, and λ is the field wavelength in μm.

Here, that ratio can reach as high as $a_0 \approx 5$. In this regime, non-relativistic electrons can pick up a significant amount of energy from the laser field and undergo gradients in the order of several tens of GeV/m, where the maximal net electron energy gain is proportional to the field intensity as well as the beam waist at focus [115]. The nature of the laser-electron interaction is twofold:

1. Non-zero azimuthal angle electric field components may offer transverse confinement of the particles while
2. They are accelerated (and decelerated) directly from the linear force exerted by the strong longitudinal component of the electric-field, uniquely available through cylindrically symmetric vector beams.

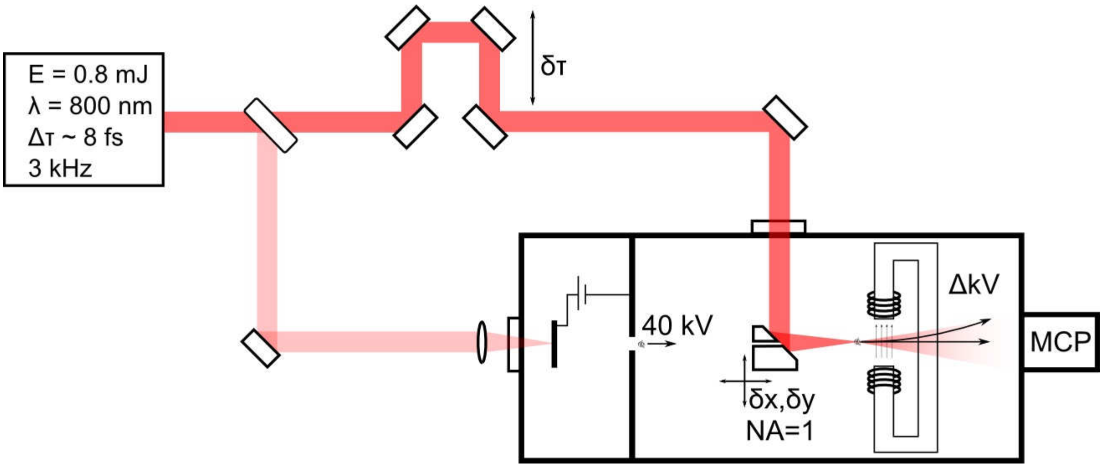

Fig. 4.12 Concept of vacuum laser acceleration in a co-linear scheme using relativistic radially polarized laser pulses.

Our experimental setup is depicted in Fig. 4.12. The monoenergetic electron bunch is generated from a photocathode excited by a small portion (2 μJ) of the radially polarized beam and accelerated to via a 40 kV DC gun. The focusing solenoid is 4.45 mm thick, has a radius of 2.75 mm, and is located 24.8 mm from the photocathode. The 40 keV electron beam from the photocathode is 1 mm long and it is assumed to exhibit an even electron distribution over all phases of the laser field. The 90-degree off-axis parabola used to focus the laser beam is 25.4 mm in diameter with a 25.4 mm effective focal length (NA=1), has a 1 mm through-hole and is located a few millimeters off the exit of the solenoid (Fig. 4.13). A pinhole was drilled by the laser source in situ and located for alignment near the interaction point (IP) to ensure maximal overlap between both transverse orthogonal dimensions of the bunch and the laser beam. The total bunch charge thereafter is 5 fC. The laser is focused with a high-NA parabolic mirror to a waist of 1.2 μm with a confocal parameter of 4 μm. The instrument is designed to limit the acceptance angle of electrons with less than 25 mrad azimuthal angle. We utilize a low-energy electron spectrometer consisting of magnetic dipole deflector (tangential plane) and a micro-channel plate with a nominal resolution of 100 eV/pxl. The magnetic dipole is located 10 cm away from the interaction point. The distance between the deflector and the micro-channel plate is 18 cm. The footprint of the entire interaction chamber is no larger than 0.5 m^2.

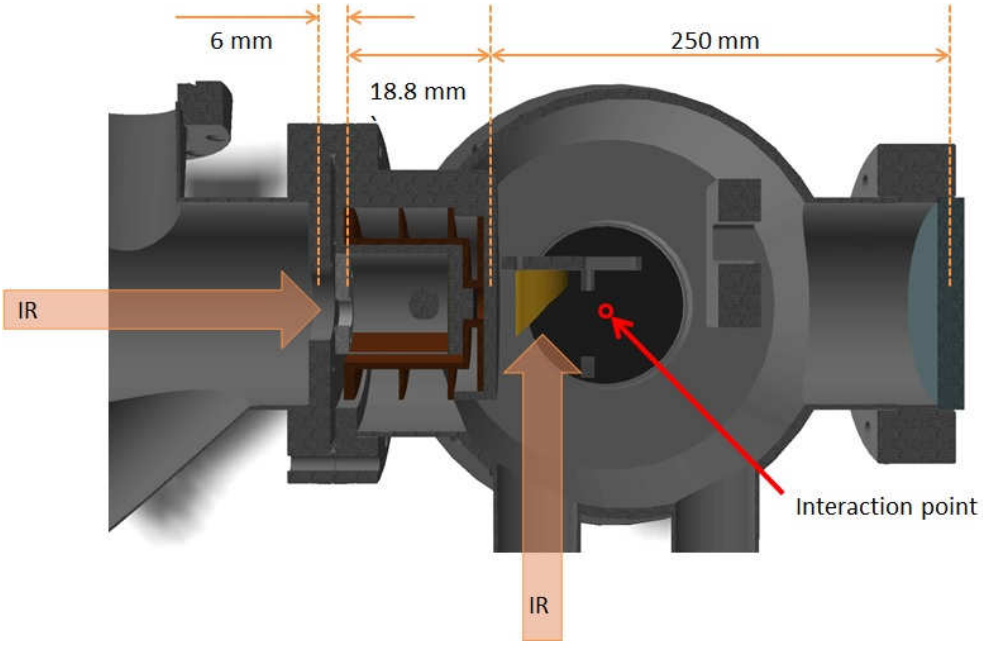

Fig. 4.13 Technical drawing of 40 keV DC electron gun and interaction chamber.

First, we determine the exact spatio-temporal coincidence of the laser and electron beams by the time-response of electron beam distortions arising from local charge due to photoionization on the edges of thin carbon film aperture at the IP. The electron undergoes observable distortions when it arrives shortly after the laser pulse at the aperture as a result of photon-induced localized charge, while no change shows if it arrives before the laser pulse. The modeled plasma density in the carbon film aperture is determined by the photo-emitted electron time-of-flight in the region of interest.

In general, all exposure measurements were carried out with the following procedure:

1. E-beam exposure: 2 consecutive independent acquisitions of 60 seconds long each with the laser OFF and e-beam ON.
2. Interaction exposure: 2 consecutive independent acquisitions of 60 seconds long each with the laser ON and e-beam ON.
3. Background exposure: 2 consecutive independent acquisitions of 60 seconds long each with laser ON and e-beam OFF.

4.4.2 Experimental Results

We denote τ=0 hereafter as to the relative time (τ) at which the accelerated charge peaks as a result of direct laser-electron interaction. Fig. 4.14 shows that the time-window of this interaction is 5 ps wide, as expected from a millimeter-long electron bunch traveling at a velocity 0.39c. The detected charge arises from accelerated electrons only in the deflection plane and does not exhibit any symmetry with respect to the laser field vector distribution. As a result, the direct interaction manifests itself as an increased energy spread of the electron beam with very small or negligible off-axis trajectory angle, where only the electrons close to the center of the focused beam are propelled forward.

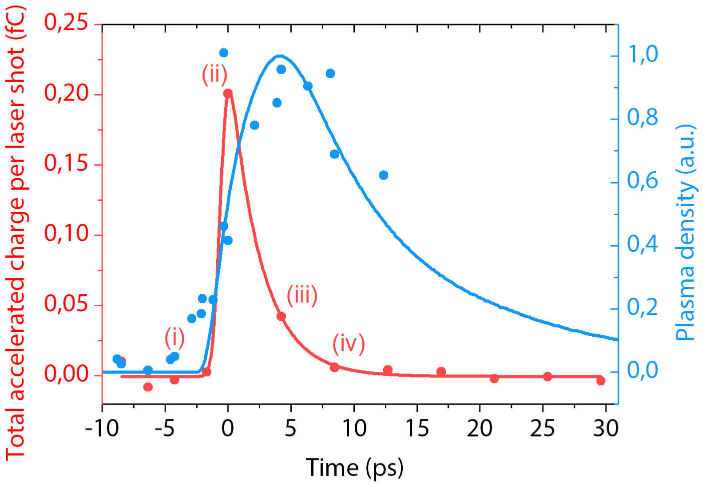

Fig. 4.14 Electron-laser beam coincidence timing and normalized charge of detected accelerated electrons as a function of laser-electron timing delay (τ).

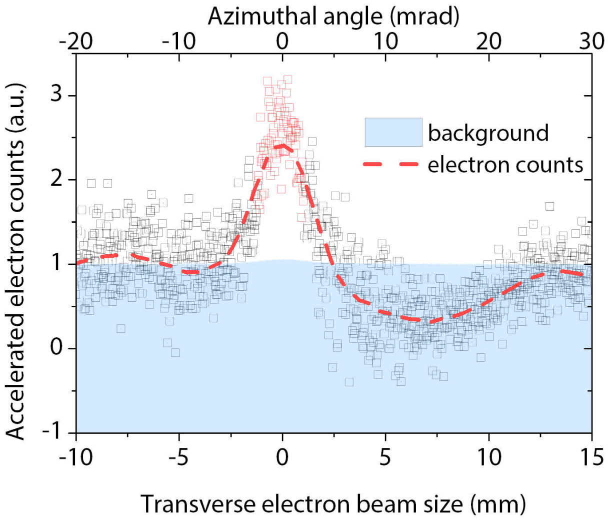

Fig. 4.15 Accelerated electron counts contained in the deflector plane at $\tau = 0$.

The divergence of the accelerated charge is less than 3 mrad FWHM, as shown in Fig. 4.15. The relative strength of the acceleration and optimum overlap are depicted in real- and momentum-space at four distinct laser-electron overlapping times in Fig. 4.16. The electron bunch reveals a 5 mm transverse size at the detector plane with a nominal ratio between the longitudinal- and transverse-momentum components of about 200 to 1.

4.4.3 Model and Analysis

In order to describe this interaction, we perform simulations based on a particle-tracking model beyond the paraxial and slowly varying envelope approximations. This model uses pulsed, radially-polarized laser beams with an exact, singularity-free solution to Maxwell's equations [116]. We are able to fully recreate the spatial and momentum distribution of $4 \cdot 10^5$ particles anytime during and after collision. We restrain our attention to only an electron ellipsoid contained in the high intensity volume of the optical pulse. The electrons start off with an initial energy of 40 keV in field-free vacuum and interact with the 0.6 mJ, 8 fs FWHM Gaussian pulse at the focus of the radially polarized beams with a waist of 1.2 μm.

When the laser pulse reaches the significantly slower 40 keV KE electron ellipsoid, the transverse portion in the center experiences acceleration from the largest longitudinal components of the laser field, which reaches its maximum on-axis. Out of the central region, the electrons undergo a strong ponderomotive force. Fig. 4.17.a depicts the modeled and measured final energy distribution of such scenario. A significant portion of electrons further from the center may also be launched forward as well in phase ranges where the longitudinal

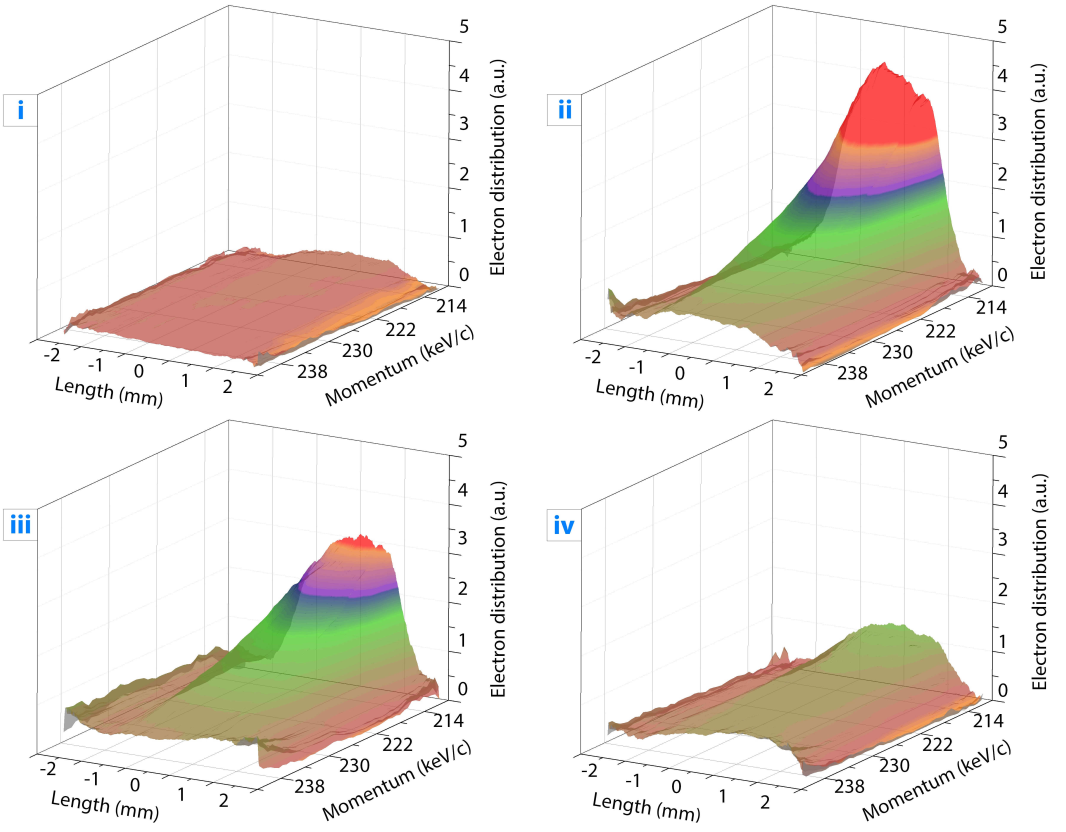

Fig. 4.16 Snapshots of the normalized distribution in real- and momentum-space of accelerated electrons at four different temporal overlaps (linked to Fig. 4.14: (i) there are no accelerated electrons when the initial electron bunch arrives at the IP 8.5 ps before the laser; (ii) distribution at the peak of total accelerated charge ($\tau = 0$) them beam is delayed by (iii) 4.25 ps and (iv) 8.5 ps with respect to the laser field.

fields are accelerating and transverse fields are focusing. This combined effect may offer proper transverse confinement while accelerating particles along the beam axis.

As shown in Fig.4.17.b, the modeled FWHM half-angle divergence of the electron bunch is 3.28 mrad, in very close agreement with the measured value. The predicted final kinetic energy distribution also matches the distribution measured at τ=0, shown in Fig. 4.18, which accounts for 4% of the total charge contained in the main electron beam, that is, 0.2 fC of accelerated charge per laser pulse. The net KE energy gain is strongest within a few keV and is measurable and statistically reproducible to up to 12 keV, comprising a 30% energy modulation of the initial KE of the non-relativistic electron bunch. These results demonstrate an unprecedented compact longitudinal laser accelerator exhibiting up to 3 GeV/m longitudinal accelerating gradients at a minimum brilliance of 250 electrons/(s·mrad^2·mm^2·0.1%BW).

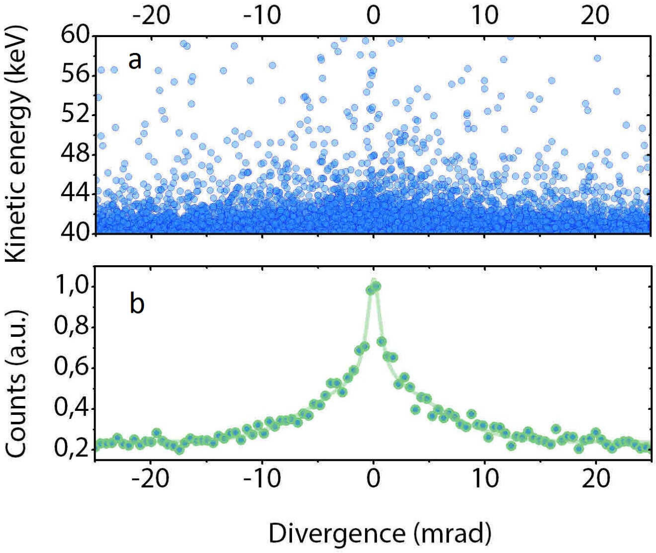

Fig. 4.17 a) Modeled final electron kinetic energy as a function of azimuthal angle in the region of study with half-angle deflection of less than 25 mrad and b) corresponding histogram as a function of divergence in the kinetic energy region ranging from 42 keV to 53 keV.

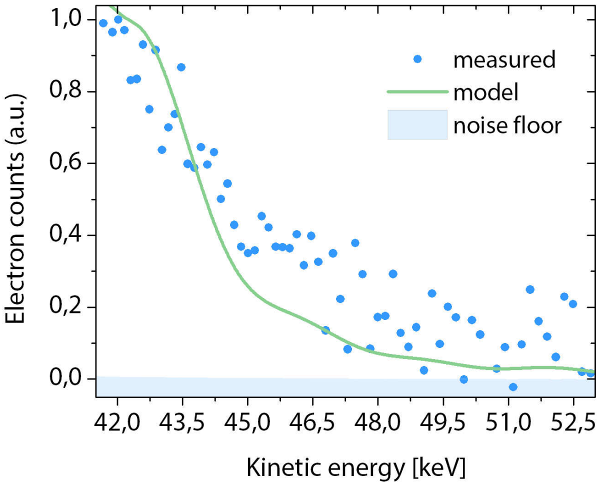

Fig. 4.18 a) Modeled final electron kinetic energy as a function of azimuthal angle in the region of study with half-angle deflection of less than 25 mrad and b) corresponding histogram as a function of divergence in the kinetic energy region ranging from 42 keV to 53 keV.

4.5 Conclusions and Remarks

In conclusion, we have first demonstrated a robust source to produce nearly diffraction-limited 3-cycle radially polarized pulses at 3 kHz repetition rate exhibiting strong longitudinal components at focus and capable of reaching relativistic intensities with only sub-mJ level energies. The general approach of combining external compression and polarization mode-conversion mechanisms is wavelength and bandwidth tunable, and in principle readily scalable to TW peak-power levels. Employing this source, we have performed a proof-of-principle experiment to demonstrate an unprecedented compact electron accelerator with 3 GeV/m longitudinal accelerating gradients.

This technology has now the ability to access net KE gains to relativistic velocities when combined with radio-frequency injector technology, since the final momentum of the particles scales significantly with increasing their initial momentum. At higher pulse energies, our method has been theoretically predicted to be capable of accelerating charged-particles from rest to relativistic velocities by an ultrashort interaction within the tightly focused few-cycle laser pulse, and thus reduce space-charge effects arising from Coulomb interactions. Moreover, this type of accelerator is uniquely capable of well-collimated tunable attosecond electron bunches and x-ray pulses. Alternatively, our concept is directly transferable to any generalized form of direct longitudinal acceleration of electrons to higher energies and larger brilliance by upscaling the laser intensity and wavelength, respectively, and thus sets the stage for the development of future atomic time- and space-scale resolution electron microscopy and tomography instruments, and high-brilliance tunable and coherent long-wavelength and attosecond x-ray sources. In fact, this technique can be extended to the use of sub-cycle waveform synthesized radially polarized pulses in photoemission from nanoemitters for an electron source to generate attosecond electron bursts with tunable kinetic energy up to relativistic velocities and focusability to the Heisenberg limit.

References

[1] L. E. Zapata, D. J. Ripin, and T. Y. Fan, “Power scaling of cryogenic yb:liyf4 lasers,” *Opt. Lett.*, vol. 35, pp. 1854–1856, Jun 2010.

[2] H. Yang, “High energy femtosecond fiber laser at 1018 nm and high power cherenkov radiation generation,” *MIT EECE M.Sc. Thesis*, Sep 2014.

[3] K. Ravi, W. Ronny Huang, S. Carbajo, X. Wu, and F. Kärtner, “Limitations to THz generation by optical rectification using tilted pulse fronts,” *ArXiv e-prints*, June 2014.

[4] R. Adair, L. L. Chase, and S. A. Payne, “Nonlinear refractive index of optical crystals,” *Phys. Rev. B*, vol. 39, pp. 3337–3350, Feb 1989.

[5] R. Adair, L. L. Chase, and S. A. Payne, “Nonlinear refractive-index measurements of glasses using three-wave frequency mixing,” *J. Opt. Soc. Am. B*, vol. 4, pp. 875–881, Jun 1987.

[6] W. Röntgen, *Ueber eine neue Art von Strahlen: 1.[-3.] Mittheilung*. Annalen der Physik und Chemie, Barth, 1898.

[7] W. Chao, P. Fischer, T. Tyliszczak, S. Rekawa, E. Anderson, and P. Naulleau, “Real space soft x-ray imaging at 10 nm spatial resolution,” *Opt. Express*, vol. 20, pp. 9777–9783, Apr 2012.

[8] W. Chao, B. D. Harteneck, J. A. Liddle, E. H. Anderson, and D. T. Attwood, “Soft X-ray microscopy at a spatial resolution better than 15 nm,” *Nature*, vol. 435, pp. 1210–1213, June 2005.

[9] F. Brizuela, S. Carbajo, A. Sakdinawat, D. Alessi, D. H. Martz, Y. Wang, B. Luther, K. A. Goldberg, I. Mochi, D. T. Attwood, B. L. Fontaine, J. J. Rocca, and C. S. Menoni, “Extreme ultraviolet laser-based table-top aerial image metrology of lithographic masks,” *Opt. Express*, vol. 18, pp. 14467–14473, Jul 2010.

[10] H. N. Chapman, A. Barty, M. J. Bogan, S. Boutet, M. Frank, S. P. Hau-Riege, S. Marchesini, B. W. Woods, S. Bajt, H. W. Benner, R. A. London, E. Plonjes, M. Kuhlmann, R. Treusch, S. Dusterer, T. Tschentscher, J. R. Schneider, E. Spiller, T. Moller, C. Bostedt, M. Hoener, D. A. Shapiro, K. O. Hodgson, D. van der Spoel, F. Burmeister, M. Bergh, C. Caleman, G. Huldt, M. M. Seibert, F. R. Maia, R. W. Lee, A. Szoke, N. Timneanu, and J. Hajdu, "Femtosecond diffractive imaging with a soft-X-ray free-electron laser," *Nature Physics*, vol. 2, pp. 839–843, Nov. 2006.

[11] S. Eisebitt, J. Luning, W. F. Schlotter, M. Lorgen, O. Hellwig, W. Eberhardt, and J. Stohr, "Lensless imaging of magnetic nanostructures by X-ray spectro-holography," *Nature*, vol. 432, pp. 885–888, Dec. 2004.

[12] J. Miao, P. Charalambous, J. Kirz, and D. Sayre, "Extending the methodology of X-ray crystallography to allow imaging of micrometre-sized non-crystalline specimens," *Nature*, vol. 400, pp. 342–344, 1999.

[13] S. C. Gallagher, W. N. Brandt, G. Chartas, and G. P. Garmire, "X-ray spectroscopy of quasi-stellar objects with broad ultraviolet absorption lines," *The Astrophysical Journal*, vol. 567, no. 1, p. 37, 2002.

[14] B. K. Agarwal *et al.*, "X-ray spectroscopy," *Springer series in optical sciences*, vol. 15, pp. 35–46, 1979.

[15] J. F. Moulder, W. F. Stickle, P. E. Sobol, and K. D. Bomben, *Handbook of X-ray photoelectron spectroscopy*, vol. 40. Perkin Elmer Eden Prairie, MN, 1992.

[16] H. N. Chapman, "X-ray imaging beyond the limits," *Nature Materials*, vol. 8, no. 4, pp. 299–301, 2009.

[17] C. Günther, B. Pfau, R. Mitzner, B. Siemer, S. Roling, H. Zacharias, O. Kutz, I. Rudolph, D. Schondelmaier, R. Treusch, *et al.*, "Sequential femtosecond x-ray imaging," *Nature Photonics*, vol. 5, no. 2, pp. 99–102, 2011.

[18] S. Carbajo, I. Howlett, F. Brizuela, K. Buchanan, M. Marconi, W. Chao, E. Anderson, I. Artioukov, A. Vinogradov, J. Rocca, *et al.*, "Sequential single-shot imaging of nanoscale dynamic interactions with a table-top soft x-ray laser," *Optics letters*, vol. 37, no. 14, pp. 2994–2996, 2012.

[19] D. H. Bilderback, P. Elleaume, and E. Weckert, "Review of third and next generation synchrotron light sources," *Journal of Physics B: Atomic, molecular and optical physics*, vol. 38, no. 9, p. S773, 2005.

[20] M. Altarelli, R. Brinkmann, M. Chergui, W. Decking, B. Dobson, S. Düsterer, G. Grübel, W. Graeff, H. Graafsma, J. Hajdu, *et al.*, “The european x-ray free-electron laser,” *Technical Design Report, DESY*, vol. 97, pp. 1–26, 2006.

[21] M. Xie, “Design optimization for an x-ray free electron laser driven by slac linac,” in *Particle Accelerator Conference, 1995., Proceedings of the 1995*, vol. 1, pp. 183–185, IEEE, 1995.

[22] H. Schwettman, J. Turneaure, and R. Waites, “Evidence for surface-state-enhanced field emission in rf superconducting cavities,” *Journal of Applied Physics*, vol. 45, no. 2, pp. 914–922, 1974.

[23] W. Leemans, B. Nagler, A. Gonsalves, C. Toth, K. Nakamura, C. Geddes, E. Esarey, C. Schroeder, and S. Hooker, “Gev electron beams from a centimetre-scale accelerator,” *Nature physics*, vol. 2, no. 10, pp. 696–699, 2006.

[24] M. Fuchs, R. Weingartner, A. Popp, Z. Major, S. Becker, J. Osterhoff, I. Cortrie, B. Zeitler, R. Hörlein, G. D. Tsakiris, *et al.*, “Laser-driven soft-x-ray undulator source,” *Nature physics*, vol. 5, no. 11, pp. 826–829, 2009.

[25] S. Mangles, A. Thomas, M. Kaluza, O. Lundh, F. Lindau, A. Persson, F. Tsung, Z. Najmudin, W. Mori, C.-G. Wahlström, *et al.*, “Laser-wakefield acceleration of monoenergetic electron beams in the first plasma-wave period,” *Physical review letters*, vol. 96, no. 21, p. 215001, 2006.

[26] J. Rocca, V. Shlyaptsev, F. Tomasel, O. Cortazar, D. Hartshorn, and J. Chilla, “Demonstration of a discharge pumped table-top soft-x-ray laser,” *Physical Review Letters*, vol. 73, no. 16, p. 2192, 1994.

[27] K. Nakajima, “Compact x-ray sources: Towards a table-top free-electron laser,” *Nature physics*, vol. 4, no. 2, pp. 92–93, 2008.

[28] J. Rocca, “Table-top soft x-ray lasers,” *Review of Scientific Instruments*, vol. 70, no. 10, pp. 3799–3827, 1999.

[29] M.-C. Chen, P. Arpin, T. Popmintchev, M. Gerrity, B. Zhang, M. Seaberg, D. Popmintchev, M. Murnane, and H. Kapteyn, “Bright, coherent, ultrafast soft x-ray harmonics spanning the water window from a tabletop light source,” *Physical review letters*, vol. 105, no. 17, p. 173901, 2010.

[30] T. Y. Fan, D. Ripin, R. Aggarwal, J. Ochoa, B. Chann, M. Tilleman, and J. Spitzberg, “Cryogenic yb3+-doped solid-state lasers,” *Selected Topics in Quantum Electronics, IEEE Journal of*, vol. 13, pp. 448–459, May 2007.

[31] T. Y. Fan and R. Byer, “Diode laser-pumped solid-state lasers,” *Quantum Electronics, IEEE Journal of*, vol. 24, pp. 895–912, June 1988.

[32] U. Brauch, A. Giesen, M. Karszewski, C. Stewen, and A. Voss, “Multiwatt diode-pumped yb:yag thin disk laser continuously tunablebetween 1018 and 1053 nm,” *Opt. Lett.*, vol. 20, pp. 713–715, Apr 1995.

[33] D. Brown, “The promise of cryogenic solid-state lasers,” *Selected Topics in Quantum Electronics, IEEE Journal of*, vol. 11, pp. 587–599, May 2005.

[34] Y. Akahane, M. Aoyama, K. Ogawa, K. Tsuji, S. Tokita, J. Kawanaka, H. Nishioka, and K. Yamakawa, “High-energy, diode-pumped, picosecond yb:yag chirped-pulse regenerative amplifier for pumping optical parametric chirped-pulse amplification,” *Opt. Lett.*, vol. 32, pp. 1899–1901, Jul 2007.

[35] K.-H. Hong, A. Siddiqui, J. Moses, J. Gopinath, J. Hybl, F. Ömer Ilday, T. Y. Fan, and F. X. Kärtner, “Generation of 287 w, 5.5 ps pulses at 78 mhz repetition rate from a cryogenically cooled yb:yag amplifier seeded by a fiber chirped-pulse amplification system,” *Opt. Lett.*, vol. 33, pp. 2473–2475, Nov 2008.

[36] J. Kawanaka, K. Yamakawa, H. Nishioka, and K. ichi Ueda, “30-mj, diode-pumped, chirped-pulse yb:ylf regenerative amplifier,” *Opt. Lett.*, vol. 28, pp. 2121–2123, Nov 2003.

[37] J. Kawanaka, K. Yamakawa, H. Nishioka, and K. ichi Ueda, “Improved high-field laser characteristics of a diode-pumped yb:liyf4 crystal at low temperature,” *Opt. Express*, vol. 10, pp. 455–460, May 2002.

[38] J. Kawanaka, H. Nishioka, N. Inoue, and K. ichi Ueda, “Tunable continuous-wave yb:ylf laser operation with a diode-pumped chirped-pulse amplification system,” *Appl. Opt.*, vol. 40, pp. 3542–3546, Jul 2001.

[39] K. Ogawa, Y. Akahane, and K. Yamakawa, “100-mj diode-pumped, cryogenically-cooled yb:ylf chirped-pulse regenerative amplifier,” in *CLEO:2011 - Laser Applications to Photonic Applications*, p. CMB4, Optical Society of America, 2011.

[40] D. Rand, D. Miller, D. J. Ripin, and T. Y. Fan, "Cryogenic yb^{3+}-doped materials for pulsed solid-state laser applications," *Opt. Mater. Express*, vol. 1, pp. 434–450, Jul 2011.

[41] D. E. Miller, L. E. Zapata, D. J. Ripin, and T. Y. Fan, "Sub-picosecond pulses at 100 w average power from a yb:ylf chirped-pulse amplification system," *Opt. Lett.*, vol. 37, pp. 2700–2702, Jul 2012.

[42] A. Chong, J. Buckley, W. Renninger, and F. Wise, "All-normal-dispersion femtosecond fiber laser," *Opt. Express*, vol. 14, pp. 10095–10100, Oct 2006.

[43] FlexPDE, "Flexpde 6,"

[44] V. Yanovsky, C. Felix, and G. Mourou, "Why ring regenerative amplification (regen)?," *Applied Physics B*, vol. 74, no. 1, pp. s181–s183, 2002.

[45] W. Koechner, *Solid-State Laser Engineering*. Springer Series in Optical Sciences, Springer, 2006.

[46] D. Findlay and R. Clay, "The measurement of internal losses in 4-level lasers," *Physics Letters*, vol. 20, no. 3, pp. 277 – 278, 1966.

[47] J. Hebling, K.-L. Yeh, M. Hoffmann, and K. Nelson, "High-power thz generation, thz nonlinear optics, and thz nonlinear spectroscopy," *Selected Topics in Quantum Electronics, IEEE Journal of*, vol. 14, pp. 345–353, March 2008.

[48] L. J. Wong, A. Fallahi, and F. X. Kärtner, "Compact electron acceleration and bunch compression in thz waveguides," *Opt. Express*, vol. 21, pp. 9792–9806, Apr 2013.

[49] L. Palfalvi, J. Fulop, G. Toth, and J. Hebling, "Evanescent-wave proton post-accelerator driven by intense thz pulses," in *Lasers and Electro-Optics Europe (CLEO EUROPE/IQEC), 2013 Conference on and International Quantum Electronics Conference*, pp. 1–1, May 2013.

[50] E. Balogh, K. Kovacs, P. Dombi, J. A. Fulop, G. Farkas, J. Hebling, V. Tosa, and K. Varju, "Single attosecond pulse from terahertz-assisted high-order harmonic generation," *Phys. Rev. A*, vol. 84, p. 023806, Aug 2011.

[51] S. Fleischer, Y. Zhou, R. W. Field, and K. A. Nelson, "Molecular orientation and alignment by intense single-cycle thz pulses," *Phys. Rev. Lett.*, vol. 107, p. 163603, Oct 2011.

[52] B. Zaks, R. B. Liu, and M. S. Sherwin, “Experimental observation of electron-hole recollisions,” *Nature*, vol. 483, pp. 580–583, Mar. 2012.

[53] D. Daranciang, J. Goodfellow, M. Fuchs, H. Wen, S. Ghimire, D. A. Reis, H. Loos, A. S. Fisher, and A. M. Lindenberg, “Single-cycle terahertz pulses,” *Applied Physics Letters*, vol. 99, no. 14, pp. –, 2011.

[54] J. Hebling, K.-L. Yeh, M. C. Hoffmann, B. Bartal, and K. A. Nelson, “Generation of high-power terahertz pulses by tilted-pulse-front excitation and their application possibilities,” *J. Opt. Soc. Am. B*, vol. 25, pp. B6–B19, Jul 2008.

[55] J. A. Fülöp, Z. Ollmann, C. Lombosi, C. Skrobol, S. Klingebiel, L. Pálfalvi, F. Krausz, S. Karsch, and J. Hebling, “Efficient generation of thz pulses with 0.4 mj energy,” *Opt. Express*, vol. 22, pp. 20155–20163, Aug 2014.

[56] T. Taniuchi, “Widely-tunable thz-wave generation in 220 thz range from dast crystal by nonlinear difference frequency mixing,” *Electronics Letters*, vol. 40, pp. 60–62(2), January 2004.

[57] T. Taniuchi, “Continuously tunable thz and far-infrared wave generation from dast crystal,” *Electronics Letters*, vol. 40, pp. 549–551(2), April 2004.

[58] K. Y. Kim, A. J. Taylor, J. H. Glownia, and G. Rodriguez, “Coherent control of terahertz supercontinuum generation in ultrafast laser-gas interactions,” *Nat Photon*, vol. 2, pp. 605–609, Oct. 2008.

[59] C. Ruchert, C. Vicario, and C. P. Hauri, “Scaling submillimeter single-cycle transients toward megavolts per centimeter field strength via optical rectification in the organic crystal oh1,” *Opt. Lett.*, vol. 37, pp. 899–901, Mar 2012.

[60] C. P. Hauri, C. Ruchert, C. Vicario, and F. Ardana, “Strong-field single-cycle thz pulses generated in an organic crystal,” *Applied Physics Letters*, vol. 99, no. 16, pp. –, 2011.

[61] S.-W. Huang, E. Granados, W. R. Huang, K.-H. Hong, L. E. Zapata, and F. X. Kärtner, “High conversion efficiency, high energy terahertz pulses by optical rectification in cryogenically cooled lithium niobate,” *Opt. Lett.*, vol. 38, pp. 796–798, Mar 2013.

[62] J. Hebling, G. Almasi, I. Kozma, and J. Kuhl, “Velocity matching by pulse front tilting for large area thz-pulse generation,” *Opt. Express*, vol. 10, pp. 1161–1166, Oct 2002.

[63] J. A. Fülöp, L. Pálfalvi, G. Almási, and J. Hebling, “Design of high-energy terahertz sources based on optical rectification,” *Opt. Express*, vol. 18, pp. 12311–12327, Jun 2010.

[64] R. W. Boyd, *Nonlinear optics*. Academic press, 2003.

[65] C. Vicario, B. Monoszlai, C. Lombosi, A. Mareczko, A. Courjaud, J. A. Fülöp, and C. P. Hauri, “Pump pulse width and temperature effects in lithium niobate for efficient thz generation,” *Opt. Lett.*, vol. 38, pp. 5373–5376, Dec 2013.

[66] K. L. Vodopyanov, “Optical generation of narrow-band terahertz packets in periodically inverted electro-optic crystals: conversion efficiency and optimal laser pulse format,” *Opt. Express*, vol. 14, pp. 2263–2276, Mar 2006.

[67] D. Redfield and W. J. Burke, “Optical absorption edge of lithium niobate,” *Journal of Applied Physics*, vol. 45, no. 10, 1974.

[68] A.-L. Calendron, H. Cankaya, and F. X. Kärtner in *Research in Optical Sciences*, p. JW2A.16, Optical Society of America.

[69] J. A. Fülöp, L. Pálfalvi, S. Klingebiel, G. Almási, F. Krausz, S. Karsch, and J. Hebling, “Generation of sub-mj terahertz pulses by optical rectification,” *Opt. Lett.*, vol. 37, pp. 557–559, Feb 2012.

[70] J. A. Fülöp, L. Pálfalvi, M. C. Hoffmann, and J. Hebling, “Towards generation of mj-level ultrashort thz pulses by optical rectification,” *Opt. Express*, vol. 19, pp. 15090–15097, Aug 2011.

[71] N. E. Yu, M.-K. Oh, H. Kang, C. Jung, B. H. Kim, K.-S. Lee, D.-K. Ko, S. Takekawa, and K. Kitamura, “Continuous tuning of a narrow-band terahertz wave in periodically poled stoichiometric litao 3 crystal with a fan-out grating structure,” *Applied Physics Express*, vol. 7, no. 1, p. 012101, 2014.

[72] G. Xu, X. Mu, Y. J. Ding, and I. B. Zotova, “Efficient generation of backward terahertz pulses from multiperiod periodically poled lithium niobate,” *Opt. Lett.*, vol. 34, pp. 995–997, Apr 2009.

[73] N. Bannov, F. Vasko, and V. Mitin, “Terahertz absorption by electrons and confined acoustic phonons in free-standing quantum wells,” *Superlattices and Microstructures*, vol. 18, no. 4, pp. 269 –, 1995.

[74] J. ichi Shikata, M. Sato, T. Taniuchi, H. Ito, and K. Kawase, “Enhancement of terahertz-wave output from linbo3 optical parametric oscillators by cryogenic cooling,” *Opt. Lett.*, vol. 24, pp. 202–204, Feb 1999.

[75] Y.-S. Lee, T. Meade, M. DeCamp, T. B. Norris, and A. Galvanauskas, “Temperature dependence of narrow-band terahertz generation from periodically poled lithium niobate,” *Applied Physics Letters*, vol. 77, no. 9, 2000.

[76] C. Varin and M. Piche, “Relativistic attosecond electron pulses from a free-space laser-acceleration scheme,” *Phys. Rev. E*, vol. 74, p. 045602, Oct 2006.

[77] A. Sell and F. X. Kärtner, “Attosecond electron bunches accelerated and compressed by radially polarized laser pulses and soft-x-ray pulses from optical undulators,” *Journal of Physics B Atomic Molecular Physics*, vol. 47, p. 015601, Jan. 2014.

[78] S. P. D. Mangles, C. D. Murphy, Z. Najmudin, A. G. R. Thomas, J. L. Collier, A. E. Dangor, E. J. Divall, P. S. Foster, J. G. Gallacher, C. J. Hooker, D. A. Jaroszynski, A. J. Langley, W. B. Mori, P. A. Norreys, F. S. Tsung, R. Viskup, B. R. Walton, and K. Krushelnick, “Monoenergetic beams of relativistic electrons from intense laser-plasma interactions,” *Nature*, vol. 431, pp. 535–538, Sept. 2004.

[79] T. Toncian, M. Borghesi, J. Fuchs, E. d’Humieres, P. Antici, P. Audebert, E. Brambrink, C. A. Cecchetti, A. Pipahl, L. Romagnani, and O. Willi, “Ultrafast laser-driven microlens to focus and energy-select mega-electron volt protons,” *Science*, vol. 312, no. 5772, pp. 410–413, 2006.

[80] S. Carbajo, E. Granados, D. Schimpf, A. Sell, K.-H. Hong, J. Moses, and F. X. Kärtner, “Efficient generation of ultra-intense few-cycle radially polarized laser pulses,” *Optics Letters*, vol. 39, no. 8, pp. 2487–2490, 2014.

[81] P.-L. Fortin, M. Piché, and C. Varin, “Direct-field electron acceleration with ultrafast radially polarized laser beams: scaling laws and optimization,” *Journal of Physics B Atomic Molecular Physics*, vol. 43, p. 025401, Jan. 2010.

[82] Y. I. Salamin, “Electron acceleration from rest in vacuum by an axicon gaussian laser beam,” *Phys. Rev. A*, vol. 73, p. 043402, Apr 2006.

[83] M. D. Perry and G. Mourou, “Terawatt to petawatt subpicosecond lasers,” *Science*, vol. 264, no. 5161, pp. 917–924, 1994.

[84] K.-H. Hong, B. Hou, J. Nees, E. Power, and G. Mourou, "Generation and measurement of >108 intensity contrast ratio in a relativistic khz chirped-pulse amplified laser," *Applied Physics B*, vol. 81, no. 4, pp. 447–457, 2005.

[85] O. Albert, H. Wang, D. Liu, Z. Chang, and G. Mourou, "Generation of relativistic intensity pulses at a kilohertz repetition rate," *Opt. Lett.*, vol. 25, pp. 1125–1127, Aug 2000.

[86] R. Dorn, S. Quabis, and G. Leuchs, "Sharper focus for a radially polarized light beam," *Phys. Rev. Lett.*, vol. 91, p. 233901, Dec 2003.

[87] K. Youngworth and T. Brown, "Focusing of high numerical aperture cylindrical-vector beams," *Opt. Express*, vol. 7, pp. 77–87, Jul 2000.

[88] L. Novotny, M. R. Beversluis, K. S. Youngworth, and T. G. Brown, "Longitudinal field modes probed by single molecules," *Phys. Rev. Lett.*, vol. 86, pp. 5251–5254, Jun 2001.

[89] D. P. Biss and T. G. Brown, "Polarization-vortex-driven second-harmonic generation," *Opt. Lett.*, vol. 28, pp. 923–925, Jun 2003.

[90] I. Moshe, S. Jackel, and A. Meir, "Production of radially or azimuthally polarized beams in solid-state lasers and the elimination of thermally induced birefringence effects," *Opt. Lett.*, vol. 28, pp. 807–809, May 2003.

[91] C. Hnatovsky, V. G. Shvedov, N. Shostka, A. V. Rode, and W. Krolikowski, "Polarization-dependent ablation of silicon using tightly focused femtosecond laser vortex pulses," *Opt. Lett.*, vol. 37, pp. 226–228, Jan 2012.

[92] L. Cicchitelli, H. Hora, and R. Postle, "Longitudinal field components for laser beams in vacuum," *Phys. Rev. A*, vol. 41, pp. 3727–3732, Apr 1990.

[93] J. Rosenzweig, A. Murokh, and C. Pellegrini, "A proposed dielectric-loaded resonant laser accelerator," *Phys. Rev. Lett.*, vol. 74, pp. 2467–2470, Mar 1995.

[94] W. D. Kimura, G. H. Kim, R. D. Romea, L. C. Steinhauer, I. V. Pogorelsky, K. P. Kusche, R. C. Fernow, X. Wang, and Y. Liu, "Laser acceleration of relativistic electrons using the inverse cherenkov effect," *Phys. Rev. Lett.*, vol. 74, pp. 546–549, Jan 1995.

[95] S. Payeur, S. Fourmaux, B. E. Schmidt, J. P. MacLean, C. Tchervenkov, F. Legare, M. Piche, and J. C. Kieffer, "Generation of a beam of fast electrons by tightly focusing a radially polarized ultrashort laser pulse," *Applied Physics Letters*, vol. 101, no. 4, pp. –, 2012.

[96] M. Bock, J. Brunne, A. Treffer, S. König, U. Wallrabe, and R. Grunwald, "Sub-3-cycle vortex pulses of tunable topological charge," *Opt. Lett.*, vol. 38, pp. 3642–3645, Sep 2013.

[97] M. Nisoli, S. De Silvestri, and O. Svelto, "Generation of high energy 10 fs pulses by a new pulse compression technique," *Applied Physics Letters*, vol. 68, no. 20, 1996.

[98] E. Granados, L.-J. Chen, C.-J. Lai, K.-H. Hong, and F. X. Kärtner, "Wavelength scaling of optimal hollow-core fiber compressors in the single-cycle limit," *Opt. Express*, vol. 20, pp. 9099–9108, Apr 2012.

[99] A. A. Ishaaya, C. J. Hensley, B. Shim, S. Schrauth, K. W. Koch, and A. L. Gaeta, "Highly-efficient coupling of linearly- and radially-polarized femtosecond pulses in hollow-core photonic band-gap fibers," *Opt. Express*, vol. 17, pp. 18630–18637, Oct 2009.

[100] E. A. J. Marcatili and R. A. Schmeltzer, "Hollow metallic and dielectric waveguides for long distance optical transmission and lasers," *Bell System Technical Journal*, vol. 43, no. 4, pp. 1783–1809, 1964.

[101] G. Machavariani, Y. Lumer, I. Moshe, A. Meir, and S. Jackel, "Efficient extra-cavity generation of radially and azimuthally polarized beams," *Opt. Lett.*, vol. 32, pp. 1468–1470, Jun 2007.

[102] M. Born and E. Wolf, *Principles of Optics: Electromagnetic Theory of Propagation, Interference and Diffaction of Light*. Pergamon Press, 1959.

[103] Y. Kozawa and S. Sato, "Sharper focal spot formed by higher-order radially polarized laser beams," *J. Opt. Soc. Am. A*, vol. 24, pp. 1793–1798, Jun 2007.

[104] S. C. Tidwell, D. H. Ford, and W. D. Kimura, "Generating radially polarized beams interferometrically," *Appl. Opt.*, vol. 29, pp. 2234–2239, May 1990.

[105] M. A. Ahmed, J. Schulz, A. Voss, O. Parriaux, J.-C. Pommier, and T. Graf, "Radially polarized 3kw beam from a co2 laser with an intracavity resonant grating mirror," *Opt. Lett.*, vol. 32, pp. 1824–1826, Jul 2007.

[106] R. Oron, S. Blit, N. Davidson, A. A. Friesem, Z. Bomzon, and E. Hasman, “The formation of laser beams with pure azimuthal or radial polarization,” *Applied Physics Letters*, vol. 77, no. 21, 2000.

[107] T. Tajima and J. M. Dawson, “Laser electron accelerator,” *Phys. Rev. Lett.*, vol. 43, pp. 267–270, Jul 1979.

[108] A. Buck, M. Nicolai, K. Schmid, C. M. S. Sears, A. Savert, J. M. Mikhailova, F. Krausz, M. C. Kaluza, and L. Veisz, “Real-time observation of laser-driven electron acceleration,” *Nat Phys*, vol. 7, pp. 543–548, July 2011.

[109] E. Peralta, K. Soong, R. England, E. Colby, Z. Wu, *et al.*, “Demonstration of electron acceleration in a laser-driven dielectric microstructure,” *Nature*, 2013.

[110] A. van Steenbergen, J. Gallardo, J. Sandweiss, and J.-M. Fang, “Observation of energy gain at the bnl inverse free-electron-laser accelerator,” *Phys. Rev. Lett.*, vol. 77, pp. 2690–2693, Sep 1996.

[111] J. Bae, H. Shirai, T. Nishida, T. Nozokido, K. Furuya, and K. Mizuno, “Experimental verification of the theory on the inverse smith purcell effect at a submillimeter wavelength,” *Applied Physics Letters*, vol. 61, no. 7, 1992.

[112] T. Plettner, R. L. Byer, E. Colby, B. Cowan, C. M. S. Sears, J. E. Spencer, and R. H. Siemann, “Visible-laser acceleration of relativistic electrons in a semi-infinite vacuum,” *Phys. Rev. Lett.*, vol. 95, p. 134801, Sep 2005.

[113] E. Esarey, C. B. Schroeder, and W. P. Leemans, “Physics of laser-driven plasma-based electron accelerators,” *Rev. Mod. Phys.*, vol. 81, pp. 1229–1285, Aug 2009.

[114] C. G. R. Geddes, C. Toth, J. van Tilborg, E. Esarey, C. B. Schroeder, D. Bruhwiler, C. Nieter, J. Cary, and W. P. Leemans, “High-quality electron beams from a laser wakefield accelerator using plasma-channel guiding,” *Nature*, vol. 431, pp. 538–541, September 2004.

[115] S. Carbajo, L. J. Wong, E. Nanni, D. N. Schimpf, and F. X. Kärtner, “Ultra-intense few-cycle radial polarization source for vacuum laser acceleration,” in *Research in Optical Sciences*, p. HTu2C.6, Optical Society of America, 2014.

[116] L. J. Wong and F. X. Kaertner, “Direct acceleration of an electron in infinite vacuum by a pulsed radially-polarized laser beam,” *Opt. Express 18*, vol. 25035-25051, 2010.

Appendix A

Solid-state Laser Materials Chart

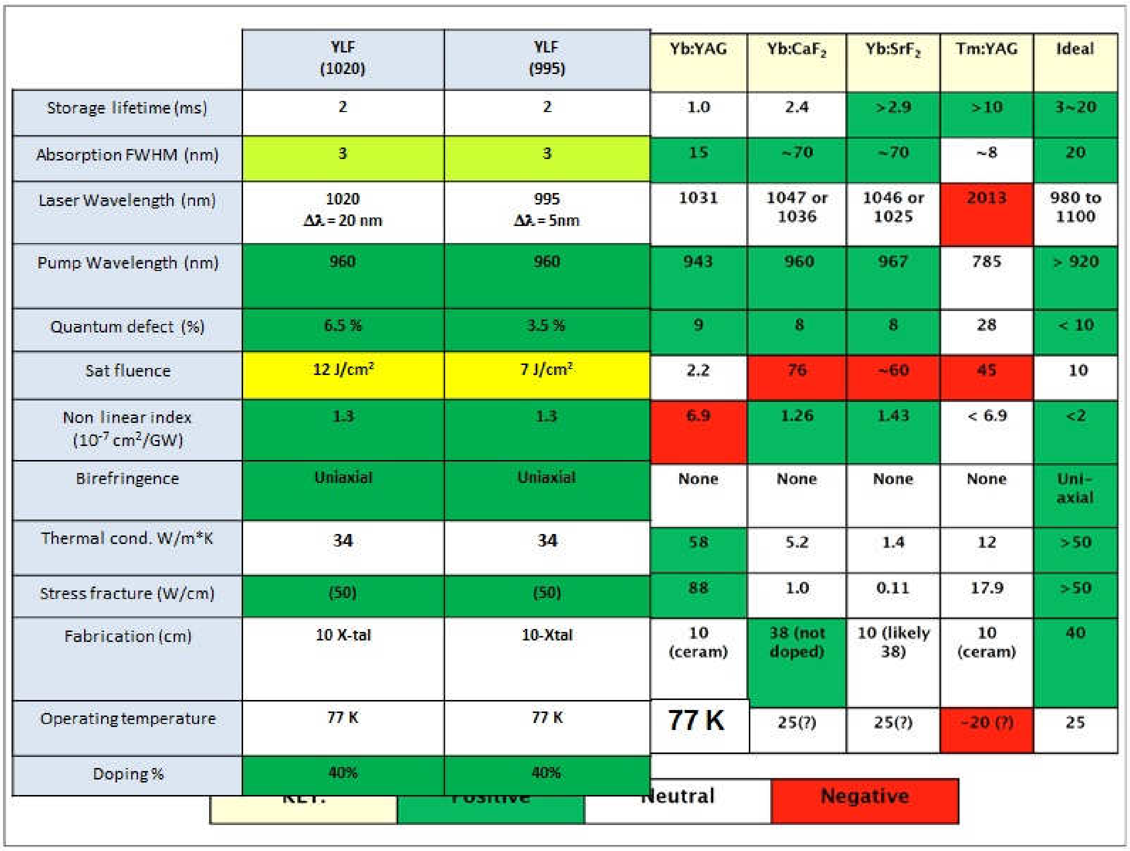

	YLF (1020)	YLF (995)	Yb:YAG	Yb:CaF_2	Yb:SrF_2	Tm:YAG	Ideal
Storage lifetime (ms)	2	2	1.0	2.4	>2.9	>10	3~20
Absorption FWHM (nm)	3	3	15	~70	~70	~8	20
Laser Wavelength (nm)	1020 $\Delta\lambda$ = 20 nm	995 $\Delta\lambda$ = 5nm	1031	1047 or 1036	1046 or 1025	2013	980 to 1100
Pump Wavelength (nm)	960	960	943	960	967	785	> 920
Quantum defect (%)	6.5 %	3.5 %	9	8	8	28	< 10
Sat fluence	12 J/cm^2	7 J/cm^2	2.2	76	~60	45	10
Non linear index (10^{-7} cm^2/GW)	1.3	1.3	6.9	1.26	1.43	< 6.9	<2
Birefringence	Uniaxial	Uniaxial	None	None	None	None	Uni-axial
Thermal cond. W/m*K	34	34	58	5.2	1.4	12	>50
Stress fracture (W/cm)	(50)	(50)	88	1.0	0.11	17.9	>50
Fabrication (cm)	10 X-tal	10-Xtal	10 (ceram)	38 (not doped)	10 (likely 38)	10 (ceram)	40
Operating temperature	77 K	77 K	77 K	25(?)	25(?)	-20 (?)	25
Doping %	40%	40%					

Neutral Negative

Fig. A.1 Relevant SSL material properties for Yb:YLF, Yb:YAG, Yb:CaF_2, Yb:SrF_2, and Tm:YAG. Chart completed by Chris Barty at LLNL and Luis Zapata at MIT LL.

Appendix B

Pockels Cell Supplementary Information

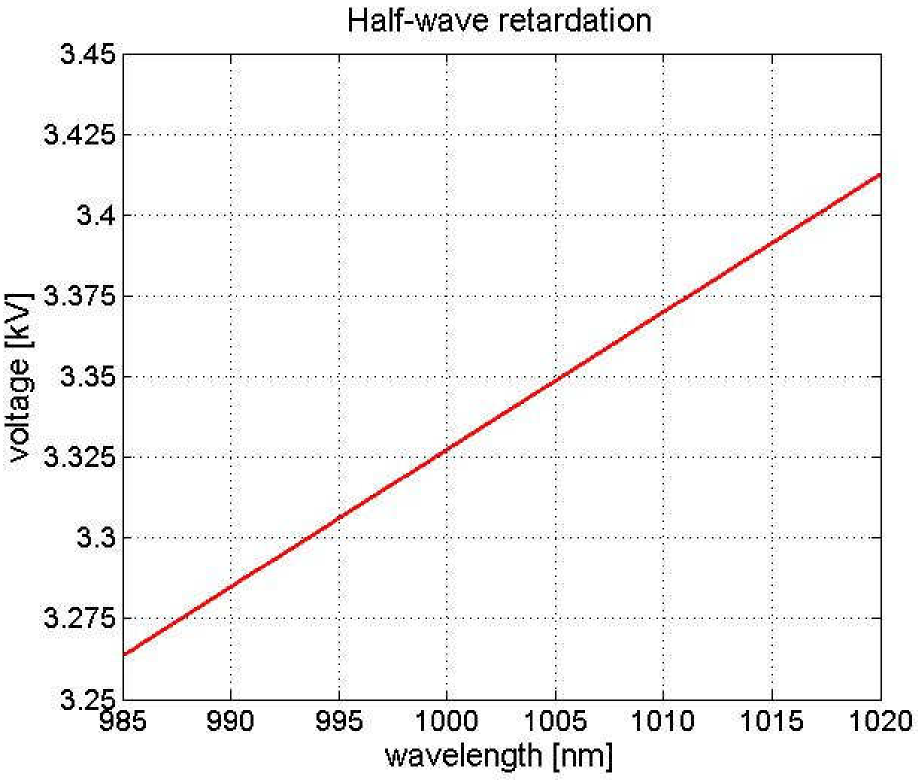

Fig. B.1 $\lambda/2$-retardation driving voltage of the KD*P Pockels Cell (1042 series).

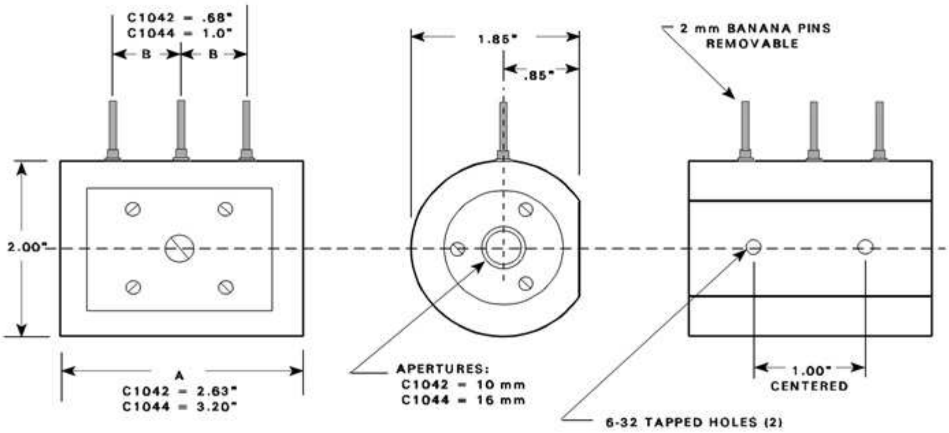
C1042 = .68"
C1044 = 1.0"
B
B
1.85"
.85"
2 mm BANANA PINS REMOVABLE
2.00"
A
C1042 = 2.63"
C1044 = 3.20"
APERTURES:
C1042 = 10 mm
C1044 = 16 mm
1.00" CENTERED
6-32 TAPPED HOLES (2)

Fig. B.2 Technical drawing of the assembled PC-retarder.

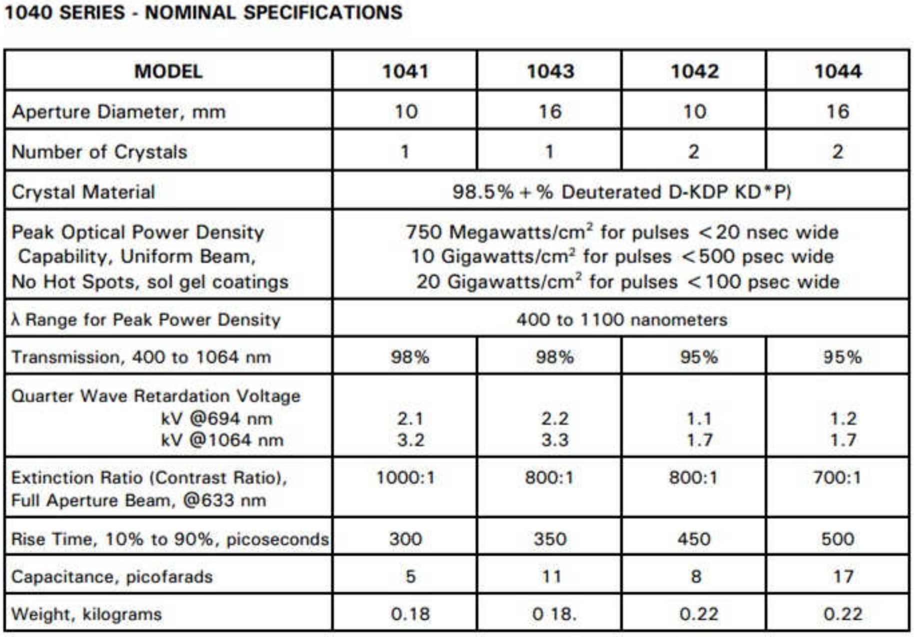

1040 SERIES - NOMINAL SPECIFICATIONS

MODEL	1041	1043	1042	1044
Aperture Diameter, mm	10	16	10	16
Number of Crystals	1	1	2	2
Crystal Material	98.5%+% Deuterated D-KDP KD*P)			
Peak Optical Power Density Capability, Uniform Beam, No Hot Spots, sol gel coatings	750 Megawatts/cm² for pulses <20 nsec wide 10 Gigawatts/cm² for pulses <500 psec wide 20 Gigawatts/cm² for pulses <100 psec wide			
λ Range for Peak Power Density	400 to 1100 nanometers			
Transmission, 400 to 1064 nm	98%	98%	95%	95%
Quarter Wave Retardation Voltage kV @694 nm kV @1064 nm	 2.1 3.2	 2.2 3.3	 1.1 1.7	 1.2 1.7
Extinction Ratio (Contrast Ratio), Full Aperture Beam, @633 nm	1000:1	800:1	800:1	700:1
Rise Time, 10% to 90%, picoseconds	300	350	450	500
Capacitance, picofarads	5	11	8	17
Weight, kilograms	0.18	0 18.	0.22	0.22

Fig. B.3 Main parameters of 1040 series KD*P Pockels Cells.

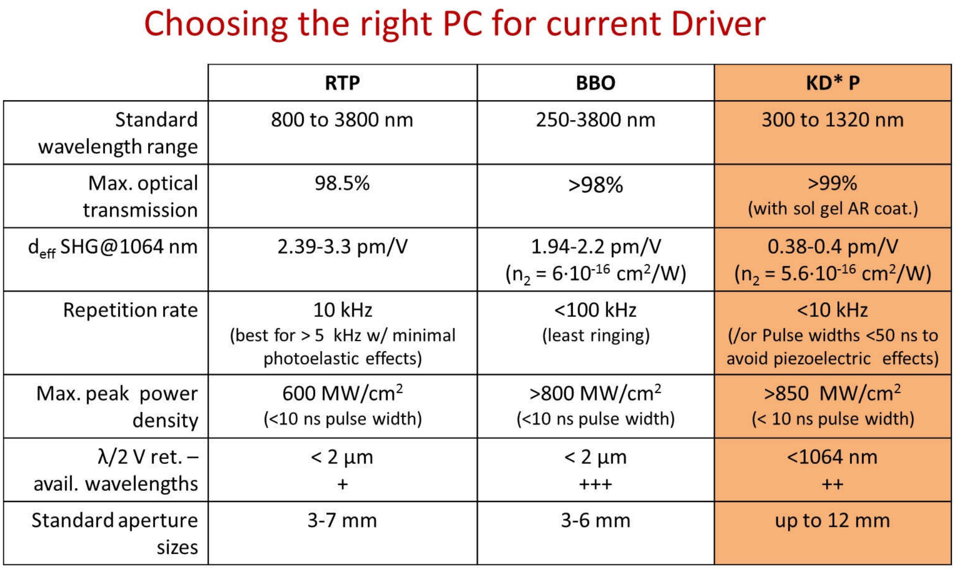

Choosing the right PC for current Driver

	RTP	BBO	KD* P
Standard wavelength range	800 to 3800 nm	250-3800 nm	300 to 1320 nm
Max. optical transmission	98.5%	>98%	>99% (with sol gel AR coat.)
d_{eff} SHG@1064 nm	2.39-3.3 pm/V	1.94-2.2 pm/V ($n_2 = 6{\cdot}10^{-16}$ cm^2/W)	0.38-0.4 pm/V ($n_2 = 5.6{\cdot}10^{-16}$ cm^2/W)
Repetition rate	10 kHz (best for > 5 kHz w/ minimal photoelastic effects)	<100 kHz (least ringing)	<10 kHz (/or Pulse widths <50 ns to avoid piezoelectric effects)
Max. peak power density	600 MW/cm^2 (<10 ns pulse width)	>800 MW/cm^2 (<10 ns pulse width)	>850 MW/cm^2 (< 10 ns pulse width)
λ/2 V ret. – avail. wavelengths	< 2 µm +	< 2 µm +++	<1064 nm ++
Standard aperture sizes	3-7 mm	3-6 mm	up to 12 mm

Fig. B.4 PC materials standard parameters chart.

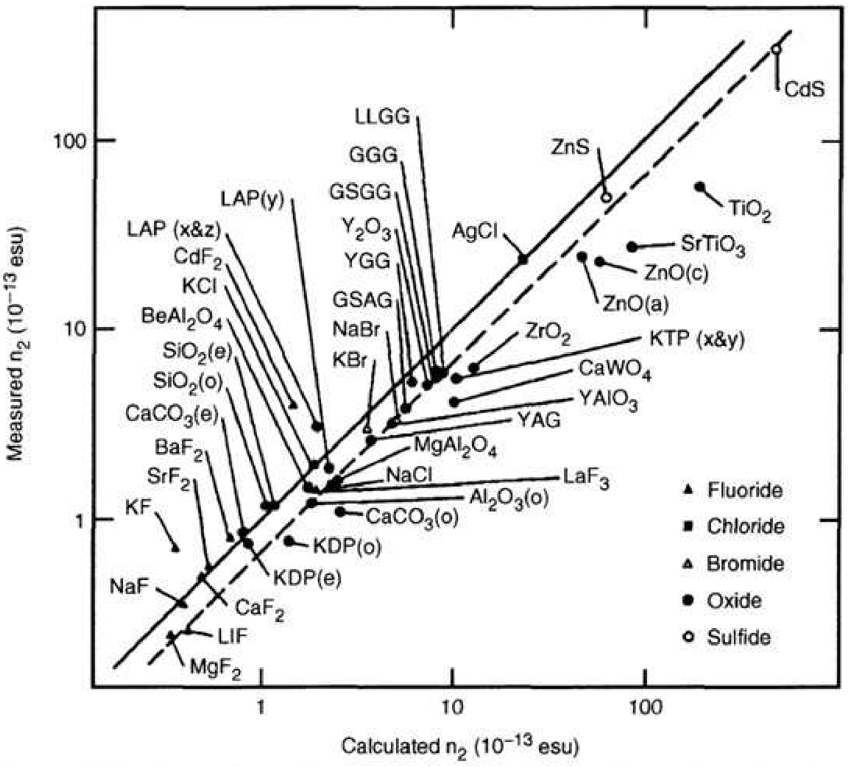

Fig. B.5 Measured and calculated nonlinear indices of refraction of optical crystals [4, 5].

Appendix C

Laser-driven Particle Acceleration

Here we recreate the dynamics of a 10^5 particle distribution 10 picoseconds after collision initially distributed in an ellipsoid with 0.8 μm transverse and 2.5 μm longitudinal semi-principal axes and initial kinetic energy of 40 keV. Fig. C.1 shows the net kinetic energy redistribution of the monochromatic particle bunch. Note that we are plotting change in kinetic energy and that some of those electrons will actually be decelerated by the field.

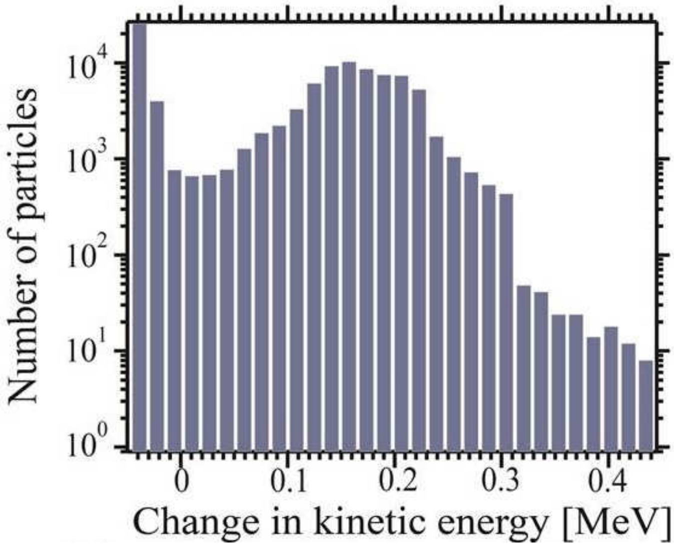

Fig. C.1 Particle net kinetic energy gain histogram.

In real-specе, the interaction is represented in Fig. C.2. The accelerated particles with a non-zero azimuthal angle, that is, the ones far off the $x = 0$ on-axis line, are the result of ponderomotive acceleration by transverse electromagnetic field components.

We also plot (Fig. C.3) the final kinetic energy as a function of deflection angle with respect to the azimuth. All of the particles in the 0-degree deflection angle are electrons

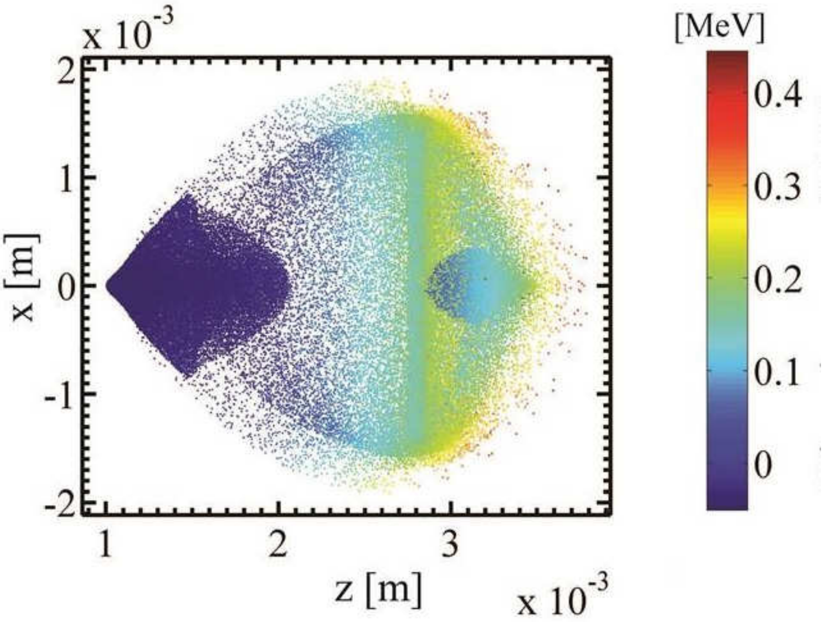

Fig. C.2 Final kinetic energy electron distribution (colormap) 10 ps after laser collision in real-space as a function of transverse dimension (x) and longitudinal dimension (z).

accelerated purely due to the longitudinal component, the on-axis component of the laser field, which are the ones can reach up to half an MeV of final kinetic energy.

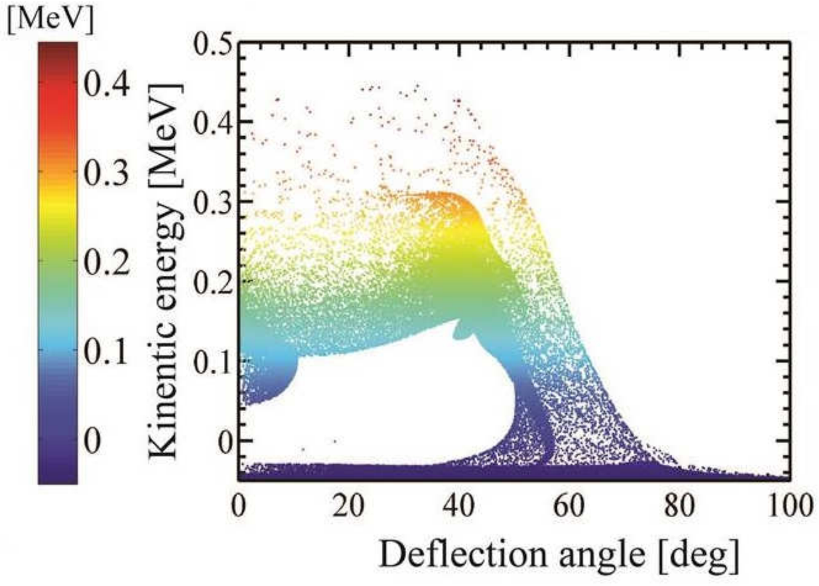

Fig. C.3 Final kinetic energy electron distribution 10 ps after laser collision as a function of azimuthal angle.